Experimental and Numerical Investigations of Two-Phase Flow in Confined Channels

Thesis

submitted in partial fulfillment of the requirement for the degree of

Doctor of Philosophy

by

Deepak Kumar Mishra

Roll No-176107014

Department of Chemical Engineering

Indian Institute of Technology Guwahati

Guwahati India

August, 2024

Dedicated to the

Almighty

Department of Chemical Engineering
Indian Institute of Technology Guwahati
Guwahati 781039, India

CERTIFICATE

It is certified that the work contained in the thesis entitled “**Experimental and Numerical Investigations of Two-Phase Flow in Confined Channels**”, by **Mr. Deepak Kumar Mishra**, has been carried out under my supervision. The work documented in this thesis has not been submitted to any other University or Institute for the award of any degree or diploma.

Dr. Raghvendra Gupta
Associate Professor
Department of Chemical Engineering
Indian Institute of Technology Guwahati
Guwahati 781039, India

Prof. Anugrah Singh
Professor
Department of Chemical Engineering
Indian Institute of Technology Guwahati
Guwahati 781039, India

Acknowledgments

I would like to thank my thesis supervisors, Dr. Raghvendra Gupta and Prof. Anugrah Singh. They have been a constant source of inspiration throughout this journey. Their kind nature and smart research aptitude created a conducive environment to develop the important research skills of critical thinking and perseverance. This journey was full of ups and downs, and I am so grateful for their patience with me and constant professional and personal support.

I would like to thank my doctoral committee members, Prof. Tapas Kumar Mandal, Prof. Manmohan Pandey, and Dr. Partho Sarathi Gooh Pattader, along with previous members Prof. Rajesh Kumar Upadhyay, Prof. Ganesh Natarajan, and Anki Reddy katha for their valuable suggestions and constructive criticism, which helped me to enhance the quality of my research work. They not only helped improve the technical part of the research but also improved my writing and presentation skills.

I am also thankful to all the faculty members of the Department of Chemical Engineering with whom I was associated either as a student for coursework or as a teaching assistant. I would also like to extend my sincere gratitude to all the technical officers and office staff of the department.

I express my deepest gratitude to all my friends and mentors, especially Dr. Mahesh Nagargoje, Dr. Swarna Makkitaya, Dr. Ankush Sontakke, Shweta Kumbhar, Roushni Kumari, Mudrika Singhal, Akash, Awkash Shrivastava, and Dr. Priya Jha. I am so grateful for the unconditional love and support from my sisters Vibha and Ruby and Advika, Ishika, Yanshu, and my parents, who have always been a constant source of motivation. This journey would not have been possible without the love and care of my dearest friend, soulmate, and wife, Priyanka.

In the end, I bow down to almighty God and thank for this beautiful journey of life.

ABSTRACT

Two-phase flow in mini and microchannels has been a major area of interest over the past few decades. Due to the large interfacial area density, easy-to-control processes, high heat and mass transfer rates, and enhanced safety flow in small channels are proven to be well-suited for miniaturization. Cooling devices, reactors, inkjet printers, droplet reactors, etc., are a few of the key areas in which two-phase flow in microchannels are being applied. Single-phase flow in microchannels is laminar due to the dominant viscous force over the inertial force. In two-phase flow, different flow regimes develop based on the flow rates, interfacial tension, and viscosity and density ratios. Major flow regimes are bubbly, slug, annular, and churn flow. Industrial application of such flow regimes often involves the introduction of curved segments or U-bends to connect multiple straight channels to provide larger path length and residence time or to allow sufficient mixing in the flow.

A survey of the literature study suggests that the understanding of hydrodynamics in different flow regimes through such curved channels is limited in terms of its effect on the distribution of liquid film near the wall and velocity field. The knowledge of liquid film thickness and velocity field plays an important role in designing microdevices as it affects heat and mass transfer rates and mixing. Similar to gas-liquid flow in microchannels (small and long Taylor bubbles), a liquid droplet in another immiscible liquid media also acts as a single batch *droplet reactor* by having an internal recirculation pattern due to the shear force applied at the interface by outer liquid. The physics of internal circulation inside the droplet moving in another immiscible liquid media is very important to understand because of its wide applicability for liquid-liquid extraction, separation and purification, and enhanced oil recovery.

This thesis addresses these two important and common problems in different applications of two-phase flow in confined channels using experimental and computational investigations. This thesis is divided into two sections, and the specific objectives of the thesis are:

(A) Study of different gas-liquid flow regimes in a curved microchannel.

- To quantify the liquid film thickness in different flow regimes using high-speed flow visualization.
- To study the interface evolution and velocity field in different flow regimes using three-dimensional numerical simulations.

(B) Study of internal circulation within a droplet falling under gravity in another immiscible liquid media.

- To study the effect of droplet diameter and release location from the wall on the internal velocity field within a single droplet and during the coalescence of two droplets using particle image velocimetry.
- To investigate the effect of viscosity ratio on internal recirculations and shape deformation inside a single droplet and during coalescence using two-dimensional numerical simulations.

Gas-liquid flow in a microchannel with multiple U-bends is studied over a range of gas and liquid flow rates using a high-speed camera for Newtonian liquids of different viscosities. The flow regime is observed to transition from slug to annular flow regime for the conditions studied with a change in gas flow rate. The liquid film formed between the wall and gas core/bubble is observed to be asymmetric in the curved section of the channel due to the centrifugal force. In the slug flow regime, the film thickness on the inner wall of the bend is observed to be thinner than that on the outer wall. On the other hand, the inner film is observed to be thicker than the outer film in the annular flow regime. This transition is possibly caused by the change in the relative importance of gas and liquid centrifugal forces with an increase in the gas flow rate.

Three-dimensional CFD simulations are carried out for slug, slug-annular, and annular flow regimes in a U-bend. The evolution of bubble shape in the slug flow regime, interface shape in the annular flow regime, and their effect on the velocity field are analyzed in detail. It is observed that similar to experimental results, the liquid film is asymmetric, and the inner film is thinner in the case of slug flow and thicker in the case of annular flow than the outer liquid film. Dean vortices are observed in the liquid slug at the bend, and the size of the circulation decreases as the bubble approaches. The bubble regains its front and back shape after traveling a sufficient length downstream of the bend. In the case of slug-annular and annular flow, the symmetric annulus is formed in an upstream straight section of the bend but becomes asymmetric after passing through the bend.

The flow field inside a droplet falling under gravity in a continuous liquid is studied using particle image velocimetry (PIV). A parametric study is carried out to understand the effect of droplet diameter and release distance from the wall. Two counter-rotating vortices spanning the bottom half of the droplet are observed in the droplet frame of reference for the droplet released at the center of the channel. This symmetric internal motion is driven by symmetric tangential stress at the interface by the surrounding liquid. The size of the internal recirculation grows with an increase in the droplet diameter. Asymmetry appears in the recirculation pattern due to asymmetric tangential stress when the droplet is released from a location between the channel centerline and the sidewall. The closer the release location to the wall, the higher the center of the vortex near the wall, and the lower the vortex center near the centerline. The presence of a wall results in increased shear on the interface closer to the wall, resulting in a bigger near-wall vortex. Further, the recirculation behavior during the coalescence is studied by releasing a smaller droplet followed by a bigger droplet at the channel center. The bigger

droplet slows down and coalesces with the smaller droplet when their velocities become equal. As the droplets coalesce, the coalescence point grows to take a neck-like shape, which grows rapidly in the beginning and then widens slowly. The growth of the neck is accompanied by the velocity directed radially outward at the neck, having velocity equal to the rate of neck growth. A pair of counter-rotating vortices are observed on each side of the neck. These vortices readjust the fluid such that the droplet gains the shape of a single bigger droplet.

Numerical study of a droplets falling in a continuous liquid under the effect of gravity using the VOF method is done to understand the effect of viscosity ratio and shape deformation. Two-dimensional CFD simulations have been performed for different droplet diameters, viscosity ratios, and release positions. Symmetric, counter-rotating vortices are observed in the case of droplets released from the center. The shape of the droplet released from the center changes from circular to oval while maintaining the symmetric vortices as the viscosity of the droplet fluid decreases. As the release location changes to near the wall, the asymmetry appears, and the location of the vortices changes from the upper part to the lower part of the droplet. Shape deformation is also observed with less viscous droplets when released near the wall, along with the asymmetric position of the vortices. While there is qualitative agreement between CFD and experimental observations, the vortices observed in the simulations span the entire droplet, unlike those observed in experiments, which are generally confined in the bottom half of the droplet. This difference is possibly due to the fact that the simulations are only two-dimensional.

List of Publications:

1. **DK Mishra**, D Mohanty, R Gupta, A Singh, "Effect of Bend on Film Thickness in Slug, Slug-Annular, and Annular Flow Regimes in Gas–Liquid Flow in a Microchannel", Ind. Eng. Chem. Res. 61 (37), 14081-14092, 2022.
2. **DK Mishra**, R Gupta, A Singh, "Velocity Field within Droplets Falling in Liquid Media inside a Rectangular Channel." Ind. Eng. Chem. Res. 63, 27, 12199–12209, 2024.
3. **DK Mishra**, R Gupta, A Singh, "Hydrodynamics and Mixing in Gas-Liquid Systems in a Tortuous Microreactor." (***Ready to submit***)
4. **DK Mishra**, R Gupta, A Singh, "Numerical Investigations of a Droplet Falling in Liquid Media." (***Under preparation***)

List of Book Chapters:

1. **DK Mishra**, R Gupta, A Singh. Coalescence of Disc-Shaped Falling Droplets Inside Quiescent Liquid Media, Springer Singapore, ISBN-13: 9789819960736, Fluid Mechanics and Fluid Power, Volume 5, 2022.
2. **DK Mishra**, R Gupta, A Singh. Study of gas-liquid flow in microchannel for sustainable energy application, Springer Nature Singapore, ISBN -13: 978-9819920877, Sustainable Energy Generation and Storage, 2022.
3. R Gupta, **DK Mishra**, Dynamic Instabilities and Their Control in Flow Boiling in Microchannels, Dynamics and Control of Energy Systems, 331-345, 2020.
4. **DK Mishra**, R Gupta, A Singh. Smooth Interface Annular Flow at U-Bend Microchannel: 2D Analytical Solution, Springer Singapore, Fluid Mechanics and Fluid Power, 2023. (***Accepted***)

Conferences

1. D K Mishra, R Gupta, A Singh. Smooth Interface Annular Flow at U-Bend Microchannel: 2D Analytical Solution, National Conference on Fluid Mechanics and Fluid Power (FMFP), December 20-22, 2023, IIT Jodhpur, India.
2. D K Mishra, R Gupta, A Singh. Effect of U-Bend on Liquid Film Behavior in Gas-Liquid Flow in Microchannel. 16th edition of Complex Fluids Symposium (COMPFLU –2022), Dec 19-21, 2022, IIT Kharagpur, India.
3. D K Mishra, R Gupta, A Singh. Coalescence of Disc-Shaped Falling Droplets Inside Quiescent Liquid Media, Fluid Mechanics and Fluid Power (FMFP), Dec 14-16, 2022, IIT Roorkee, India.
4. D K Mishra, R Gupta, A Singh. An analytical solution to gas-liquid smooth interface annular flow at U–bend microchannel. Research and Industrial Conclave (RIC), Jan 20-23, 2022, IIT Guwahati, India.
5. D K Mishra, R Gupta, A Singh. Study of gas-liquid flow in microchannel for sustainable energy application. North East Research Conclave (NERC), May 20-22, 2022, IIT Guwahati, India.
6. D K Mishra, R Gupta, A Singh. Experimental investigations of gas-liquid annular flow in straight and curved millimeter-size channel. 26th International Symposium on Chemical Reaction Engineering (ISCRE 26), Dec 5-8, 2021, New Delhi, India.
7. D K Mishra, R Gupta, A Singh. Gas-liquid flow visualization in U-bend millimeter-size channel. International Conference on Reaction Engineering (ICRE2021), May 07-08 2021, NIT Raipur, India.

Table of Contents

LIST OF TABLES

LIST OF FIGURES

List of Symbols

Nomenclature

D	Droplet diameter (m)
D^*	Theoretical diameter (m)
L	Column width (m)
l	Depth between glass slides (m)
V	Droplet volume (µl)
U_t	Terminal velocity (m/s)
ρ_c	Density of the continuous fluid (kg/m^3)

ρ_d	Droplet density (kg/m^3)
μ_c	Viscosity of the continuous fluid (Pa.s)
μ_d	Viscosity of the droplet fluid (Pa.s)
g	Acceleration due to gravity (m/s^2)
λ	Viscosity ratio (-)
τ	Shear stress (N/m^2)
d	Distance from the wall (m)
σ	Surface tension (kg/m.s)
μ_{GW}	Viscosity of glycerol-water mixture (Pa.s)
μ_{Si}	Viscosity of silicon oil (Pa.s)
Re	Reynolds number (-)
$U_{O,H}$	Average velocity of the surrounding fluid (m/s)
C_0	Pre-factor (-)
$R_{Droplet}$	Radius of the droplet (m)
Re	Reynolds number (-)
L	Column length (m)
U_{SG}	Gas superficial velocity (m/s)
U_{SL}	Liquid superficial velocity (m/s)
g	Gravity (m/s^2)
D	Diameter (m)
R	Channel radius (m)

B	Axial pressure gradient (N/m^3)
r_i	Interface distance from the center (m)
Ca	Capillary number (-)
We	Weber number (-)
Re	Reynolds number (-)
De	Dean number (-)
Su	Suratman number (-)
Bo	Bond number (-)
I_p	Pixel intensity value (-)
N	Number of pixels in scale (-)
S	Slip ratio (-)
σ	Surface tension (kg/m.s)
μ	Viscosity (Pa.s)
δ_1	Outer liquid film thickness (m)
δ_2	Inner liquid film thickness (m)
$\delta_{average}$	Mean of outer and inner liquid film thicknesses
ρ	Density (kg/m^3)

Chapter 1. Introduction

1.1 Background

In the past few decades, multiphase flows in confined channels have been increasingly popular because of their wide range of applications in various industries. Some of the areas where it is being used are pharmaceuticals, inkjet printing, chemical process engineering, electronics cooling, lab-on-a-chip devices, spacecraft thermal management applications, fuel cell, micro-electro-mechanical systems (MEMS), agriculture, biomedical devices (Al-Asadi et al., 2022; Bhosale and Acharya, 2020; Lakhera et al., 2022; Sarvar-Ardeh et al., 2023; Sharma et al., 2022; Tiwari et al., 2018; Wang et al., 2017; J. Zhou et al., 2020). Figure 1 shows some of the advance applications in droplet soft robotics (Čejková et al., 2017), liquid-liquid extraction on microfluidic chip (Xiong et al., 2016), fabrication of ultrasound responsive microparticle from capillary microfluidics for controlled drug delivery system (Huang et al., 2023) and use of stacked multichannel reactors for bulk chemical industry (Noishiki et al., 2013).

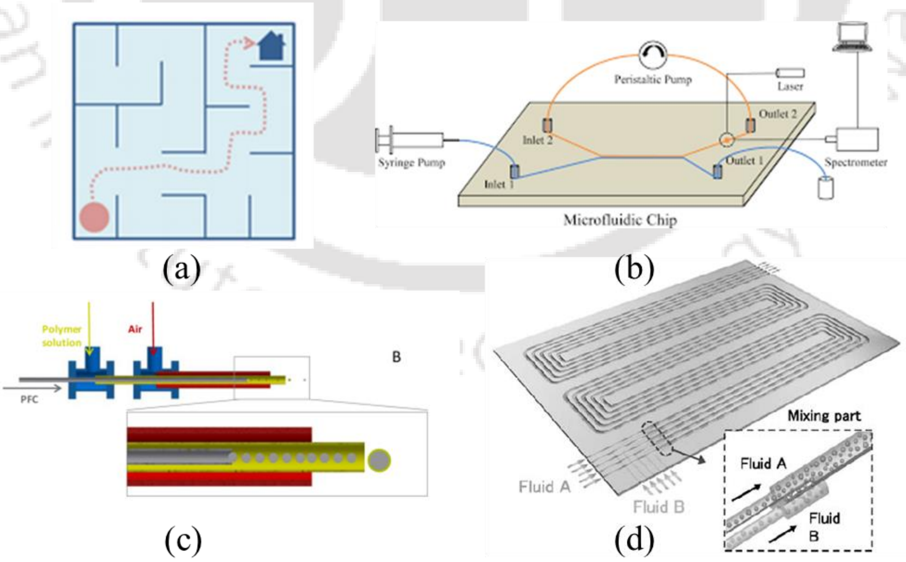

Figure 1.1 Application of microfluidics in (a) droplet soft robotics, (b) Liquid-liquid extraction, (c) Fabrication of ultrasound responsive microparticle from capillary microfluidics, and (d) Stacked multichannel reactors for bulk chemical industry

The range of their application is so vast that almost every engineering field is investigating it, and research centers are opening worldwide to explore its full potential (Keller and Pauly, 2009; Pandya et al., 2015; Rastog, 2018; Subasinghe et al., 2022; Tirre et al., 2019). All these applications utilize the advantages of high interfacial area density (surface area per unit volume), minimum waste, fast response, precise control, safety, and ease of numbering-up. Figure 1.2 shows a typical image of microfluidic lab-on-a-chip (Pandya et al., 2015).

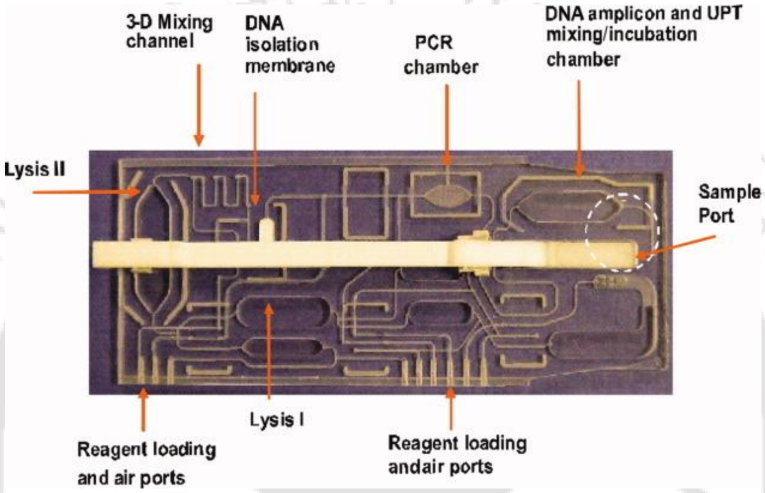

Figure 1.2 Microfluidic lab-on-a-chip used for early screening and diagnostics during dental visits developed by (Pandya et al., 2015).

Single-phase flow in small diameter channels is generally laminar due to the small characteristic length as the viscous force is dominant over inertial force. To increase the rate of heat and mass transfer in these systems, the additional means of mixing is often achieved by passive mixing caused by meandering (secondary flow or Dean flow) or innovative channel designs (Dean, 1927; Gaikwad et al., 2017). Gas-liquid and liquid-liquid flows in microchannels, however, develop different flow regimes. Depending on the flow rates, viscosity, and surface tension of liquids, different flow regimes such as bubbly, slug, slug-annular, annular, and churn flow occur in gas-liquid flow microchannels (Akbar et al., 2002; Chinnov et al., 2015; Hassan et al., 2005a; Kakac and Bon, 2008; Kawahara et al., 2002; Rawal et al., 2022; Thome, 2004; Triplett et al., 1999). Figure 1.3 shows the flow regimes observed in 1.045 mm diameter channel (Triplett et al., 1999). While some applications involve targeted flow regimes to operate (i.e., reactors, mixers, printers, etc.), others encounter most of the flow regimes (i.e., boiling). Higher interfacial area per unit volume available in these flow regimes enhances the heat transfer rate during heating and cooling applications in microchannels. Higher interfacial area density also increases the mass transfer rate in liquid-liquid or gas-liquid systems.

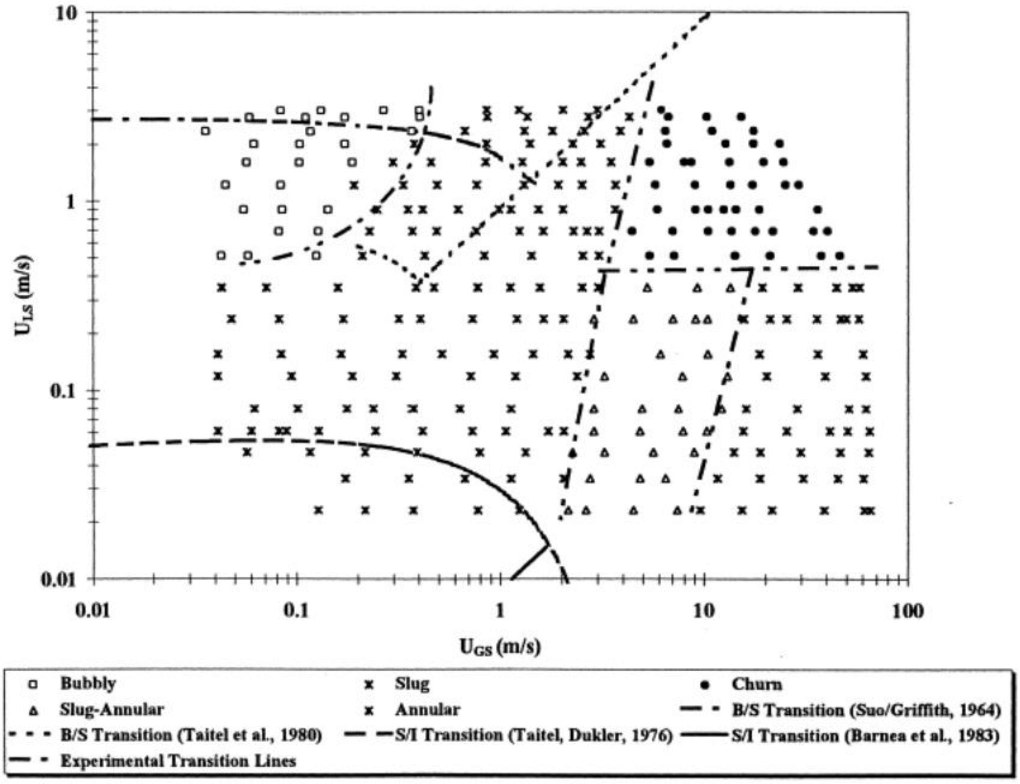

Figure 1.3 Flow regime map developed for 1.045 mm diameter channel by (Triplett et al., 1999)

The Bubbly flow regime occurs at high liquid and low gas flow rates in which small gas bubbles are dispersed in the liquid phase. Interfacial area density is highest in this flow regime but is difficult to control in terms of predictability, stability, and ease of management. A slug flow or Taylor flow pattern appears when small bubbles merge and form a bigger bubble that is the size of the channel diameter. The slug flow regime is better than the bubbly flow in terms of control. Flow physics in a single bubble represents the flow behavior of all the bubbles in the entire flow. Taylor flow also provides mixing inside both phases. Further, an increase in the gas flow rate results in the coalescence of Taylor bubbles and the formation of longer Taylor bubbles or wavy-annular flow with longer amplitude of waves at the interface. At the higher gas flow rate and low liquid flow rates, annular flow appears. A thin liquid film is present between the gas bubble/core and the wall in slug and annular flow regimes, which affects the heat and mass transfer rates. If the liquid flow rate is also increased along with that of the gas, churning occurs, in which the interface is disrupted, and different sizes of bubbles appear with disrupted interfaces.

Depending on the application, higher residence time or longer path length is required in order to utilize the benefit of slug flow or annular flow on a small chip area. A U-bend is often used for better space utilization to connect different straight microchannels to achieve a higher residence time or longer path length. The behavior of different flow regimes changes at the bend because of the secondary flow caused by the pressure gradient developed across the cross-section of the bend due to the change in the direction of the flow. Depending on the centrifugal force, the interface may deform or disrupt, changing the thickness of the liquid film, which can affect the heat transfer and mass transfer rates. Secondary flow-induced mixing or recirculation inside the liquid slug and gas bubble/core is crucial for the reactor design. Therefore, it is important to understand the flow physics of different flow regimes at the bend.

Similar to circulation inside bubbles in slug flow or Dean flow at the bend, recirculation patterns are observed inside a moving droplet in the case of immiscible liquid-liquid flow. A moving liquid droplet inside another immiscible liquid media develops internal circulation induced by the shear stress at the interface. Recirculations inside the droplet possess the capability for various industrial applications. In emulsion formation, these internal flows ensure effective mixing and dispersion of the dispersed phase within the continuous phase, crucial for stabilizing emulsions used in food products, cosmetics, and pharmaceuticals. For liquid-liquid extraction processes, internal recirculations enhance mass transfer rates between phases, optimizing the separation and purification of chemicals. Moreover, within underground reservoirs, understanding and controlling internal flows within oil droplets suspended in water is essential for maximizing oil recovery efficiency through strategies such as enhanced oil recovery techniques (Deng et al., 2014; Zhang et al., 2023). Many industries like food, pharmaceutical, petroleum, and chemical industries involve processes in which, knowledge of the hydrodynamics of droplets and their behavior is essential to optimize it. Using the small volume of droplet as a reactor is relatively newer area of exploration known as *droplet reactor*. It uses a single or series of droplets as a complete reaction unit (Joanicot and Ajdari, 2005; Pan et al., 2018; Zhang et al., 2023). In such a case, mixing inside the droplet is important, for example, to accurately determine the reaction rate. Viscosity and interfacial tension affect the recirculation strength, heat, and mass transfer rates. Key parameters such as terminal velocity, shape, internal circulation, and interface behavior are very important. Liquid-liquid contacting is required to transfer a solute from one phase to another for the reaction or extraction process. The knowledge of droplet dynamics in liquid-liquid contactors is essential to increase the transfer efficiency.

The strength of recirculation inside a moving droplet in immiscible liquid media is also very important for the design of a droplet reactor or other purposes. Because of the wide application, it is very important to understand the dynamics of droplets in confined geometries as most of the applications involve such environments.

1.2 Thesis Objectives

This study aims to understand the gas-liquid and liquid-liquid flow behavior in a millimeter-sized channel using experiments and numerical simulations. The first problem addresses the analysis of different flow regimes at U-bends. The second problem focuses on the recirculations inside falling droplets surrounded by liquid media. The specific objectives of the thesis are as follows:

Part A. Gas-liquid flow in circular cross-section curved microchannel

1. To quantify the liquid film thicknesses for different flow regimes using high-speed flow visualization.
2. To study the interface evolution and velocity field in different flow regimes using numerical simulations.

Part B. Falling droplet inside liquid media in a rectangular confined channel

3. To study the effect of droplet diameter and release location from the wall on the internal velocity field of a single droplet and during coalescence using particle image velocimetry.
4. To investigate the effect of viscosity ratio on internal recirculations and shape deformation inside a single droplet and during coalescence using numerical simulation.

1.3 Thesis Outline

The thesis has been presented in six chapters, including the introduction section (Chapter 1). The background and motivation of the research work are included in Chapter 1. The outline of the remaining chapters is as follows:

Chapter 2: An experimental study of gas-liquid flow in U-bend microchannel and analysis of the liquid film thickness surrounding the bubble/core are discussed.

Chapter 3: Three-dimensional CFD investigation of slug, slug-annular, and annular flow inside U-bend is discussed.

Chapter 4: The experimental investigation of falling droplets inside liquid media using PIV is discussed in this chapter.

Chapter 5: A numerical study of falling droplets inside liquid media from different diameters and release locations from the wall is discussed.

Chapter 6: The overall conclusions and the scope for future studies are addressed.

The literature review relevant to each chapter is included in the corresponding chapter itself and the details of methodologies are given in each chapter.

Part A:

Gas-liquid flow in circular cross-section curved microchannel

Chapter 2. Experimental study of gas-liquid flow in a curved microchannel

This chapter presents the studies on gas-liquid two-phase flow (for Newtonian liquids of different viscosities) in a microchannel with multiple U-bends using a high-speed camera. The flow regime transitions from slug to annular, with the liquid film between the wall and gas core/bubble becoming asymmetric in the bends due to centrifugal force. In slug flow, the inner wall film is thinner, while in annular flow, it is thicker. This transition is influenced by changes in the relative importance of gas and liquid centrifugal forces.

2.1 Introduction & Literature Review

Heat and mass transfer processes in several applications such as electronics cooling, process intensification (Zong and Yue, 2022), microreactors in the manufacturing of pharmaceutical and fine chemicals (Günther and Jensen, 2006), and enhanced oil recovery (Kumari et al., 2019; Sharma et al., 2021) involve complex gas-liquid flows in small diameter channels. In recent decades, the miniaturization of equipment has shown great applicability in terms of yield, design, handling, and safety. Gas-liquid flow in a small diameter channel is beneficial for enhancing heat and mass transfer rates due to its large interfacial area density. Based on the gas and the liquid flow rates, viscosity, and surface tension of liquids, different flow regimes such as bubbly, slug, slug-annular, annular, and churn occur in microchannels (Chung and Kawaji, 2004; Hassan et al., 2005b; Kawahara et al., 2009; Lakehal et al., 2012; Triplett et al., 1999). While most of the studies are done with circular cross-section microchannel, some researchers used square microchannel and observed similar flow regimes (Chung and Kawaji, 2004; Dessimoz et al., 2008; Kawahara et al., 2002; Kolb and Cerro, 1991; Simmons et al., 2002). Square channels show irregular flow patterns for the case where circular cross-section channels show annular flow regimes. There are significant variations in the transition of flow regimes between square and circular cross sections. Corner flow in square cross section channel is reported to be laminar even at very high turbulent flow at the core (Zhao and Bi, 2001).

The flow of distinct and very small diameter bubbles in the continuous liquid stream is termed as bubbly flow. When bubble size increases up to the channel diameter, it elongates with a further increase in the bubble volume, taking a capsular shape, and a train of alternate gas bubbles and liquid slugs is formed. This is known as the slug or Taylor flow regime (Gupta et al., 2010). Further, an increase in the gas flow rate results in the coalescence of adjacent bubbles and the development of annular flow with gas in the core and liquid film on the wall. The thickness of the liquid film formed on the wall varies depending on the gas and liquid flow rates and their properties (Ashwood et al., 2015). The flow field in the liquid film plays a significant role in the heat and mass transfer to/from the wall of the microchannels (Chaurasiya and Singh, 2022; Ge et al., 2020; Ramji et al., 2019). Therefore, extensive numerical and experimental studies (Angeli and Gavriilidis, 2008; Gupta et al., 2010; Haase et al., 2016) on gas-liquid two-phase flow behavior have been reported in the past. The thickness of the liquid film varies with flow regime change (Suo and Griffith, 1964). Recently, Etminan et al. (2021) have summarized the film behavior in gas-liquid flow in microchannels.

Based on the fluid properties and flow rates of the phases, capillary number $\left(Ca = \frac{\mu U}{\sigma}\right)$, and Reynolds number $\left(Re = \frac{D\rho U}{\mu}\right)$ are two important non-dimensional groups governing the flow behavior. Weber number (We), the product of capillary and Reynolds numbers, is another important non-dimensional group, especially when inertia is non-negligible. Suratman number $\left(Su = \frac{Re}{Ca} = \frac{D\rho\sigma}{\mu^2}\right)$ is another key dimensionless group for the flow regime transition from bubbly to slug and slug to the annular flow regime (Colin et al., 1996; Jayawardena et al., 1997;

Sen, 2010, 2009). Note that the Suratman number is a function of channel size and fluid properties only.

Bretherton (1961) derived an expression for film thickness surrounding a long Taylor bubble. His expression is applicable at the low capillary numbers ($Ca < 5 \times 10^{-3}$). Further, Aussillous and Quéré proposed an empirical model which is applicable up to moderate value of capillary numbers ($Ca < 1$) (Aussillous and Quéré, 2000). Klaseboer et al. (2014) derived an extended Bretherton's model for liquid film thickness similar to that of Aussillous and Quéré. It is applicable at moderate values of Ca and converges to Bretherton's solution at low values of Ca. The effect of the inertia on the liquid film thickness in terms of We and Ca is investigated for the Taylor bubble in a straight rectangular microchannel by Han et al. (2009) using a laser focus displacement meter.

Several applications may require long microchannels with good passive mixing (Lee et al., 2016; Pang et al., 2020). One such example can be a microreactor in which a long residence time of gas and liquid phases is desired (Fernández-Maza et al., 2022). This is often achieved by connecting several straight sections via U-bends (Al-Rawashdeh et al., 2012). A similar arrangement is also useful to increase radial mixing as the curvature at the bends induces secondary flow in the transverse direction, known as Dean flow (Dean, 1927).

While there are a number of studies investigating gas-liquid flow in straight microchannels (Leung et al., 2012; Mandal et al., 2008; Ratulowski and Chang, 1989), the studies on two-phase flow in curved microchannels are limited (Fries et al., 2008; Günther et al., 2004; Guo et al., 2019; Muradoglu and Stone, 2007; Y. Zhou et al., 2020). In the slug flow regime in straight channels, recirculation patterns are established in the liquid slugs, which can be observed in the bubble frame of reference. The presence of Dean vortices makes this problem further interesting as the mixing would occur in the axial as well as radial directions, resulting in complex, three-dimensional vortices.

Günther et al. (2004) studied gas-liquid flow in a rectangular microchannel having straight and meandering sections using micro-particle image velocimetry (μPIV) and experimentally observed recirculations in the liquid slug region which switch their position across the centerline of the channel because of the bending. Han et al. (2015) found that the film thickness decreased with an increase in the superficial gas velocity in gas-liquid annular flow. Using a conductance probe Wang et al. (2018) observed that average liquid film thickness decreased with an increase in the gas superficial velocity for a given liquid superficial velocity.

Zaloha et al. (2012) observed symmetric recirculations in the liquid slug straight section and non-symmetric recirculation in the meandering section using μPIV. Peng Zhang et al. (2018) studied mass transfer characteristics of Taylor flow (CO_2 and Water) in a unit cell (containing one bubble and one slug) of serpentine rectangular microchannel using high speed photography.

Muradoglu and Stone (2007) studied the motion of a long bubble in a curved microchannel for small capillary numbers ($Ca < 0.01$) and observed the inner liquid film to be thinner than the outer liquid film. Core-annular flow in curved channels has been investigated theoretically by Picardo and Pushpavanam (2013a). They suggested that the gently curved channel does not affect the velocity profile significantly. However, large curvature can greatly affect the velocity profiles. It is also concluded that in core-annular flow at the curved region, gas and liquid may affect the flow field inside each other, resulting in liquid displacement from the outer wall to the inner wall.

The effect of U-bend on two-phase annular flow in serpentine microchannel is investigated by Wu and Sundén. (2019) They observed that the centrifugal force breaks the annular core into slug and droplet. López et al. (2020) studied air-water annular flow in horizontal U-bend experimentally and numerically. They investigated the effect of the curvature of bend on gas holdup and liquid film distribution in a channel of 14 mm diameter. Yao et al. (2020) studied liquid-liquid Taylor flow in rectangular microchannel consisting of straight and U-bend sections for the viscous effect of different fluid combinations on mass transfer characteristics. They observed a non-crossing pattern (inner and outer vortices do not change their position while passing through the bend) for smaller flow rates and a crossing pattern at higher flow rates.

Based on the above review of literature, it is clear that there have been extensive studies of slug flow regimes in straight microchannels. However, there are limited studies on annular flow microchannels. Further, the investigations on the slug as well as annular flow regimes in the curved microchannels are limited. Two-phase flow in curved channels shows tremendous opportunity to enhance mixing due to secondary flow in the radial direction and axial mixing in the liquid slugs (Vashisth et al., 2008). Liquid film thickness significantly affects the phenomena at the curvature. Therefore, it is essential to investigate the flow in curved channels and measure the liquid film thickness.

This study focuses on the effect of fluid properties such as viscosity, density, and surface tension on the liquid film thickness in the slug, slug-annular, and annular flow regime in a 1 mm diameter circular glass channel having multiple U-bends. Mixtures of de-mineralized (DM) water and ethylene glycol in various ratios are used as test liquids. Images of the phase distribution at the U-bend are captured using a high-speed camera and processed to extract film thickness evolution with time at certain locations. The effect of different flow parameters on the film thickness is analyzed.

2.2 Experimental Methodology

Experiments are performed to quantify liquid film thickness in gas-liquid flow in a microchannel by high-speed imaging. Images are processed to identify the gas-liquid interface. The identified gas-liquid interface is used to characterize the flow regime. A schematic of the experimental setup is shown in Figure 2.1. It consists of a compressed nitrogen gas cylinder, a gas regulator, a syringe pump, a gas mass flow controller, a T-junction, the test section, a high-speed camera, an LED light source, and a computer to record, save and post process the images, and a container to collect the discharged liquid. The liquid and gas lines also consist of unions and check valves to connect the tubes of different diameters and restrict the backflow, respectively.

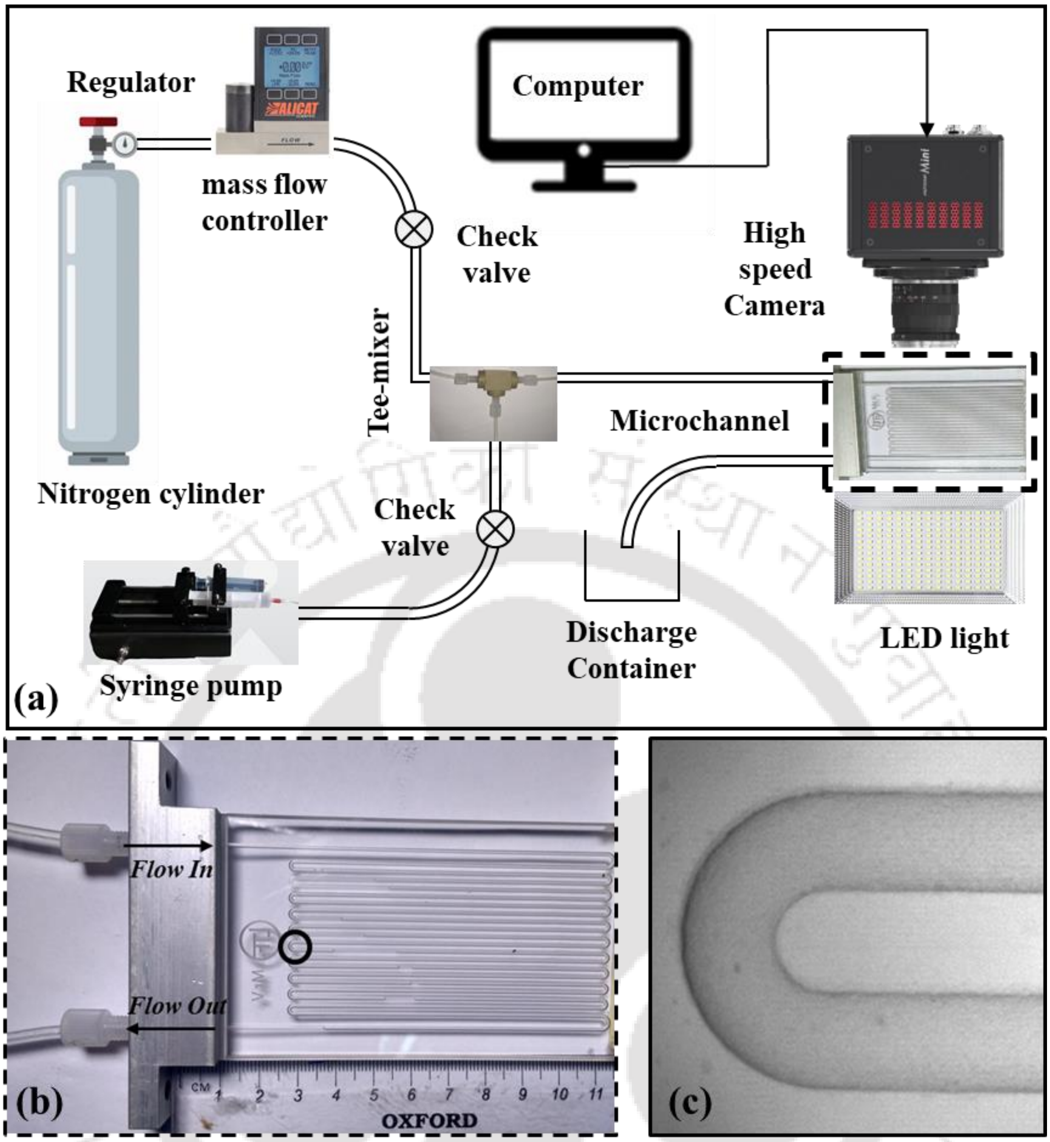

Figure 2.1 (a) Schematic diagram of the experimental setup (b) Enlarged view of microchannel assembly showing flow inlet and outlet directions and (c) Image of the 1 mm diameter, circular cross-section, U-bend from the top.

A transparent glass microreactor (LTF Germany) having a circular cross-section of diameter (D) 1 mm and a total length of ~2 m is used as the test section. As shown in Figure 2.1b, it consists of both straight and curved sections. Figure 2.1c shows an enlarged view of the U-bend. There are 21 U-bends (0.5 mm inner radius of curvature) and 20 straight sections (each 8.5 cm long), and two long straight sections about 10 cm long at the inlet and outlet. Channel is made by hemispherical grooving of half surfaces and joined together to form an internal channel in a transparent glass sheet.

The different liquid phases are de-mineralized and de-ionized water combined with ethylene glycol in various proportions (26% and 50%) and toluene. As the gas phase, high purity nitrogen (>99.9%) is used. The properties of test fluids are given in Table 2.1. Note that the notations W, 26EG, 50EG, TOL are used for liquids in the rest of the article. The liquid is delivered at a controlled, calibrated rate through a syringe pump (Holmarc *HO-SPLF 2*). A Luer lock syringe of volume 60 ml is used in the syringe pump. The flow rate of the syringe pump can be varied between 0.0021 ml/min to 83.3 ml/min. The maximum pressure offered by the syringe pump is 300 kPa. All experiments are conducted at the room temperature (~25°C) and near atmospheric pressure. Nitrogen gas is delivered from a gas cylinder through a regulator (*Aneer Engineering Works*). The gas flow rate is controlled using a gas mass flow controller (*MC-Series < 5 slpm*, ALICAT).

Table 2.1 Fluids used in the experiments and their properties

Fluids	**Density (ρ) (kg/m^3)**	**Viscosity (μ) (Pa·s)**	**Surface Tension (σ) (N/m)**
Water (W)	998	0.00098	0.073
26% EG (26EG)	1027	0.002	0.061
50% EG (50EG)	1055	0.004	0.057
Toluene (TOL)	867	0.00056	0.028
Nitrogen (N_2)	1.145	0.00002	-

Two phases are mixed at the T-junction, as shown in Figure 2.1a. T-junction has circular cross-section and the gas and liquid streams meet in the mixer perpendicular to each other. Connecting tubes of 3.2 mm diameter connect the syringe pump to check valves and gas flow controller to T-junction. The inlet of the test section is connected to the T-junction and outlet to the collecting tank. Flow visualization is performed using an 8-bit depth High speed Camera

(Model: Mini UX50, Make: *PHOTRON*) and a 4X zoom lens. The camera's maximum frame rate is 2000 fps at a 1280 × 1024 pixels resolution and a minimum exposure time of 1 μs. The camera is positioned vertically above the channel using a tripod stand. The test section is mounted horizontally. The LED light (*YONGNUO YN900*) is placed below the channel (as shown in Figure 2.1), and a light diffuser sheet is used between the channel and the light source to capture backlit images. The field of view is approximately 2 cm × 2.5 cm.

2.2.1 Image Acquisition and Processing

Based on the flow speed, the images are captured with pixel resolutions of 1280 ×1024 at 2000 frames per second (fps) and 1280 ×512 at 4000 fps. Low flow velocity bubbles are captured at 2000 fps without showing motion blur when adjusted by the exposure time (200-500 μs). At high flow velocities, 4000 fps is used with an exposure time of 100-250 μs to avoid motion blur of moving bubbles. Images are captured using the Photron FASTCAM Viewer software and stored in the computer memory.

Images are processed using ImageJ software, (Schindelin et al., 2012) an open-source image processing tool. The background of the image contains unevenly illuminated spots which are removed using rolling ball algorithm (Sternberg, 1983). According to the images, the radius of the rolling ball is varied from 30-50 pixels. A monochromatic image contains a grey shade, which is undesirable in interface detection. Thresholding is applied to capture a clear interface of objects in the image, which converts the image into binary format (Lai and Rosin, 2014). In thresholding, each pixel is compared with the threshold and is consequently converted into either a black or a white pixel. The average intensity of the gas phase and liquid phase region is chosen as a thresholding criterion (grey level of 188-194 on a 0-255 scale) for the segmentation of the boundary of phases. Pixels with intensity above the threshold value are considered liquid, and the rest are considered gas phases (Patel et al., 2015). For a uniformly illuminated image with less noise, the intensity histogram is bimodal, and segmentation is easily possible using a global threshold value. Minimum cross-entropy thresholding (Li and Lee, 1993) is used as a global thresholding method. However, if an image is non-uniformly illuminated and contains noise, global thresholding fails, and for such cases, local thresholding is applied. The term ‘local’ refers to the fact that the threshold for each pixel is calculated based on the properties of the image within a certain radius of neighboring pixels.

Noise in the segmented image is removed using the median filter to smoothen the interface. It is done by substituting each pixel with the median value of its neighboring pixels within a certain radius. A suitable radius value is selected based on the interface noise level. Figure 2.2 shows a schematic of steps involves in image processing.

2.2.2 Film Thickness Calculation

To capture the temporal variation of the film thickness at a particular location, a straight line (from the outer to the inner wall, the length of the line is 1 mm) is drawn on the original image, as shown in Figure 2.2. This line calibrates the physical spatial dimension to the pixel dimension. Spatial resolution varies from 16-18 μm/pixel. Segmentation of the image results in two types of pixel intensity values: 0 and 255. All the regions with the gas phase are marked with a pixel intensity value of 255, and all the liquid phase regions are marked with a pixel intensity value of 0. Liquid film thickness at the location can be calculated using Eq. (2.1.

$$\delta = \frac{\sum I_p}{255N} \tag{2.1}$$

In the above equation, I_p is the pixel intensity value, and N is the number of pixels occupied in 1 mm. The film thickness calculated based on the line joining inner to outer wall is sum of inner and outer film thicknesses. Therefore, two different lines are drawn from the center of the channel to outer and inner wall separately. It is necessary to create separate line to differentiate the inner and outer film thickness values. Liquid film thickness calculated from these two lines represents inner and outer liquid film thicknesses. Hence, in the case of a liquid slug occupying the whole area of the channel, film thickness calculated from one line is 0.5 mm.

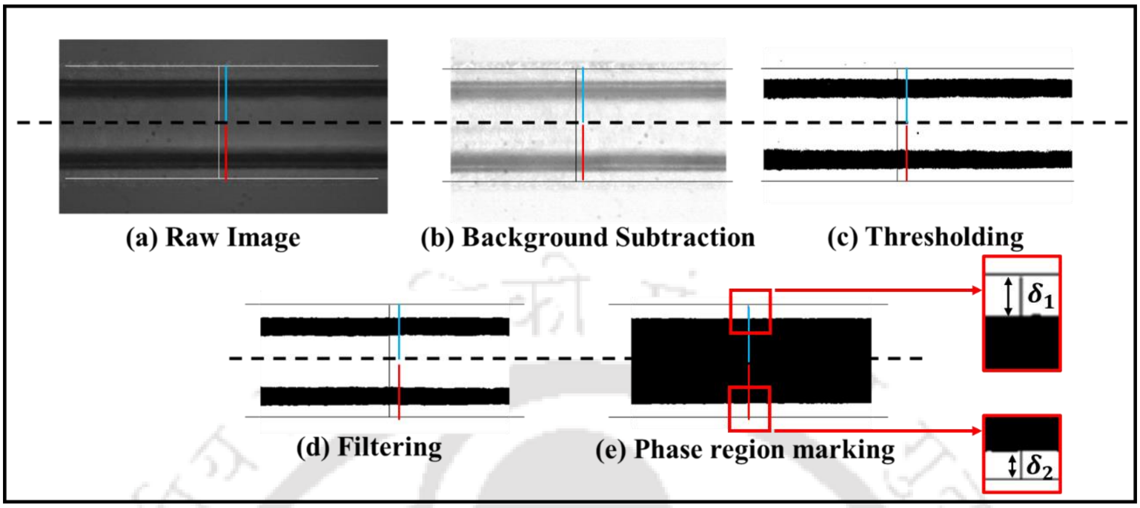

Figure 2.2. Steps of image processing applied to raw images. (i) Raw image captured in experimental condition, (ii) Background noise subtraction, (iii) Thresholding, (iv) Filtering and (v) Phase region marking.

Measurements are taken at the middle U-bend (12th from the inlet, marked by a circle in Figure 2.1) where they are supposed to be independent of the number of U-bends. The liquid distribution at the bend is independent of the position of the bend (far away from the inlet and exit) at which measurement is made (see image snapshot in Figure 2.3). This is further corroborated by the time-averaged film thicknesses shown in Figure 2.3

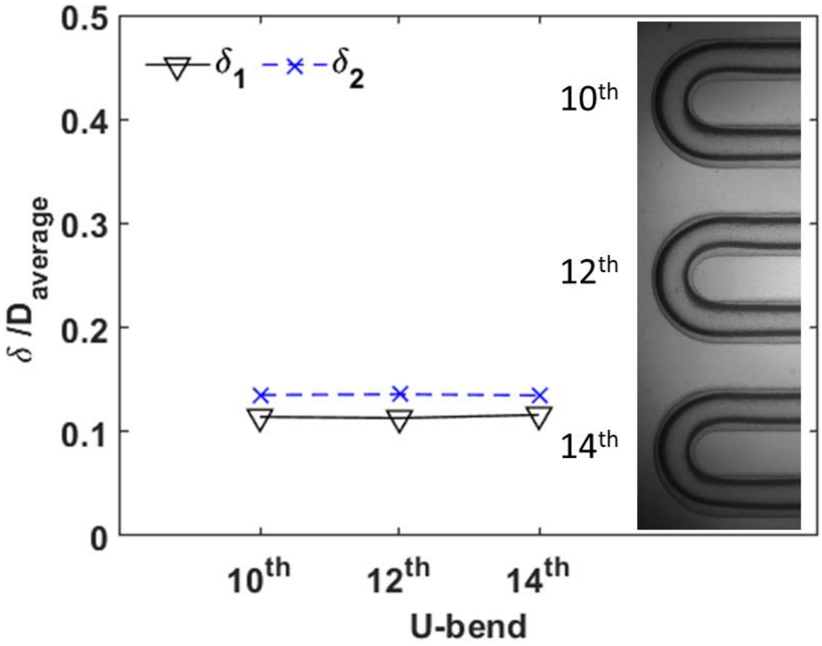

Figure 2.3 Time averaged outer (δ_1) and inner (δ_2) film thickness at different bends (10th, 12th, and 14th from the inlet) showing that measurement location is unaffected by the inlet and exit effect of the channel

Figure 2.4 shows the flow direction and measurement locations where the interface is captured, and liquid film thickness is calculated. Location X_1 and X_5 are positioned at a distance of 6D from the inner wall of the middle of the bend. Locations X_2 and X_4 are chosen just before the entrance and exit of the bend. Location X_3 is at the center of the bend. δ_1 is liquid film thickness on the outer wall while δ_2 is the liquid film thickness on the inner wall. Experiments are repeated 4 times and the maximum experimental error observed is 3.9%.

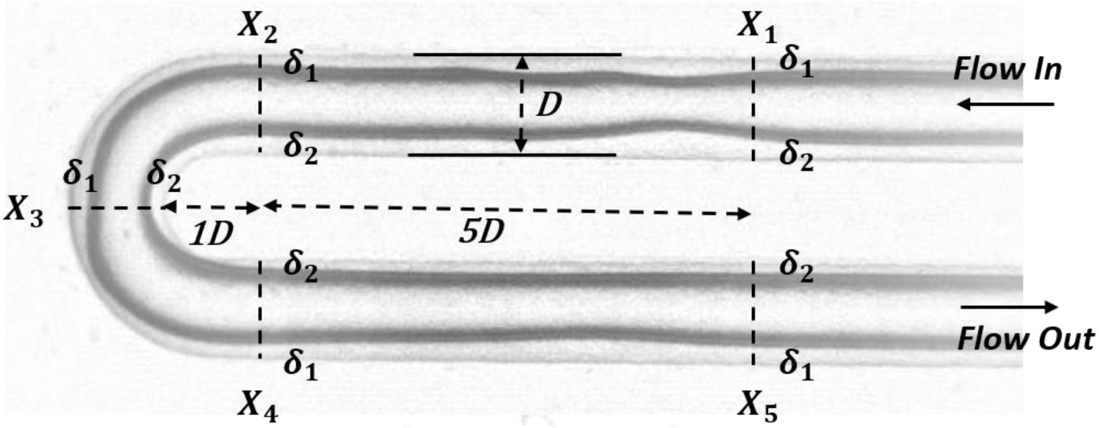

Figure 2.4. Longitudinal cross-section of the channel (diameter D) showing the measurement locations (X_1, X_2, X_3, X_4, and X_5). Liquid film thickness on the outer boundary of the channel is termed δ_1, and film thickness on the inner boundary of the channel, δ_2.

2.3 Results and Discussion

2.3.1 Flow Regime Map

Experiments are performed in a microchannel of circular cross-section over a range of gas and liquid flow rates, as given in Table 2.2. A map indicating the flow regimes observed on the U_{SG}-U_{SL} plane is shown in Figure 2.5. U_{SG} and U_{SL} are the superficial velocities of the gas and the liquid phases, respectively. Representative images of typical flow regimes are also shown. As can be seen in the figure, the experiments have been performed at low liquid flow rates and over a large range of gas flow rates. There is no unanimity in the literature on the nomenclature of these flow structures because of the considerable variability in flow structures reported in different regimes. We term the annular flow regime as the regime in which a continuous gas core surrounded by a thin liquid film on the wall is observed. However, there are always waves present on the interface. The amplitude and frequency of these waves depend on the gas and liquid flow rates and fluid properties. At very high gas flow rates, the wave amplitude is relatively small, and the interface appears to be nearly smooth. However, in the case of lower gas flow rates, the wave amplitude is larger and such regime is termed as wavy-annular flow regime in the following sections. Note that no differentiation has been made between the wavy-annular and annular flow regimes in Figure 2.5. In the slug-annular flow regime, long or very long gas bubbles followed by short liquid slugs are observed. However, unlike the slug or Taylor flow regime in microchannels, the flow is not periodic in the slug-annular flow regime. In some cases, a slug flow regime is observed, which is differentiated from the slug-annular flow regime based on the periodic occurrence of alternate gas bubbles and liquid slugs. The bubbles are very long in these cases too.

Table 2.2. Typical Superficial velocities used for the experiments

U_{SL} (m/s)	0.01	0.02	0.04	0.06	0.1	0.2	-
U_{SG} (m/s)	2.34	4.68	7.024	11.71	16.38	23.41	30.44

An increase in the gas velocity results in the coalescence/merging of gas bubbles leading to an annular flow regime as the gas inertia ($\rho_G U_G^2$) is able to overcome the surface tension ($\sim 2\sigma/R$). Equating the two effects, the critical gas superficial velocity at which the flow regime transitions to annular flow can be given by Eq. (2.2.

$$U_{SG,Critical} = \sqrt{\frac{2\sigma}{\rho_G R}} \tag{2.2}$$

For air-water flow, the value of critical superficial velocity comes out to be ~16 m/s, which is closer to the value observed in the experiments. It may be noted that the slug-annular flow regime is highly transient, and sometimes, two consecutive bubbles may merge, and the flow regime may appear as wavy-annular intermittently.

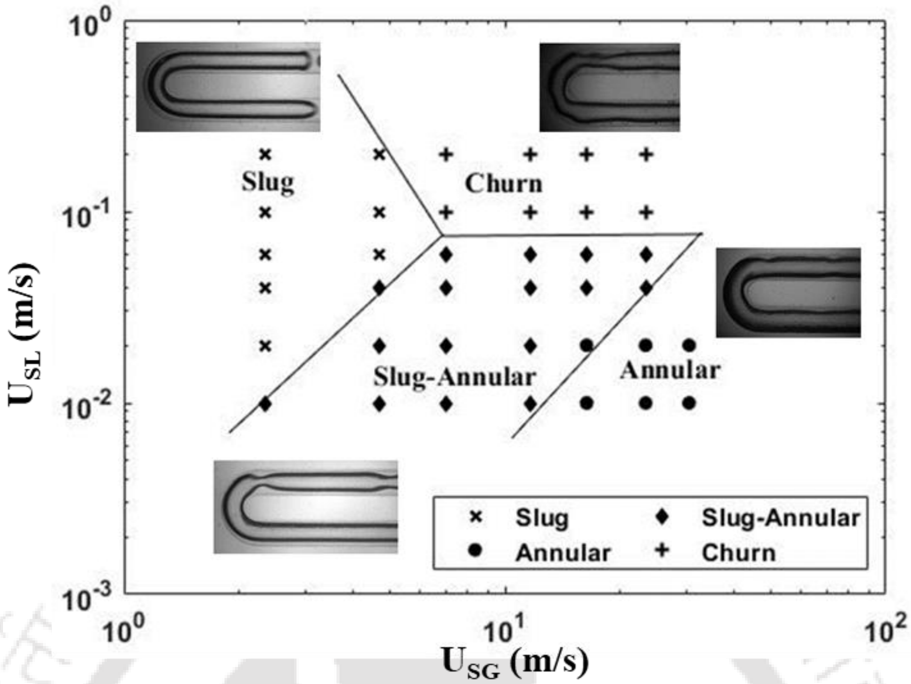

Figure 2.5. Flow regime map for 1 mm diameter, U-bend circular channel, and representative images of (a) slug, (b) slug-annular, (c) annular flow, and (d) churn flow regimes observed in the experiments.

Unlike the axisymmetrically distributed liquid film in straight channels, the liquid film is observed to be distributed non-symmetrically in the glass microchannel used in this work. The thickness of the liquid film on the inner and outer walls of the bend is observed to be different. This can be attributed to the different centrifugal forces experienced by the gas and liquid phases.

2.3.2 Time Evolution of Film Thickness

Slug Flow

Figure 2.6(i) shows the variation of dimensionless film thickness with time for four different liquids at U_{SL} = 0.1 m/s and U_{SG} = 2.34 m/s at three locations (X_1 X_3 and X_5). Representative instantaneous images indicating the flow direction and observation points are also shown in Figure 2.6(ii). Note that when slugs of the liquid pass through any of the observation points, δ_1

and δ_2 have value of 0.5, indicating the presence of only liquid. When the bubble passes through the location, the liquid film thicknesses vary between 0 and 0.5. At location X_1 (upstream of the bend), δ_2 is always greater than δ_1 for all the liquids, but as we move towards X_3 and X_5, δ_2 becomes smaller than δ_1.

Table 2.3 Dimensionless parameters at U_{TP} = 2.44 m/s, centerline radius of curvature (R_c) = 1 mm

Fluids	$Ca = \frac{\mu U_{TP}}{\sigma}$	$Re = \frac{D\rho U_{TP}}{\mu}$	$We = Re.Ca$	$De = Re\sqrt{\frac{D}{2R_c}}$	$Su = \frac{D\rho_L \sigma}{\mu_L^2}$	$Bo = \frac{\Delta\rho g D^2}{\sigma}$
W	0.033	2485	81.39	1757	75858	0.134
TOL	0.049	3778	184.35	2671	77410	0.303
26EG	0.080	1253	100.24	886	15662	0.165
50EG	0.171	644	110.19	455	3758	0.181

Using a two-dimensional theoretical analysis, Muradoglu and Stone(Muradoglu and Stone, 2007) showed that for a long bubble passing through a curved section, δ_2 is lower than δ_1 at low capillary numbers. This is also observed in the present experiments, as shown in Figure 2.6(i). In the middle of the curved section (location X_3), δ_2 is always observed to be lower than δ_1. This indicates that in the curved region, the bubble is nearer to the inner wall and the liquid film on the outer wall is thicker than that on the inner wall. However, the difference between the thicknesses of the inner and outer wall films is observed to decrease with an increase in Ca (as can be understood from Table 2.3). Downstream of the bend, at location X_5, the same pattern is observed, i.e., δ_2 is always smaller than δ_1. However, the difference between δ_1 and δ_2 is smaller at X_5 compared to that at X_3. This is probably because the centrifugal force that causes the difference in film thickness ceases to act downstream of the bend.

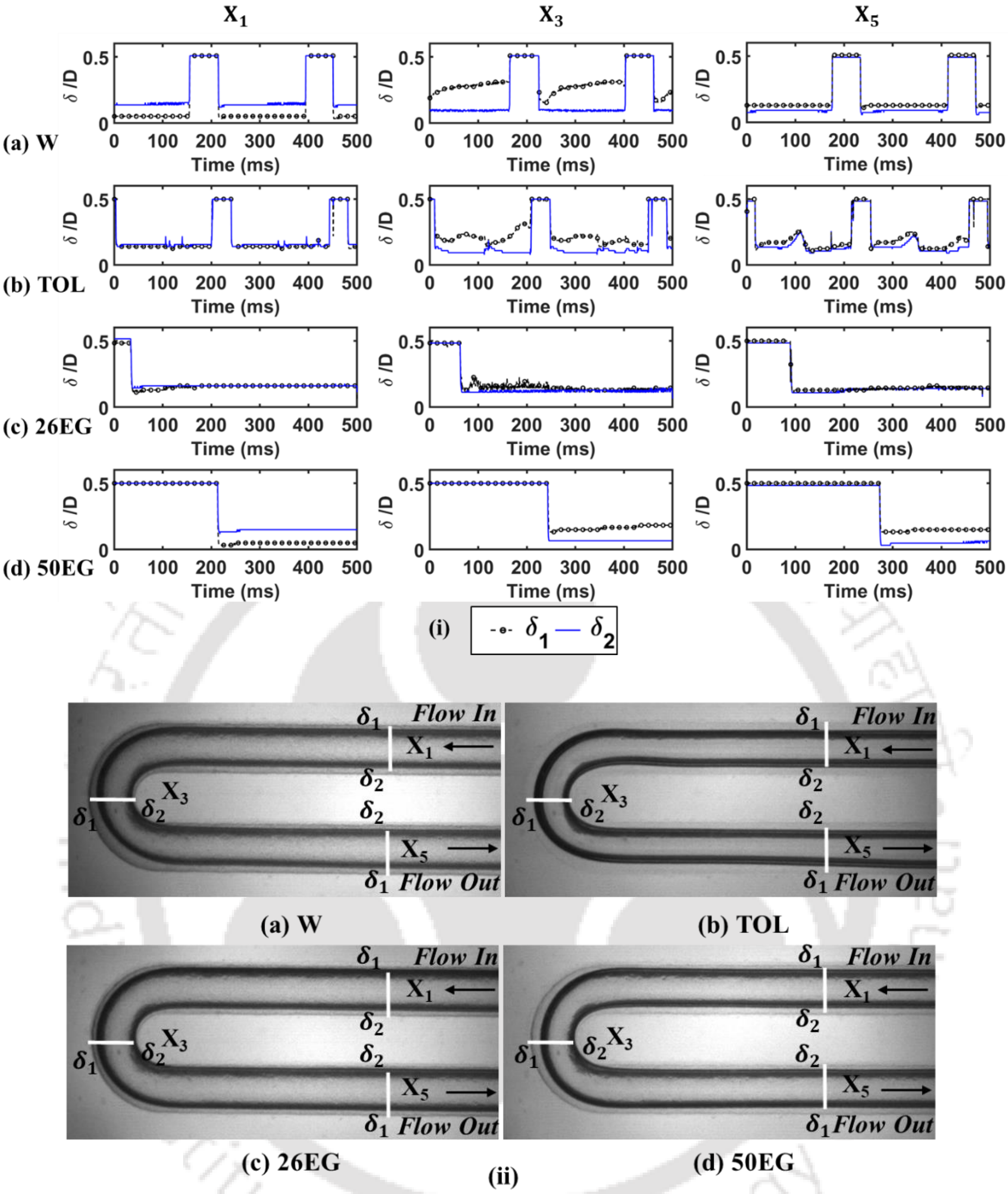

Figure 2.6. (i) Film thickness variation with time and (ii) Instantaneous snapshot of the long bubble in slug flow for (a) W, (b) TOL, (c) 26EG, and (d) 50EG at U_{SL} = 0.1 m/s, U_{SG} = 2.34 m/s. Ca increases from (a) to (d). Note that δ_1 denotes outer film thickness and δ_2 denotes inner film thickness.

Slug-annular and annular flow

Figure 2.7(i) shows the film thickness variation for four liquids, W, TOL, 26EG, and 50EG, with time at location X_3 for U_{SG} = 7.02, 16.38, and 23.41 m/s. U_{SL} is 0.02 m/s for all the cases.

Figure 2.7(ii) shows the instantaneous image of slug, slug-annular and annular flow regimes for water-nitrogen flow. At U_{SG} = 7.02 m/s (slug-annular flow), δ_2 is higher than δ_1 for all the liquids except for 50EG (high viscosity liquid), for which δ_1 is more than δ_2. With the increase in U_{SG}, the difference between δ_1 and δ_2 increases. The gas core moves towards the outer curvature, and the outer liquid film becomes thinner. This behavior at the curvature is opposite to that observed in the slug flow regime in which the gas bubble sticks to the inner wall and δ_2 becomes smaller than δ_1. This phenomenon is observed for all the liquids at U_{SG} = 16.38 m/s and 23.41 m/s, as shown in Figure 2.7(ii).

Table 2.4 Dimensionless parameters at U_{TP} = 7.04 m/s, 16.40 m/s, and 23.43 m/s at centerline radius of curvature (R_c) = 1 mm

U_{TP} (m/s)	**Fluids**	**Ca**	**We**	**Re**	**De**	**Su**	**Bo**
7.04	W	0.095	677.57	7169	5069	75858	0.134
	TOL	0.141	1534.64	10899	7707	77411	0.303
	26EG	0.231	834.42	3615	2556	15662	0.165
	50EG	0.494	917.32	1857	1312	3758	0.181
16.40	W	0.220	3681	16701	11809	75858	0.134
	TOL	0.328	8338	25391	17954	77411	0.303
	26EG	0.538	4533	8421	5955	15662	0.165
	50EG	1.152	4984	4326	3059	3758	0.181
23.43	W	0.315	7505	23860	16872	75858	0.134
	TOL	0.469	16998	36275	25650	77411	0.303
	26EG	0.768	9242	12031	8507	15662	0.165
	50EG	1.644	10160	6179	4370	3758	0.181

Temporal plots show the presence of high amplitude waves on the interfaces for U_{SG} = 7.02 m/s. These oscillations are observed to decrease with an increase in U_{SG}. The wave properties on the inner and outer interfaces are not symmetric. The wave amplitude at the inner interface is large, whereas the outer interface is relatively quiescent for U_{SG} = 23.41 m/s. The amplitude of the wave at the inner interface decreases with an increase in U_{SG}. As Ca increases (refer to Table 2.4), the wave amplitude at the outer interface decreases for all the cases. However, no significant dampening of wave amplitude is observed at the inner interface with increase in Ca.

The origin of the waves on the interface in the annular flow has been studied extensively (Govindarajan and Sahu, 2013; Usha and Sahu, 2019). Sahu (2021), using linear stability analysis, has shown that increasing surface tension destabilizes the long wave perturbation at the interface for gas-liquid flow at constant density, viscosity, and Re. Similar destabilization is also observed for U_{SG} = 7.02 m/s. However, viscosity increases with different liquids (water to 50% EG) resulting in the increased value of Re along with the effect of curvature at the interface.

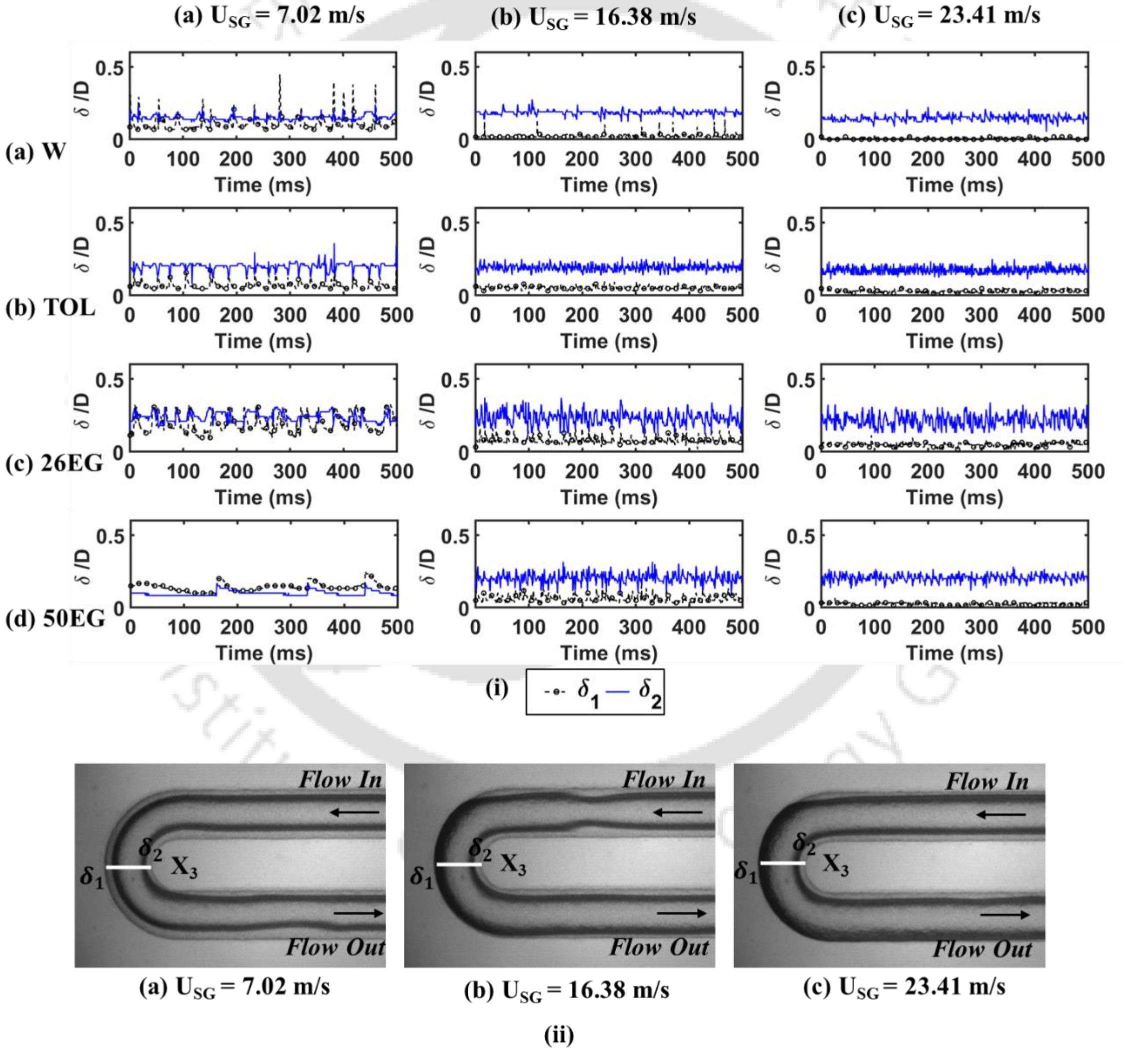

Figure 2.7. (i) Film thickness variation with time at X_3 for all the liquids and (ii) Instantaneous snapshot of the water-nitrogen annular flow regime at U_{SL} = 0.02 m/s, and (a) U_{SG} = 7.02 m/s, (b) U_{SG} = 16.38 m/s, (c) U_{SG} = 23.41 m/s. Note that the Ca increases from (a) to (d).

Slug to annular transition

Figure 2.8(i) shows the time evolution plot of inner and outer films at three locations, X_1, X_3, and X_5, and the effect of transition from slug to annular flow regimes. Experimental conditions are the same as Sections 3.2.1 and 3.2.2 hence the results are shown only for water-nitrogen flow. Figure 2.8(ii) shows the instantaneous snapshot of the flow.

At X_1, the inner film (δ_2) is always greater than the outer film (δ_1), irrespective of the flow regimes. However, wave frequency increases with U_{SG} as the flow regime transitions from slug to annular. At X_3, the inner film (δ_2) is smaller than the outer film (δ_1) in the slug flow regime but becomes greater than the outer film (δ_1) in the annular flow regime. This transition occurs in the slug-annular flow regime, as shown in Figure 2.8(ii).

At X_5, the outer film (δ_1) is observed to be greater than the inner film (δ_2) in the case of slug flow, but as the transition occurs, it starts decreasing in magnitude and becomes smaller than the inner film (δ_2) in the case of the annular flow regime. High amplitude waves are present in case of slug-annular flow at all locations. The wave amplitude is observed to reduce (ripple flow) when the regime changes to annular flow.

In slug flow, inner film (δ_2), which is greater than outer film (δ_1) at X_1, becomes smaller when the flow reaches X_5. This transition can be attributed to the curvature effect on the film. Similar switching behavior is also observed by Günther et al. (2004) This switching of inner and outer film thicknesses is observed when the flow regime changes to slug-annular (U_{SG} = 7.02 m/s). Interfaces become highly wavy in nature at all locations (X_1, X_3, and X_5). With an increase in U_{SG} to 16.38 m/s, the switching of film thicknesses on the inner and outer wall diminishes, and almost the same magnitude is observed at X_5 for both films. After the transition, no switching is observed in the case of annular flow, and the outer film (δ_1) remains smaller than the inner film (δ_2) at all locations (X_1, X_3, and X_5). Interface wave amplitudes are also observed to be smaller than slug-annular flow regimes.

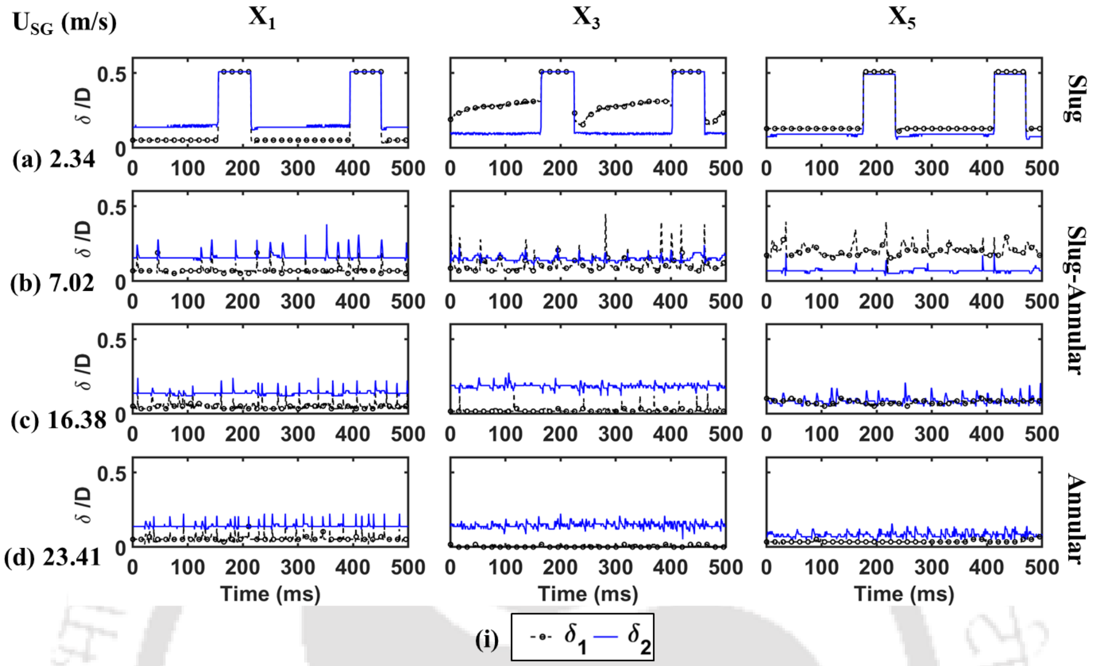

(i)

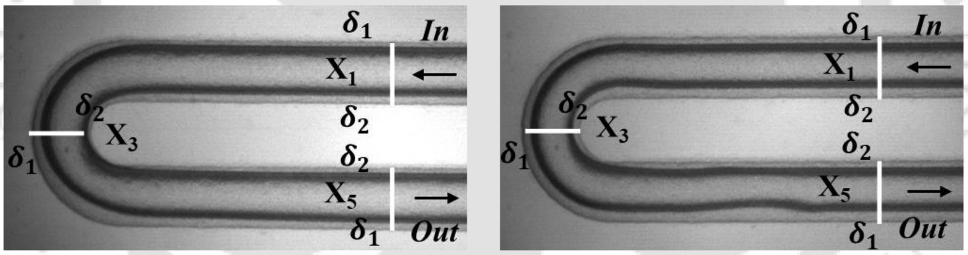

(a) Slug flow

(b) Slug-Annular flow

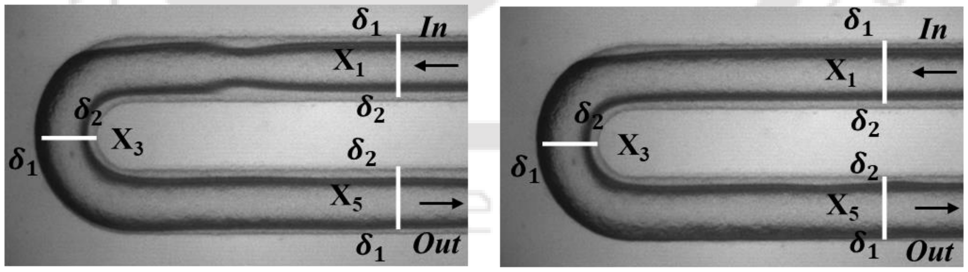

(c) Slug-Annular flow

(d) Annular flow

(ii)

Figure 2.8. The transition of flow regime from slug to annular showing (i) Time evolution plots at X_1, X_3, and X_5 locations. (ii) Instantaneous snapshot of corresponding flow regimes for (a) Slug flow (U_{SG} = 2.34 m/s, U_{SL} = 0.1 m/s), (b) Slug-Annular flow (U_{SG} = 7.02 m/s, U_{SL} = 0.02 m/s), (c) Slug-Annular flow (U_{SG} = 16.38 m/s, U_{SL} = 0.02 m/s), and (d) Annular flow (U_{SG} = 23.41 m/s, U_{SL} = 0.02 m/s).

2.3.3 Time Average Film Thickness

Time evolution plots of slug, slug-annular and annular flow regimes have shown that the curvature of the bend affects the film thickness significantly. Therefore, it is important to quantitatively investigate average film behavior at location X_3.

Slug Flow

In Figure 2.9(i), the time-averaged film thickness for four different liquids is plotted with Ca at location X_3. Note that Ca changes because of the change in fluid properties only, as the superficial velocities are the same for all the cases. The mean of inner and outer time-averaged film thicknesses ($\delta_{average}$) are also plotted for comparison. The film thickness was calculated using Eq. (2.3 proposed by Klaseboer et al. (2014)

$$\frac{\delta_F}{R} = \frac{1.34Ca^{2/3}}{1 + 3.74Ca^{2/3}} \tag{2.3}$$

Time-averaged δ_1 decreases with the increase in Ca. Whereas time-averaged δ_2 first increases and then decreases at higher Ca. Therefore, the average of δ_1 and δ_2 continuously decreases with an increase in Ca which is opposite to the trend observed by Eq. (2.3(2.3. Note that the expression in Eq. (2.3 is developed for a straight microchannel flow. It is possibly due to the fact that δ_1 and δ_2 are measured on a two-dimensional plane seen from the top of the channel although average film thickness behavior over the circular cross-section could result in an overall increase with Ca. Qualitative images shown in Figure 2.9(ii) represent the instantaneous film behavior at location X_3.

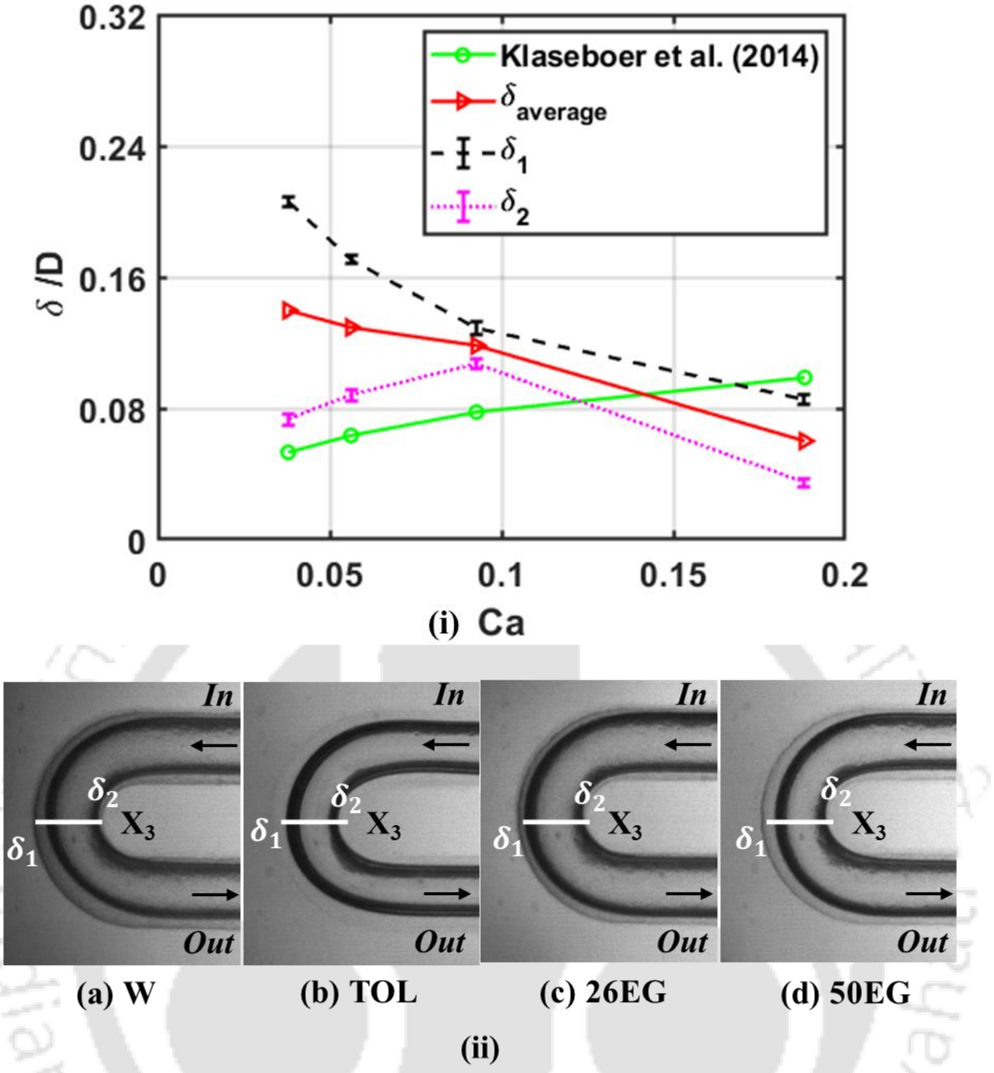

Figure 2.9. (i) Time average film thickness variation with Ca at location X_3 and (ii) Instantaneous images of the slug flow at X_3 for (a) W, (b) TOL, (c) 26EG, and (iv) 50EG.

While capillary number takes into account only viscous and surface tension effects, Suratman number includes inertial, surface tension and viscous forces. Since inertial forces are important in this work, the variation of film thickness with Su is also shown in Figure 2.10. δ_1 increases with an increase in Su. Unlike δ_1, variation of δ_2 is random. As a result, as Su increases, $\delta_{average}$ increases overall, with a slight decrease at Su = 75858.

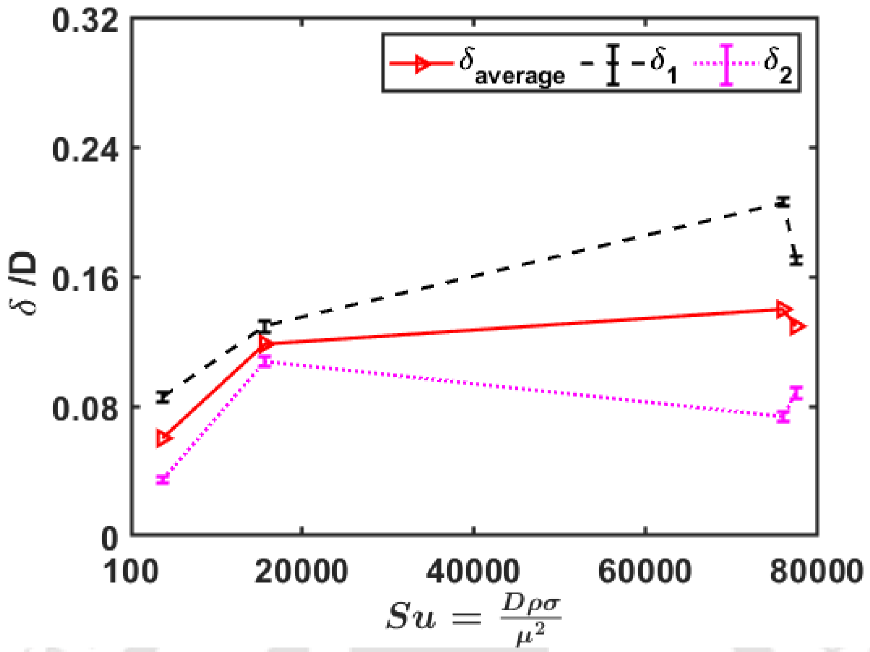

Figure 2.10. Time averaged film thickness variation with Suratman number (Su)

Annular Flow

An analytical solution relating pressure gradient (B) with U_{SL} and U_{SG} for core-annular flow in straight channel can be derived assuming the laminar, fully-developed flow and the smooth interface between the two phases (Guo et al., 2016; Gupta et al., 2016).

$$U_{SL} = -\frac{BR^2}{8\mu_L}\left(1-\frac{r_i^2}{R^2}\right)^2 \tag{2.4}$$

$$U_{SG} = -\frac{BR^2}{4\mu_G}\left[\left(\frac{\mu_G}{2\mu_L}-1\right)\left(\frac{r_i}{R}\right)^4 + \left(\frac{r_i}{R}\right)^2\right] \tag{2.5}$$

U_{SL}, and U_{SG} are liquid and gas superficial velocities. μ_G and μ_L are the viscosity of gas and liquid, respectively. B is the axial pressure gradient, and R is the radius of the channel. The distance of the interface from the center of the channel is r_i $(= R - \delta)$. Eq. (2.4 and (2.5 can be solved to calculate r_i for known gas and liquid properties, superficial velocities, and channel diameter.

Figure 2.11 shows the variation of time-averaged inner and outer film thickness with Ca at location X_3 for three gas superficial velocities; U_{SG} = 7.02 m/s, 16.38 m/s, and 23.41 m/s. The corresponding smooth interface analytical solution is also shown for comparison. Note that Ca changes because of the change in the liquid properties only.

In Figure 2.11(a), slug-annular flow at U_{SG} = 7.02 m/s shows no significant trend with an increase in Ca. High amplitude waves present at the interface in slug-annular flow may be the reason for trend. $\delta_{average}$ first increases with the increase in Ca and then decreases. As observed in the time evolution plot described in Section 3.2.3, the time-averaged outer film (δ_1) is always smaller than the inner film (δ_2) except at Ca = 0.47, which is the case of 50EG.

Figure 2.11(b,c), plotted for slug-annular and annular flow at U_{SG} = 16.38 m/s and 23.41 m/s respectively, show that time-averaged film thickness increases with Ca. δ_1 is always smaller than δ_2. Though δ_2 and $\delta_{average}$ show a substantial difference, δ_1 is observed to be closest to analytically calculated film thickness.

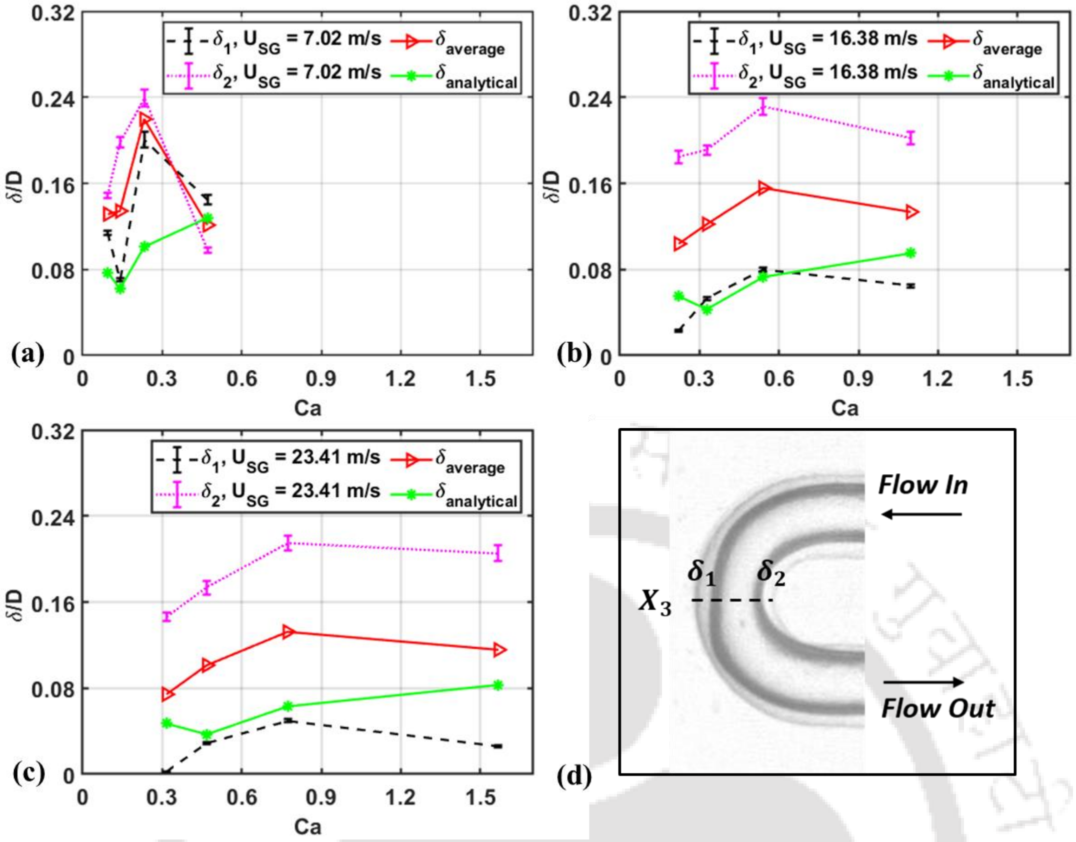

Figure 2.11. Time averaged film thickness variation with Ca at location X_3 at U_{SL} = 0.02 m/s, and (a) U_{SG} = 7.02 m/s, (b) U_{SG} = 16.38 m/s, and (c) U_{SG} = 23.41 m/s. (d) A typical image of the bend showing location and flow direction.

Slug to Annular Transition

The gas to liquid flow rate ratio is an important parameter in the regime transition as well as in determining the liquid film thickness. This ratio has been defined as slip ratio $\left(S = \frac{U_{SG}}{U_{SL}}\right)$ in the literature (Nino et al., 2002). In Figure 2.12, time-averaged inner and outer film thicknesses along with the $\delta_{average}$ for water-nitrogen flow are plotted as a function of slip ratio on a logarithmic scale as the secondary x-axis. Slug and annular flow regimes are differentiated by a random dotted line. It is observed that time-averaged δ_1 decreases continuously with an increase in slip ratio. In contrast, the effect on the δ_2 is ambiguous. As a result, $\delta_{average}$

remains nearly constant in slug and slug-annular regime but decreases continuously in annular flow regime as the slip ratio increases.

Gas to liquid centrifugal force ratio $\left(\frac{\rho_L U_{SL}^2}{\rho_G U_{SG}^2}\right)$ is plotted as the primary x-axis for the same. At the curvature, centrifugal force becomes an important parameter for a liquid film thickness. In the case of slug flow, this ratio is always greater than 1. However, the transition of flow regimes occurs when this ratio decreases well below the value 1.

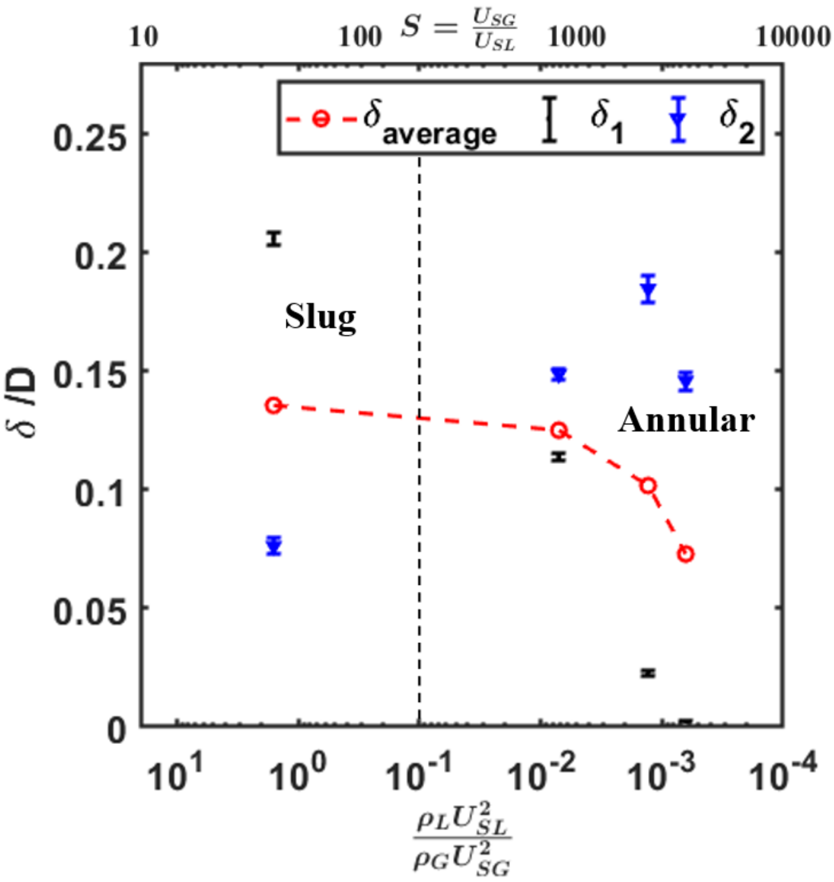

Figure 2.12. Time average film thickness variation with liquid to gas centrifugal force ratio at the bottom and slip ratio (S), which is gas to liquid flow rate ratio at the top for water-nitrogen flow. Note that dotted line separating the flow regimes is for denotion only and do not show any critical range.

Figure 2.13 (i) shows the consolidated film thickness behavior of water-nitrogen flow at various locations of curved sections for slug and annular flow regimes. The results shown are for slug flow at U_{SL}= 0.1 m/s, U_{SG} = 2.34 m/s, and for annular flow at U_{SL}= 0.02 m/s, U_{SG} = 23.41 m/s. An instantaneous snapshot of the flow pattern for each case is also shown in Figure 2.13(ii). However, it may be noted that the data shown on the graph are time-averaged, whereas the images are only for a time instant.

In the case of slug flow, the outer film (δ_1) is thinner than the inner film (δ_2) at the entrance of the U-bend (X_1 and X_2). The outer film (δ_1) becomes thicker at the middle of the bend (X_3). At downstream of the bend (X_4 and X_5), the outer film (δ_1) starts thinning again, and the two films are of almost equal thickness. Unlike outer film (δ_1), the inner film (δ_2) remains almost same at all locations. However, the inner film (δ_2) is observed to be thinner between locations X_3 and X_4, as can be seen in the image of slug flow (Figure 2.13(ii)).

In the case of annular flow, the outer film (δ_1) is thinner as it enters the bend (X_1) and becomes very thin at the bend (X_3). As the flow exits the bends, the outer film (δ_1) starts thickening again. As is the case for slug flow, the inner film (δ_2) is relatively of constant thickness at the bend.

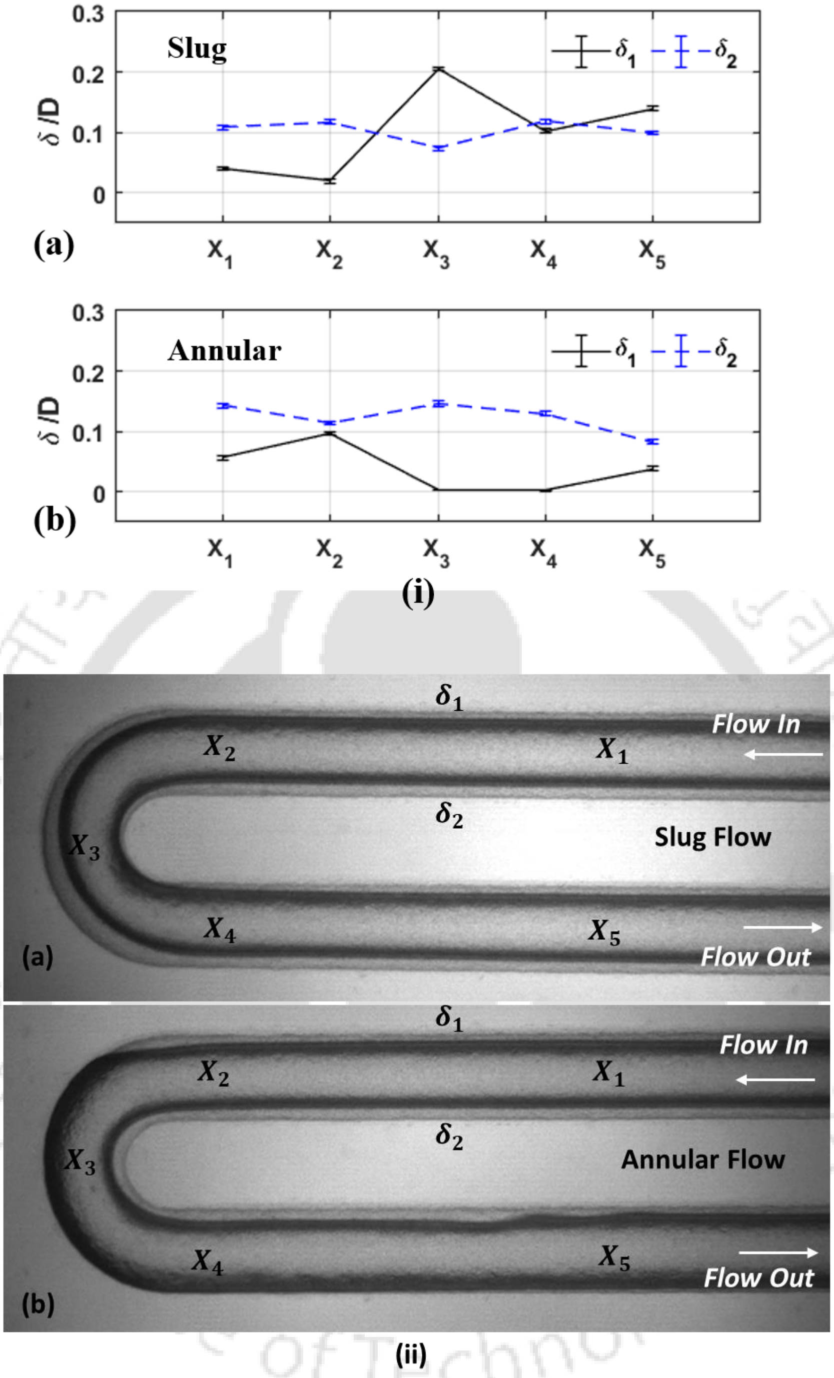

Figure 2.13. (i) Time-averaged outer (δ_1) and inner (δ_2) liquid film thickness variation of water-nitrogen flow at various locations (X_1, X_2, X_3, X_4, and X_5). (ii) Typical instantaneous images for slug and annular flow regimes. (a) Slug flow at U_{SL}= 0.1 m/s, U_{SG} = 2.34 m/s, and (b) Annular flow at U_{SL}= 0.02 m/s, U_{SG} = 23.41 m/s. Note that the bubble is very long in case of a slug flow regime, and either of the bubble ends are not visible in the image.

2.4 Summary

Liquid film thickness distribution in slug, slug-annular, and annular flow regimes in a 1 mm diameter circular glass microchannel having multiple U-bends was investigated using a high-speed camera. Images were captured and processed at the U-bend to quantify liquid film thickness for liquids having different viscosities with nitrogen as the gas phase. Spatial and temporal variation of film thicknesses was plotted for low to very high capillary numbers (Ca = 0.033-1.644) at different locations of the U-bend. The liquid film was observed to be distributed non-symmetrically in all the regimes. In general, the inner liquid film was of constant thickness throughout the bend except between the middle and exit of the bend. The outer liquid film varied considerably at the bend for a particular case. Inner film thickness was smaller than that of outer film in the slug flow regime. This showed that the bubble tends to move towards inner curvature of the bend in slug flow regime. However, in annular flow regime inner film thickness was larger than outer film, which showed that gas core moves towards outer curvature of the bend. This transition of film thickness behavior at the bend occurred in the slug-annular flow regime. The average liquid film thickness decreased with an increase in the slip ratio i.e., ratio of gas and liquid flow rates.

Chapter 3. Numerical Investigation of Gas-Liquid Flow in a Curved Microchannel

Experimental study of different gas-liquid flow regimes in curved microchannel showed that the circumferential distribution of liquid in the film present between gas bubble/core and the wall changes with the flow regime transition. Images of different flow regime in curved microchannel show the liquid film distribution but do not provide any detail of the resultant flow field in the gas and liquid phases. Therefore, to understand the flow physics of different gas-liquid flow regimes at the U-bend, three-dimensional numerical investigation has been done for one U-bend section of the same channel as used in the experiments. The hydrodynamics of the gas-liquid flow, liquid film thickness on the wall, and local velocity field in each phase play a major role in the design of the microsystems of a specific application. In this numerical study, we investigate gas-liquid flow in a lab-scale microreactor of a circular cross-section of 1 mm diameter U-bend used in the experiment discussed in chapter 2. The evolution of the liquid film on the wall, the deformation of the bubbles/gas core in the curved section, and its effect on local hydrodynamics and mixing are examined in the slug and annular flow regimes. Secondary flow or Dean vortices are observed in both phases at the U-bend across various Capillary numbers (Ca) (0.001-0.007) during the transition from slug to annular flow regime.

3.1 Introduction & Literature Review

The qualitative results from experimental observation of gas-liquid flow in a curved microchannel indicate the asymmetric distribution of liquid in the film at the curved section of the microchannel. During the transition from slug flow regime to annular flow regime, the thin inner liquid film in slug flow becomes thicker in annular flow. It is suggested that the ratio of centrifugal forces on gas and liquid phases can be governing factor for this transition in liquid film thickness. Local velocity field inside both phases at the curved region can provide further understanding of the flow. Liquid film thickness is symmetric, surrounding the gas core in a straight microchannel, but a sudden change in flow path disturbs the film thickness distribution. Numerical investigation of the motion of a large bubble in curved channels showed that the inner liquid film is thinner than the outer liquid film for small *Ca* (Muradoglu and Stone, 2007). Further, studies theoretically suggested that smaller curvatures do not affect the velocity profile much, but larger curvatures may affect the flow field inside, and liquid film may get displaced toward the inner wall (Picardo and Pushpavanam, 2013b).

Centrifugal force developed due to curvature plays an important role in flow regime development at the bend and can affect annular flow severely, breaking it into small slugs (Wu and Sundén, 2019). 2D axisymmetric CFD modeling of these flow regimes is in abundance for straight microchannels because of the symmetric nature of the problem (Asadolahi et al., 2011; Gupta et al., 2010; Klaseboer et al., 2014; Kumari et al., 2019). However, the problem of two-phase flow at the bend is three-dimensional in nature, and resolving the interface using refined grid size becomes numerically expensive (Kositanont et al., 2014; Magnini et al., 2022).

The literature review indicates the limited knowledge of flow regime behavior at the bend and the requirement of three-dimensional CFD investigation for a better understanding. Therefore, in this study, we investigate slug-to-annular flow regime transition at different flow velocities. The behavior of liquid film at a U-bend is investigated in the case of a slug to annular flow transition at low to moderate Capillary number (*Ca*) using 3D CFD modeling. The gas-liquid system chosen for this study is nitrogen and water. This study focuses on the secondary flow, velocity field in both phases, and liquid film thickness behavior at the bend.

3.2 Computational Methodology

This study involves CFD modeling of gas-liquid flow inside the U-bend with a circular cross-section of diameter 1 mm. Table 3.1 shows the physical properties of water and nitrogen gas used for the study.

Table 3.1 Physical properties of nitrogen gas and water used in the simulations

Fluids	**Density (ρ) (Kg/m^3)**	**Viscosity (μ) (Pa·s)**	**Surface Tension (σ) (N/m)**
Water	998	0.00098	0.073
Nitrogen	1.145	0.00002	-

3.2.1 CFD Methodology

To understand flow behavior near the U-bend, a 10 mm long upstream and downstream straight section along with the U-bend is chosen for numerical investigation. Figure 3.1a shows that the computational domain consists of two 10 mm long straight channels connected with a U-bend. The cross-section of the channel is circular having 1 mm diameter. Geometry is three-dimensional, and the figure shows a 2D view (*xy* plane passing through $z = 0$) of the channel. An upstream and downstream length of 10D along with the semicircular curved channel of 1D curvature is selected as the computational domain. Gas and liquid enter the computational domain in annular manner, gas in the core and liquid on the wall and flow regimes develops along the flow direction. A development length is required to achieve a specific flow regime (slug, slug-annular, and annular).

The volume of fluid method (VOF) is used to capture the interface. In this method, a 'single-fluid formalism' is used in which only a single set of conservation equations are solved together with an advection equation for a marker function (Hirt and Nichols, 1981). The marker function has a value of '0' for one phase and '1' for the other, and values between 0 and 1 are the interface region. For the VOF method, the volume fraction of one of the phases is the marker function. The flow is incompressible and laminar, with constant fluid properties such as density, viscosity, and surface tension. The conservation equations for the VOF method can be written as Eq. 3.1 and (3.2):

Conservation of mass:

$$\frac{\partial \rho}{\partial t} + \nabla.(\rho \mathbf{v}) = 0 \qquad 3.1$$

Conservation of Momentum:

$$\frac{\partial \rho \mathbf{v}}{\partial t} + \nabla.(\rho \mathbf{v}\mathbf{v}) = -\nabla P + \nabla.(\mu \nabla \mathbf{v}) + \mathbf{F}_{SV} \qquad (3.2)$$

An additional equation for the advection of the marker function (α) is solved to track the phases. The marker function (α) is the volume fraction of one of the phases as given by Eq. (3.3)(α).

$$\frac{\partial \alpha}{\partial t} + \mathbf{v}.\nabla \alpha = 0 \qquad (3.3)$$

The equations (3.1, (3.2), and (3.3)) represent the conservation equations in phase 1 when α = 1 and in phase 2 when α = 0. For the interface cells in which $0 < \alpha < 1$, the volume fraction-weighted average of the properties of the two fluids is used in the conservation equations.

$$\varphi = \varphi_1 \alpha + (1 - \alpha)\varphi_2 \qquad (3.4)$$

Where φ represents the bulk properties of the fluid, such as density, and viscosity. The jump in the stresses normal to the interface is modeled using the continuum surface model (CSF) which approximates the surface force as a body force in the vicinity of the interface using the Dirac function ($\delta(\boldsymbol{r}-\boldsymbol{r}_{int})$) as given by Eq. (3.5) (Brackbill et al., 1992).

$$\mathbf{F}_{\mathrm{SV}} = \kappa\sigma\delta(\mathbf{r}-\mathbf{r}_{\mathrm{int}})\hat{\mathbf{n}} \tag{3.5}$$

The Dirac delta function is zero everywhere except at the interface, i.e., $\boldsymbol{r} = \boldsymbol{r}_{int}$ where $\boldsymbol{r}$ is the position vector. The surface curvature κ, is calculated from the surface normal at the interface ($\kappa = \nabla.\hat{\boldsymbol{n}}$). The surface normal is obtained from the gradient of the volume fraction $\left(\hat{\boldsymbol{n}} = \frac{\nabla\alpha}{|\nabla\alpha|}\right)$.

Constant gas and liquid velocities are used at the inlet, and a constant pressure (gauge pressure of 0 Pa) is specified at the outlet. A no-slip boundary condition is used on the channel wall. A structured mesh is used throughout the geometry.

3.2.2 Mesh and Numerical Schemes

The mesh is refined sufficiently near the wall so that the film near the wall can be captured accurately. Researchers have investigated the appropriate refinement for this purpose in the past (Gupta et al., 2009; Khadiya et al., 2021). Figure 3.1b show the meshing at the inlet which is swept along the flow direction. Figure 3.1c and Figure 3.1d show the near wall mesh at the location marked with red rectangles on Figure 3.1a which is refined enough to capture the interface.

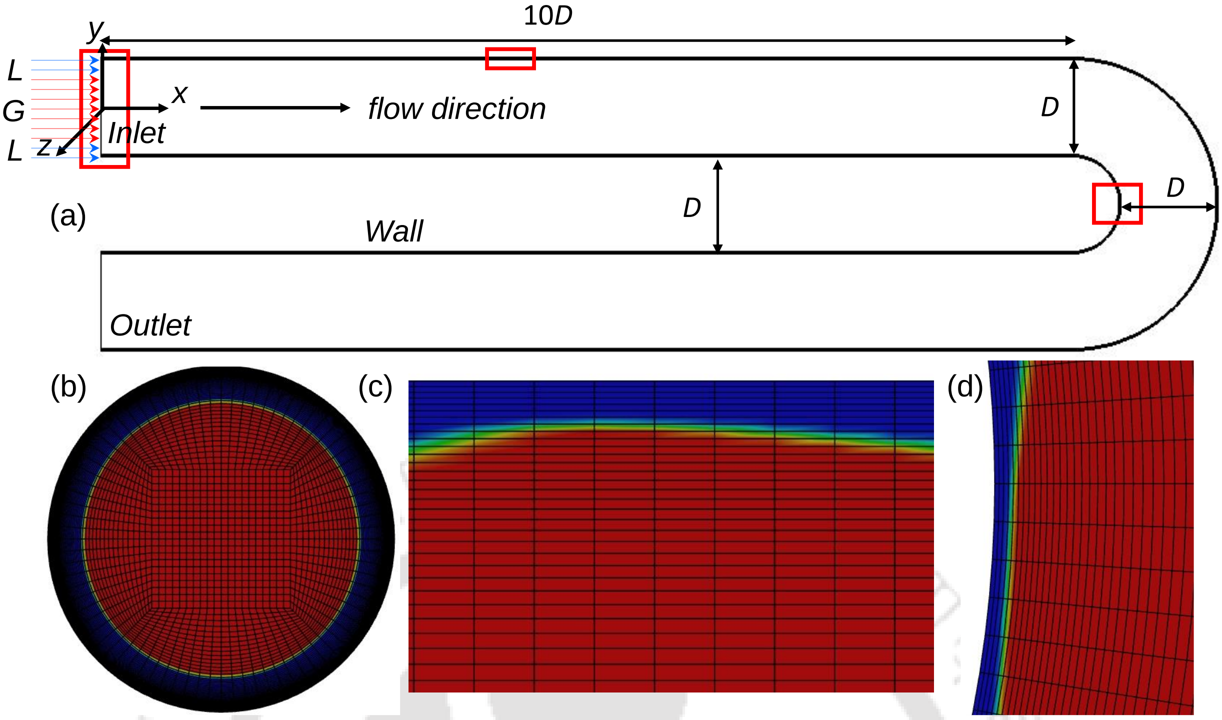

Figure 3.1 (a) Schematic diagram of the U-bend geometry with flow direction and dimensions shown on a *xy* plane passing through the middle cross-section (z =0). Structured meshing with the near-wall refinement at (b) Inlet cross-section (*yz* plane), (c) Straight section (xy plane), and (d) U-bend to capture the interface. Regions marked with red color rectangles show the locations.

The governing equations are solved using the commercial CFD software ANSYS Fluent 19.2, which is based on the finite volume approach. The SIMPLE (semi-implicit pressure linked equations) scheme is applied for pressure–velocity coupling. The pressure at the face between neighboring cells is interpolated using the PRESTO! scheme, and the momentum equation is discretized using a second-order upwind method. An implicit scheme of the first order is employed for the discretization of the unsteady term. The time step size of 10^{-5} s is chosen for transient simulations. The absolute convergence criterion is set to 10^{-4} for all the equations.

3.2.3 Mesh Independency Study

A mesh independency test has been performed at two locations marked on the images with white lines shown in Figure 3.2a and Figure 3.2b. The profile of velocity magnitude are obtained using different meshes are shown in Figure 3.2a and Figure 3.2b. As suggested by previous researchers (Gupta et al., 2009) 5 to 8 mesh elements are used to capture the interface. The smallest number of mesh elements used in this study to capture interfaces at both regions (straight and curved) is 2.64×10^6. Further refinement is done by increasing the number of elements in diameter direction, which resulted in four meshes: 2.64×10^6, $3.08\ \times10^6$, 3.96×10^6, 4.4×10^6. The velocity profile for all the meshes at the curved section is shown in Figure 3.2a, while for the straight section is shown in Figure 3.2b. All the meshes are able to capture the interface. The comparison of velocity profiles show that the results are independent of the mesh used for the mesh having elements 3.96 million. Therefore, the mesh with 3.96 million or more element have been used for the further study.

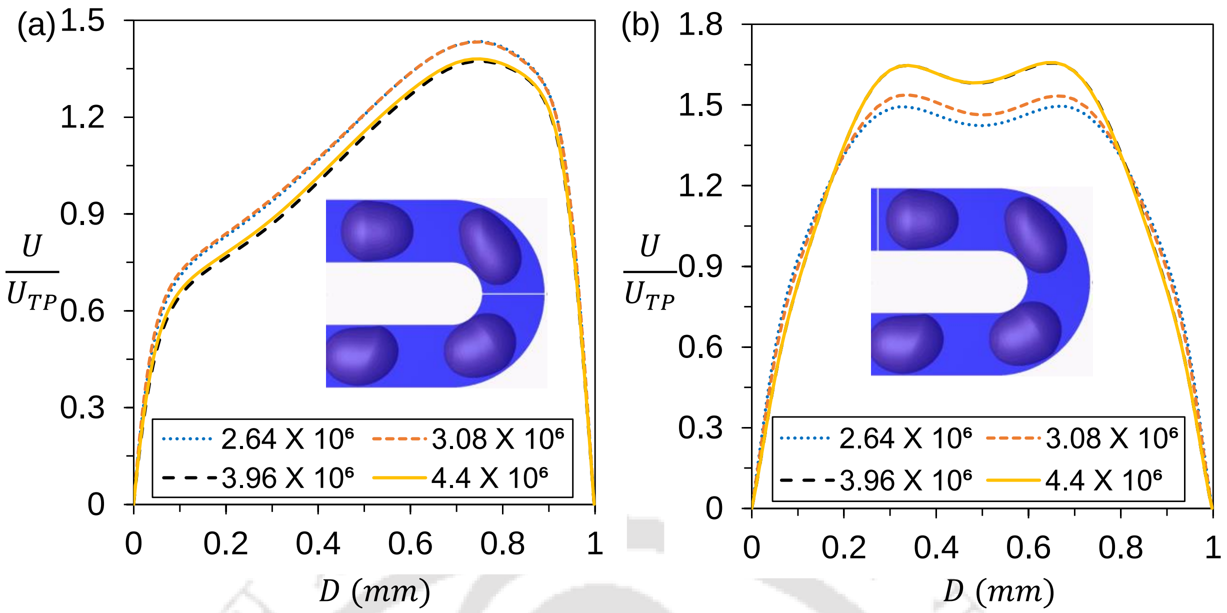

Figure 3.2 Mesh independence study performed at two locations (a) Velocity profile on a line passing through the midpoint of U-bend (shown by a white line), (b) Velocity profile on a line before the start of the U-bend (shown by a white line)

3.3 Results

3.3.1 Flow Regimes

Transient simulations are done for gas-liquid flow in the specified geometry for different superficial gas velocities (U_{SG} = 0.15 m/s, 0.23, 0.31, 0.46, and 0.62 m/s) keeping liquid superficial velocity constant (U_{SL} = 0.21 m/s). Figure 3.3 shows the volume fraction on a plane passing through the middle of the cross-section of the channel at three different time instants, *t* = 66 ms, 67 ms, and 68 ms. Gas enters as a central core at the inlet, and liquid jet surrounding the gas core. Different flow regimes are formed based on the corresponding phase velocities, as shown in Figure 3.3. A periodic slug or Taylor flow forms for U_{SG} = 0.15 m/s. Bubbles pinch off from the gas core at a length of ~4.8D from the inlet. The images at three time instants show the process of bubble separation from the gas core. A neck is formed before bubble pinch off. Increasing gas velocity at the constant liquid velocity results in longer bubble break off length.

For gas superficial velocity of U_{SG} = 0.23 m/s, bubble separation occurs at the bend. The size of the bubble increased with the increase in U_{SG}. The bubble shape is symmetric in the straight section. However, the outer film thickens, and the bubble moves towards the inner wall while passing through the curved section.

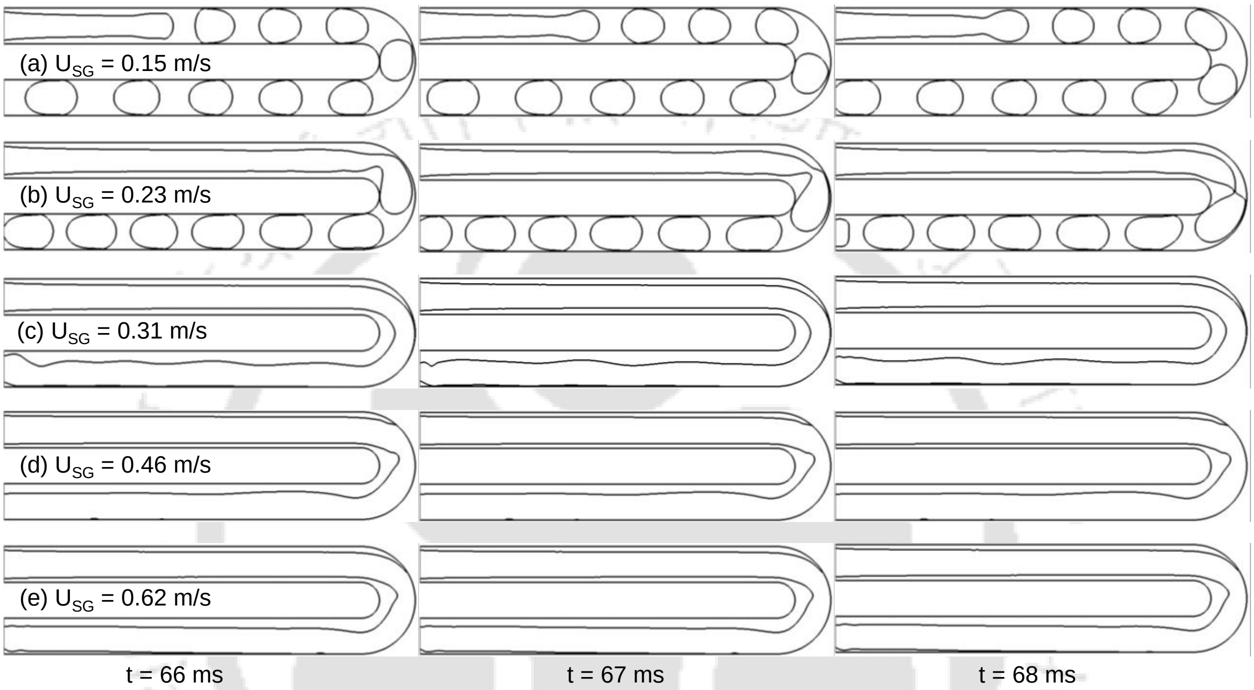

Figure 3.3 Shape and size of gas-liquid phases at a plane passing through the middle of the cross-section for slug, slug-annular, and annular flow at U_{SL} = 0.21 m/s and (a) U_{SG} = 0.15 m/s, (b) U_{SG} = 0.23 m/s, (c) U_{SG} = 0.31 m/s, (d) U_{SG} = 0.46 m/s, (e) U_{SG} = 0.62 m/s. Flow enters from the upper section and exits from lower.

Similar behavior was observed in the experimental investigations shown in chapter 2. Further increase in gas velocity results in the annular flow regime. Figure 3.3c, Figure 3.3d, and Figure 3.3e show the annular flow with different inner and outer liquid film thicknesses at U_{SG} = 0.31, 0.46, and 0.62 m/s. A major film thickness behavior change is observed in upstream and downstream straight sections of the channel. Inner and outer liquid film thickness is symmetric in the upstream section while asymmetric in downstream section. A complete dry-out is observed for the outer liquid film in the case of U_{SG} = 0.62 m/s. Note that the numerical dry-out depends on the near wall mesh size at the outer wall (less than 1 µm in this study).

3.3.2 Bubble Generation and Time Evolution

Since the method of bubble generation can affect its shape and size, it is important to understand the hydrodynamics of bubble formation before it reaches the U-bend. Figure 3.4 shows the snapshot of bubble formation at different time instants with a gap of Δt = 20 µs. It shows an isosurface of gas volume fraction α = 0.5. Gas and liquid enter the geometry from the inlet and gas blob (gas core/bubble before detachment) develops (marked in red rectangle) at the front tip of the gas core. The gas blob size increases with time and distance as the two phases move forward. After reaching nearly 4.8 mm from the inlet, this gas blob separates from the gas core, and form a bubble. The shape of the bubble changes over the next few microseconds, adjusting its front and tail while moving forward. Similarly, the tip of the gas core, which remains behind, starts to develop the next blob and starts increasing in size.

The time snapshot of the bubble generation shown in Figure 3.4 also depicts the change in bubble shape while passing through the U-bend. It is observed that after a bubble is generated and forms a bullet shape, it is symmetric in nature. In this case, the liquid film thickness is the same at all the locations from the wall. The shape starts to deform as soon as the bubble reaches the U-bend (9.0 mm from the inlet). The centrifugal force $\left(\frac{\rho U^2}{R_{curvature}}\right)$ at the U-bend induces a buoyancy force in the gas-liquid system. This causes the deformation in the shape of the bubble. The shape of the bubble continues to change while passing through the U-bend. Based on the flow velocity, it travels a sufficient length to regain its shape after passing through the U-bend.

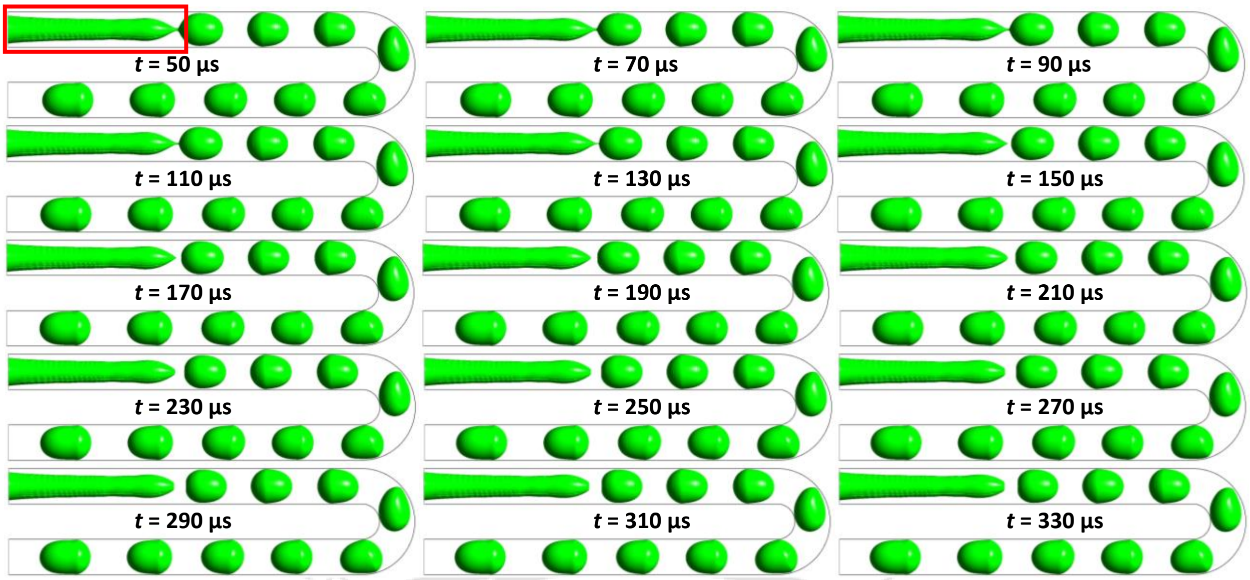

Figure 3.4 Bubble splitting and shape behavior at the U-bend at different time instants for $U_{SL} = 0.21$ m/s and $U_{SG} = 0.15$ m/s.

Based on the large variations in velocity profile inside the bubble at different time instants, it is important to understand the average behavior of bubble velocity at the bend. Volumetric average bubble velocity with time at different locations is shown in Figure 3.5. Volumetric average bubble velocity is calculated using equation Eq. $(3.6).(a)$

$$U_B = \frac{\int V_{mag} \alpha dV}{\int \alpha dV} \tag{3.6}$$

Bubble velocity increases (position 2) due to momentum gain after pinch off from gas core and achieves a steady constant velocity afterwards (position 3). Velocity increases a little before a small decrease as it approaches the bend (position 4 and 5). Because of the curvature, a sudden jump in velocity observed till position 6 before it starts to decrease until it reaches to position 8. Similar to upper half of the U-bend, a jump in bubble velocity is observed from position 9 to 10. The bubble velocity goes through a fall and rise before it reaches again to a steady velocity near position 14. Bubble travels ~2 mm to gain the steady velocity again after passing through the bend (from position 10).

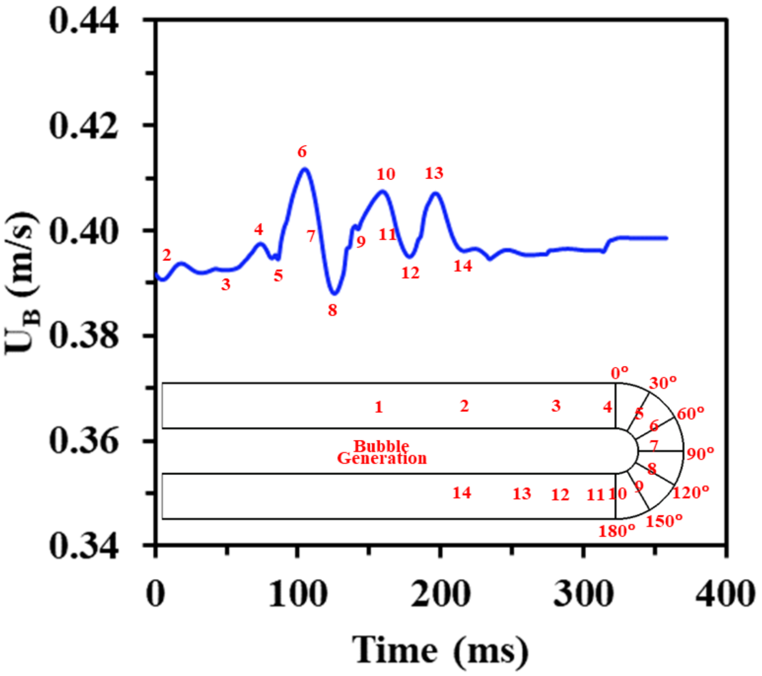

Figure 3.5 Bubble velocity behavior with time after generation. Bubble generated at U_{SG} = 0.2 m/s, and U_{SL} = 0.2 m/s

3.3.3 Secondary Flow

The curvature also induces a secondary flow in the cross-section plane. In a two-phase flow, the development and the evolution of secondary vortices can be more complex. Figure 3.6 shows the velocity magnitude projection on the x-z plane and viewing from the (-y)-axis passing through the mid-point of the U-bend. The inner circle shows the boundary of the gas phase. Figure 3.6a-e are plotted at constant liquid superficial velocity of U_{SL} = 0.21 m/s, while gas superficial velocity is varied from (a) U_{SG} = 0.15 m/s, (b) U_{SG} = 0.23, (c) U_{SG} = 0.31, (d) U_{SG} = 0.46, (e) U_{SG} = 0.62 m/s. Figure 3.6i-iii shows these flow fields at three time instants (64.0 ms, 66.0 ms, and 68.0 ms). The smallest gas superficial velocity U_{SG} = 0.15 m/s results in Taylor flow. Velocity magnitude is shown by color coding and the length of the arrow of the projected vectors on the plane. A smaller length vector represents that flow is towards normal to the plane, and a larger length vector represents that flow is towards tangential to the plane. Liquid flows away from the bubble towards the outer wall and then goes to the vicinity of the inner wall to bubble (see Figure 3.6a i-ii). The liquid-induced recirculation inside the bubble can be seen in Figure 3.6a i-ii. After the bubble passes, the Dean vortices appear inside the liquid phase throughout the cross-section (see Figure 3.6a iii). At U_{SG} = 0.23 m/s, two Dean vortices inside the bubble appear (Figure 3.6b i-ii) which is of greater strength than those observed at U_{SG} = 0.15 m/s. Figure 3.6b iii shows two smaller strength liquid recirculations towards the inner wall while the tail of the bubble appears at the outer wall. Further increase in gas superficial velocity to U_{SG} = 0.31 m/s, 0.46 m/s, and 0.62 m/s results in the slug-annular transition to annular flow. During this transition, the interface changes from convex to concave towards the inner wall.

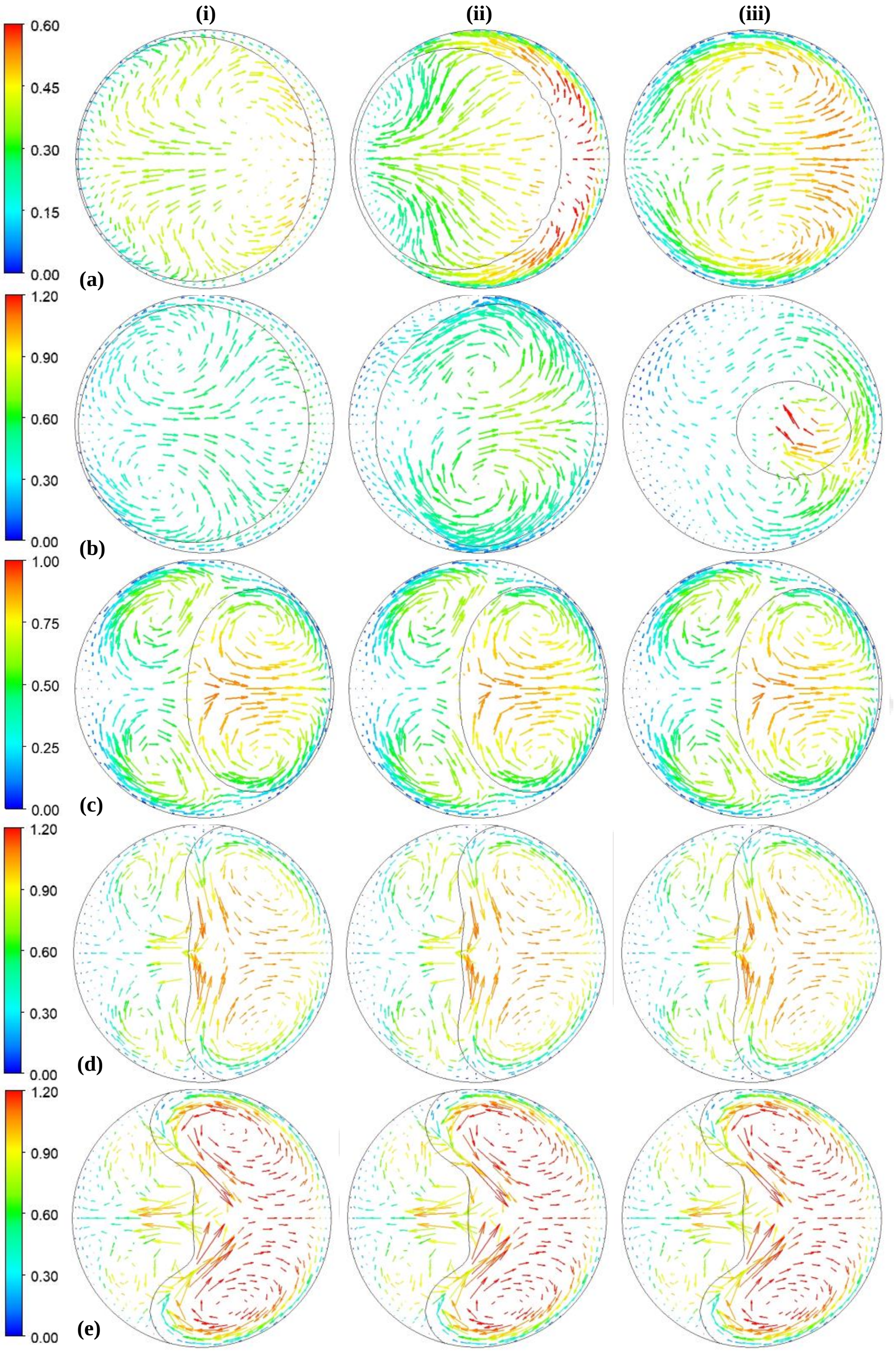

Figure 3.6 Secondary flow at the mid-point cross-section plane of the U-bend for (a) U_{SG} = 0.15 m/s, (b) U_{SG} = 0.23, (c) U_{SG} = 0.31, (d) U_{SG} = 0.46, (e) U_{SG} = 0.62, and at U_{SL} = 0.21 m/s, section i, ii, and iii are at different time interval Δt = 1 ms.

The change in the shape of the interface at the mid of the U-bend as shown in Figure 3.6 is explained by comparing centrifugal forces in the gas and liquid phases. Figure 3.7 shows the variation of the ratio of liquid to gas centrifugal forces with superficial gas velocity at a constant liquid superficial velocity (U_{SL} = 0.21 m/s). It is observed that while U_{SG} increases from 0.15 – 0.62 m/s, the corresponding ratio of centrifugal forces exhibits a proportionally greater increase, amplifying by approximately one order of magnitude, from 0.0006 to 0.0096 (16 time).

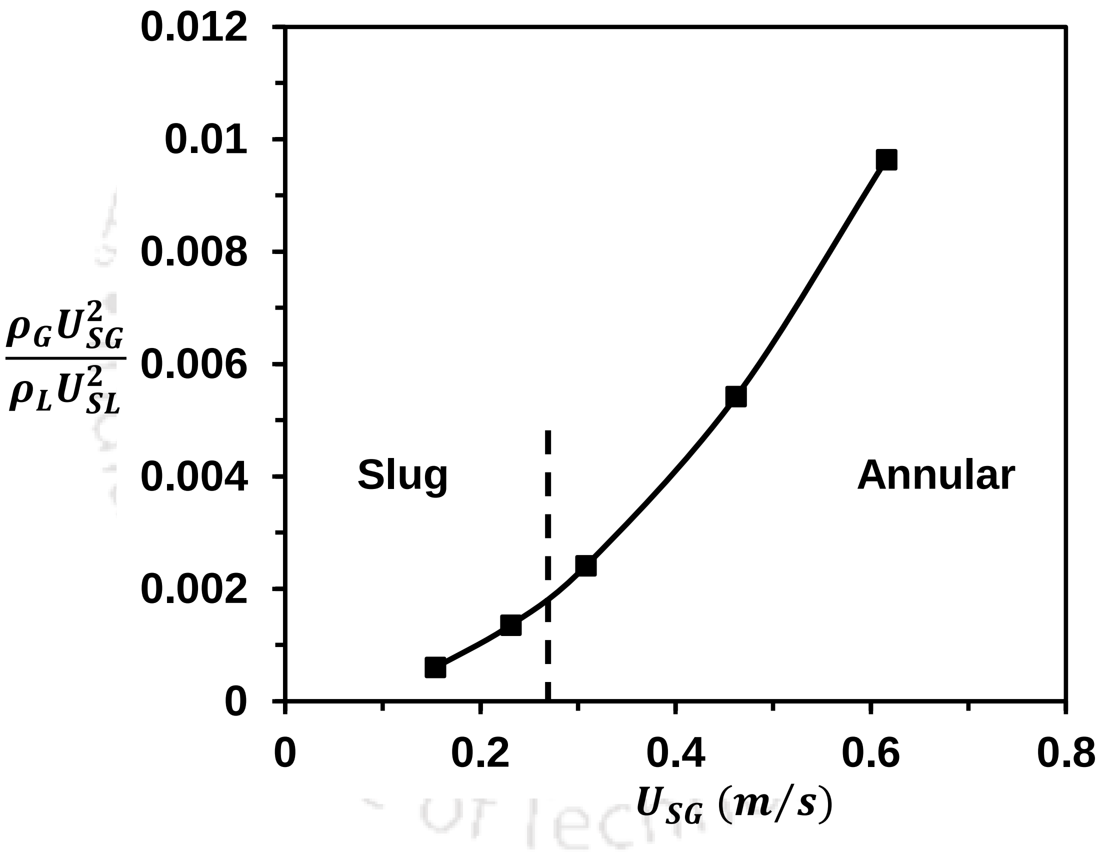

Figure 3.7 Behavior of centrifugal forces of liquid to gas ratio with superficial gas velocity (U_{SG})

3.3.4 Liquid film Thickness

A thin liquid film is observed at U_{SG} = 0.31 m/s (Figure 3.6c), which disappears (Figure 3.6d and e) with a further increase in gas velocity. Counter-rotating Dean vortices appear in both phases in all these cases (Figure 3.6c-e). The velocity magnitude inside the gas phase increases with an increase in U_{SG}. Figure 3.8 shows the variation in inner and outer liquid film thickness with capillary number (*Ca*). It show that the inner liquid film is thinner than the outer liquid film in the case of the slug flow regime and vice versa in the case of the annular flow regime.

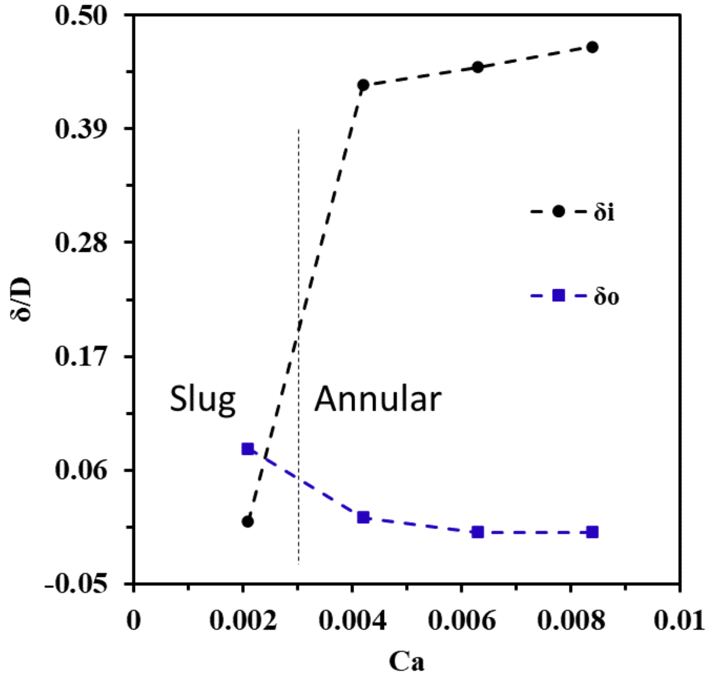

Figure 3.8 Film thickness behavior with Capillary number (*Ca*) based on gas superficial velocity for slug, slug-annular, and annular flow.

3.3.5 Velocity Profiles

Figure 3.9a shows the profile of velocity magnitude of different flow regimes in a straight section at 8.0 mm away from the inlet plotted on a line on *xy* plane across channel cross-section passing through $z = 0$ at constant $U_{SL} = 0.21$ m/s. This location (8.0 mm) is selected in such a way that it could describe the flow behavior of the bubble just before entering into the U-bend. Velocity increases along the radial direction and achieves a maximum velocity for $U_{SG} = 0.31$

m/s, 0.46 m/s, and 0.62 m/s. However, cross-sectional velocity, first increases and then decreases for U_{SG} = 0.15 m/s along the radial direction. Velocity profiles are symmetric around the center point of the circular cross-section of the channel. There is a sudden increase and decrease in the velocity profile for U_{SG} = 0.15 m/s case at the inner and outer wall interfaces, which indicates the presence of a large velocity gradient.

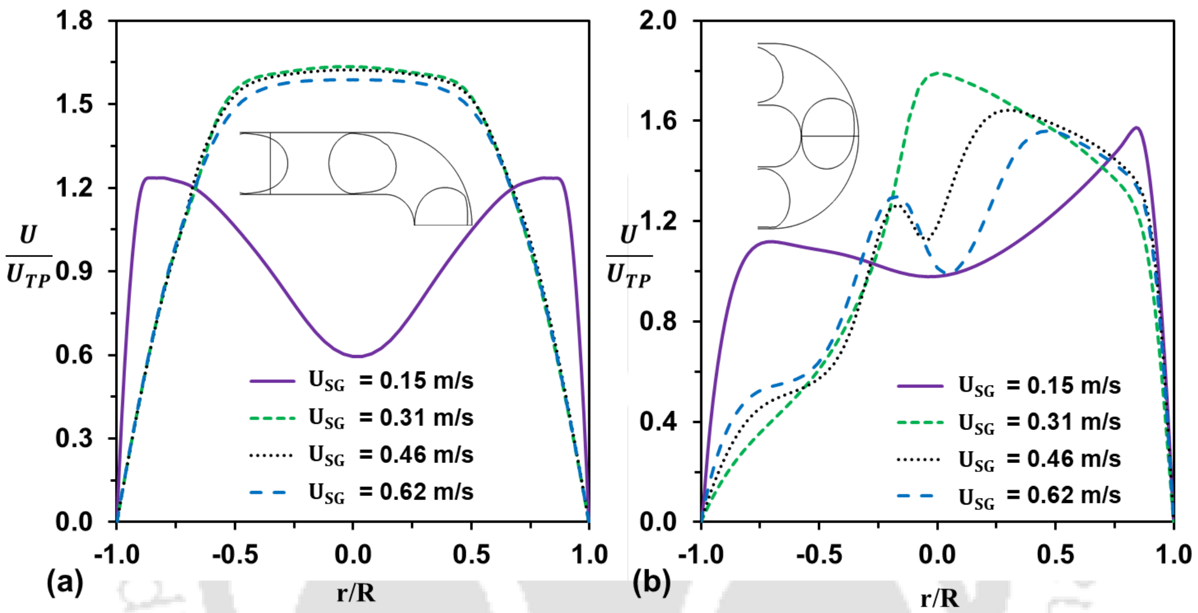

Figure 3.9 (a) Velocity profiles in a straight section at 8.0 mm away from the inlet plotted on a line on *xy* plane passing through *z* = 0 at constant U_{SL} = 0.15 m/s. (b) Velocity profiles plotted on a line on *xy* plane passing through the mid-point of the channel cross-section of the U-bend at Y = -1.0 mm at constant U_{SL} = 0.15 m/s.

Figure 3.9b shows the velocity magnitude profile on a line on the *xy* plane passing through *z* = 0 across the channel cross-section at the mid of the U-bend (y = -1.0 mm) at constant U_{SL} = 0.21 m/s. Similar to the straight section, the trend of the slug flow (U_{SG} = 0.15 m/s) velocity profile is different from annular flows. In slug flow, velocity increases near the wall and decreases at the center of the channel. However, at U_{SG} = 0.31 m/s, velocity continues to increase in the center until it reaches a maximum point and then decreases as we move towards the outer wall. Note that, unlike the straight section, the velocity profile is not symmetric around a center point. For U_{SG} = 0.46 m/s and 0.62 m/s, the velocity magnitude decreases and increases twice in the center region along the diameter. The possible reason for this behavior can be attributed to the curvature effect of the U-bend.

Based on the analysis of Figure 3.9, it is important to understand the behavior of cross-section velocity magnitude with time for slug flow (U_{SG} = 0.15 m/s) at the same location of the line. Figure 3.10a shows the time snapshot of the bubbles on the *xy* plane passing through z = 0. Figure 3.10b shows the corresponding velocity profiles on different time instants on the line shown in Figure 3.10a. At time t = 64.0 ms, the bubble just passed the line, and only the liquid slug is present; the corresponding velocity profile shows that as velocity increases along the radial direction from the wall, a small decrease occurs at the center region. The profile is not symmetric across the center point. This asymmetry is observed because of the presence of the bubble. As the time increases, the bubble moves further away from the line, asymmetry starts to disappear, and the profile becomes symmetric around 65.0 ms. The dip in the velocity at the center region increased and started to decrease again as the next bubble approached the line (see the images on 64.0 and 65.0 ms). At 66.0 ms, the front of the bubble crosses the line, which corresponds to the lowest velocity in the center region, and with an increase in time, the bubble passes, and the center point velocity starts to increase again (see velocity profile at 67.0 ms and 68.0 ms). The velocity profiles shown in Figure 3.9 are plotted at a time of 66.0 ms, where the slug flow profile behaves very differently because of the front of the bubble passing through the line. However, with the advent of time, the velocity profile in the center region flattens and approaches annular flow, as can be seen in Figure 3.10.

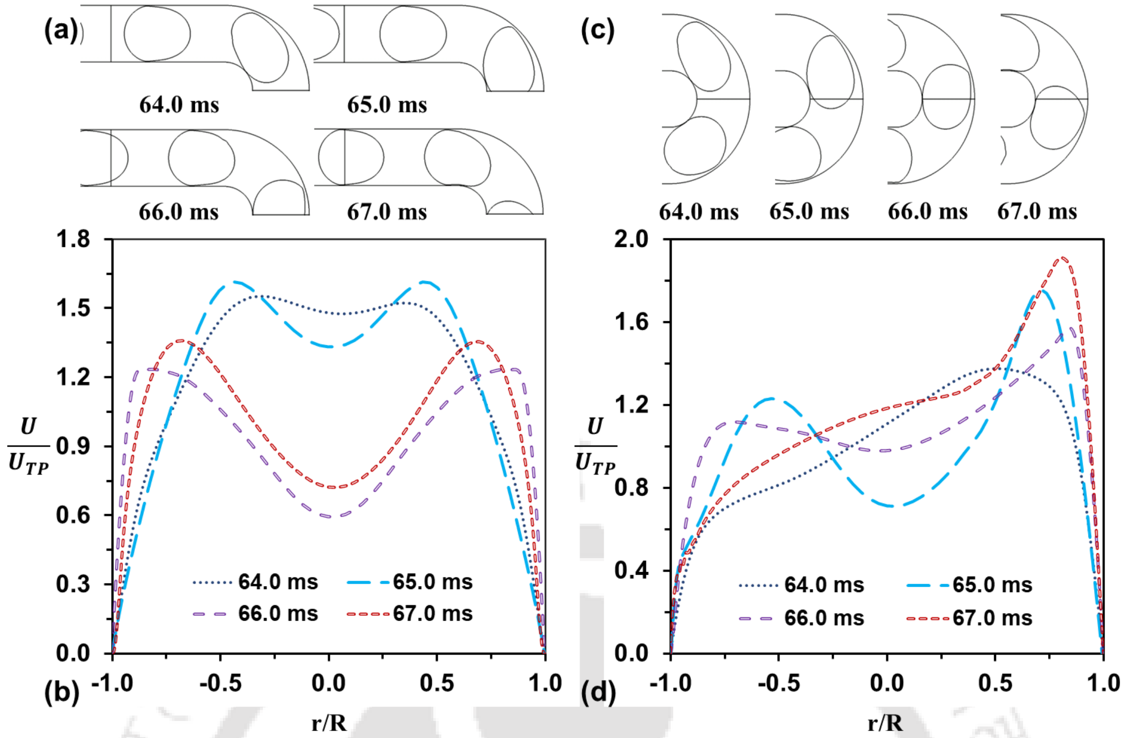

Figure 3.10 (a)Time snapshot of the bubbles on *xy* plane passing through *z* = 0 near the line across channel cross-section created at 8.0 mm away from the inlet before entering to U-bend along with velocity profiles on the line at different time instants for slug flow regime at U_{SG} = 0.15 m/s, and U_{SL} = 0.15 m/s and (b) Corresponding velocity profiles on the line at different time instants for slug flow regime at U_{SG} = 0.15 m/s, and U_{SL} = 0.15 m/s (c) Time snapshot of the bubbles on *xy* plane passing through *z* = 0 near the line across channel cross-section at the midpoint of the U-bend (d) Corresponding velocity profiles on the line at different time instants for slug flow regime at U_{SG} = 0.15 m/s, and U_{SL} = 0.15 m/s

Figure 3.10c and Figure 3.10d shows the bubble image at the U-bend at different time instants, along with the corresponding velocity profile plotted on the line, for slug flow at U_{SG} = 0.15 m/s and U_{SL} = 0.15 m/s. Similar to the straight section velocity profile, it is observed that as the bubble front falls on the line, a sudden change in velocity profile appears, as shown in the zoomed view of the bubble at 64.0, and 65.0 ms time snapshots. It is observed that this behavior only appears at the inner wall liquid film thickness, which is thinner than the outer wall (see images at 64.0, and 65.0 ms). At 66.0 ms, the sudden change in velocity profile near the inner wall disappears and does not appear for all other cases. The change in velocity profile at the center region occurs due to the Dean flow or secondary flow because of the curvature effect.

An analytical solution is derived from Navier Stokes equation assuming a two-dimensional, steady state, incompressible newtonian flow in cylindrical coordinate. The full derivation for the analytical solution is given in Appendix A. However, the analytical solution provides information about the asymmetric behavior of the velocity profiles it could not be used for the quantitative comparison with CFD results.

3.4 Summary

Gas-liquid two-phase flow in a circular cross-section U-bend microchannel of 1 mm diameter was investigated numerically for a nitrogen-water gas-liquid system. Bubble generation and shape change while passing through the bend were studied at different time instants. The liquid film thickness was measured for different sizes of the gas bubbles/core, and the internal velocity field inside the gas and liquid phases was analyzed. Dean vortices were observed in both the phases at U-bend at different *Ca* during the transition from slug to annular flow regime. Different velocity profiles on a line passing through the cross-section before and at the bend were investigated. The average bubble velocity was measured during Taylor flow. The bubble velocity magnitude increased during the upper half of the bend and decreased during the lower half of the bend. This study confirms the enhanced mixing in both phases because of the bend.

Part B:

Droplet inside liquid media in a rectangular confined channel

Chapter 4. Velocity Field Within Droplets Falling in Liquid Media Inside a Rectangular Channel

4.1 Introduction & Literature Review

The motion of a droplet moving in a continuous liquid is important to understand due to its application in emulsion formation, liquid-liquid extraction, and oil-water flow in pores of an underground reservoir (Deng et al., 2014). The concept of a droplet acting as a reactor, commonly known as a *droplet microreactor*, has been introduced in microfluidics (Pan et al., 2018; Saucedo-Espinosa et al., 2023; Zhang et al., 2023) in which a train of droplets move in a continuous liquid stream. In such a case, mixing inside the droplets is important, for example, to accurately determine the reaction rate. Liquid-liquid contacting is required to transfer a solute from one phase to another for the reaction or extraction process (Assmann et al., 2013; Mehrabian et al., 2018; Widianto et al., 2020). The knowledge of droplet dynamics in liquid-liquid contactors is essential to increase the transfer efficiency. Understanding droplet behavior in a confined environment is crucial for designing various micromixing devices. Design developments in soft robotics, quake valves, lab-on-a-chip, microelectronics, and organ-on-a-chip require knowledge of droplet dynamics in a confined environment (Aminizadeh and Moosavi, 2023; Bezuidenhout et al., 2020; Günther et al., 2004; Mazzolai and Mattoli, 2016; Shen et al., 2010; Unger et al., 2013).

The motion of a droplet falling under gravity in a liquid of lower density depends on the size and shape of the droplet, densities, and viscosities of the droplet and surrounding fluids, acceleration due to gravity, and channel geometry. Hadamard (1911) and Rybczynski (1911) analytically derived the velocity and pressure fields in and around a spherical droplet moving in an infinite immiscible fluid in the creeping flow regime. As shown in Eq. (4.1), the terminal velocity of the droplet (U_t) falling/rising in another liquid because of gravity can be obtained by balancing the gravitational and drag forces experienced by the droplet.

$$U_t = \frac{2}{3}\frac{R^2 g|\rho_d - \rho_c|}{\mu_c}\frac{(\mu_c + \mu_d)}{(2\mu_c + 3\mu_d)} \tag{4.1}$$

Where μ_d, and ρ_d are the viscosity and density of the droplet and μ_c, and ρ_c are the viscosity and density of the surrounding liquid, and R is the droplet radius. They theoretically suggested the presence of vortices inside the droplet. Later, the internal circulation patterns inside the droplets were confirmed experimentally by several researchers (F. H. Garner and P. J. Haycock, 1959; Garner et al., 1954; Garner and Skelland, 1955; R.H. Magarvey and Juris Kalejs, 1963; Savic, 1953). Spells (1952) investigated the internal circulation experimentally using photography and captured circulation patterns for glycerin and glycerin-water mixture in castor oil for different droplet terminal velocities. Savic (1953) investigated internal circulation within water droplets in castor oil using images of suspended aluminium particles in the liquid. The effect of interfacial tension on circulation was investigated. Hu and Kinter (1955) studied the motion of ten organic liquid droplets falling through quiescent water media. A correlation is developed to predict the terminal velocity and drag coefficient for an equivalent drop size. Abdel-Alim and Hamielec (1975) numerically investigated the flow around spherical droplet in a liquid medium for Reynolds numbers (Re) between 1 and 50 and compared the drag coefficient with those obtained experimentally. Oliver and Chung (1985) investigated the effect of density and viscosity ratios on the flow inside and around the fluid sphere at low Reynolds numbers employing a series truncation method. While the effect of the change in density ratio was negligible, the shear stress and drag coefficient increased with an increase in the viscosity ratio of the droplet fluid to that of the surrounding fluid.

Hudson (2010) investigated numerically the effect of channel aspect ratio on the circulation pattern in a spherical droplet in rectangular channels. It was suggested that the symmetry of recirculation inside droplets may be broken by confinement and the Marangoni effects. Waheed et al. (2004) investigated computationally the effect of fluid properties on the flow pattern and velocity of a droplet of liquid settling in a Newtonian liquid. Lekhlifi et al. (2010) numerically studied the motion of the water droplet in paraffin oil, employing the volume of fluid (VOF) method to model the two-phase flow in a two-dimensional computational domain. The authors studied the effect of the distance of the release point from the wall on the droplet motion and showed the flow field inside the droplet to be symmetric or non-symmetric depending on the distance of the release location from the wall. The trajectory of the droplet deviated from a straight line for the release points located near the wall. Khadamkar et al. (2017) computationally studied the motion of rising droplets of toluene and n-butanol in water in a confined geometry. Aminzadeh et al.(2012) investigated the motion of the Newtonian and non-Newtonian droplets at $50 < Re < 500$ experimentally for air and water as surrounding media.

Multiple droplets of different sizes achieve different velocities and may lead to coalescence, resulting in change in the interfacial area per unit volume (Clift, R. C., Grace, B. J., and Weber, 1999). The coalescence of droplets has been studied by several researchers in the presence of air as an outer fluid on the liquid surface and the superhydrophobic surface (Anthony et al., 2017; Bird et al., 2020; Brik et al., 2021; Charles and Mason, 1960; Khadiya et al., 2021; Kovalchuk et al., 2018; Mashayek et al., 2003; Paulsen, 2013; Rahmat and Yildiz, 2018; Sprittles and Shikhmurzaev, 2012; Wu et al., 2004). Eggers et al.(1999) studied analytically the behavior of the bridge formed between two drops during the early stage of coalescence. They derived an expression for neck growth for different outer fluid viscosities. Menchaca-Rocha et al. (2001) studied the coalescence of two mercury droplets using a video camera as well as by numerical simulations and confirmed the expression for neck size evolution suggested by Eggers et al. (1999). Further, neck radius evolution by using scaling laws is reported by several authors (Nowak et al., 2016; Paulsen, 2013; Rahman et al., 2019; Wu et al., 2004).

Paulsen et al.(Paulsen et al., 2014) studied the coalescence of bubbles and droplets in the presence of denser fluid. They developed a phase diagram to determine the regime of coalescence using inertial and viscous stresses. Khadiya et al.(2021) studied computationally the coalescence of the bubble in a microchannel and observed that the neck radius grows as $\sim t^{1/2}$ initially when it is away from the wall, but in the presence of the wall, it grows slowly and is proportional to $t^{0.1}$. Kovalchuk et al. (2018) studied the effect of surfactant on coalescence in confinement. The bubble coalescence inside liquid media is studied by several authors numerically as well, but the experimental study of the flow field inside the bubble/droplet is limited (Chen et al., 2017, 2011; Hasan and Zakaria, 2011; Liu and Palm, 2016; Thoroddsen et al., 2005). Most of the studies in the literature show qualitative data during coalescence, and very limited data is available for the flow field inside the droplets during coalescence (Paulsen et al., 2014). The dynamics of the shape evolution of coalesced droplets and the flow field inside droplets during the coalescence are important to develop a complete understanding of droplet-droplet coalescence.

The fluid motion inside a droplet is driven by the shear caused by the surrounding fluid at the interface. When the surface tension is constant, the shear at the interface depends on the viscosity of the surrounding fluid medium, droplet size and its velocity relative to the surrounding fluid. Most of the experimental studies reported in the literature are performed in an unconfined droplet. Numerical studies (e.g., Hudson (2010)) suggest that the flow surrounding the droplet and therefore, the shear at the interface becomes asymmetric when the droplet is confined asymmetrically. Consequently, the confinement also affects the fluid motion inside the droplet. Further, during coalescence of two droplets, the internal motion has a strong effect on the evolution of the shape of the resultant droplet.

In this work, we aim to study the internal motion inside a droplet confined between two parallel glass plates with the ends on the sides closed. The effect of droplet size and its distance from the centerline on the internal motion using particle image velocimetry (PIV) is investigated. A major challenge in the measurement of the internal motion in the spherical droplets using PIV is the curved droplet interface and the associated difficulties such as reflection, and optical distortion. The problem of curved interface can possibly be simplified by studying the internal motion inside the droplet confined between two parallel plates. The glass plates are coated with a hydrophobic material to allow free settling of the droplet under gravity. Further, the coalescence of two unequal-sized droplets is studied and the interface evolution and associated transient velocity field is measured.

4.2 Experimental Methodology

The velocity field inside a droplet falling under the effect of gravity inside a liquid medium is obtained using 2D particle image velocimetry (PIV) technique. The liquid is seeded with tracer particles in such a way that they follow the flow of the liquid faithfully. Further, instantaneous images of 2D droplets are captured at a fixed frame rate (fps). Cross-correlation of two consecutive images gives the displacement of the tracer particles, and dividing this distance with the time duration gives velocity vectors. The time duration between the images captured should be sufficiently small when compared with the time scale of the flow. A typical flow time scale for the problem at hand is the ratio of the droplet diameter and its terminal velocity. The smallest time scale of the flow turns out to be ~ 2s.

As the droplet is very thin, the out-of-plane motion of seeding particles is restricted, enabling the use of 2D PIV to study the velocity field inside the droplet. The details of channel preparation and PIV post-processing are explained in Sections 2.3 and 2.4. Experiments are performed to investigate the effect of droplet release distance from side walls, diameter, and viscosity ratio of the droplet to surrounding liquid on the recirculation inside the droplet, terminal velocity, and coalescence dynamics of the two droplets of different size.

4.2.1 Channel Preparation

In order to have the visual access to the channel, the channel is made up of two glass plates (slides) kept at a distance of 1 mm apart and sealed from the sides and bottom. To study the effect of side walls on the motion of droplets, the front and back walls must be hydrophobic so that droplet can move smoothly in the channel. Hence, the glass surfaces of the confined channel are coated with a hydrophobic material, Octadecyltrichlorosilane (OTS). Glass slides (76.2 mm × 25.4 mm × 1 mm) are first treated with isopropyl alcohol at 60 °C for 30 min followed by 30 min ozone treatment to remove all the contamination on it. 0.2% OTS solution in toluene is prepared by heating at 60 °C for 30 min, and cleaned glass slides are kept inside OTS solution for 30 min, followed by washing with nitrogen gas. Two such glass slides are kept apart at a distance of 1 mm and sealed from three sides, leaving the top opening for liquid injection. Sealing from sides is done using two 1 mm thick clean glass slides sandwiched between them on either side and UV superglue is used to attach and seal. The bottom opening is filled with a 5 mm silicone sealant. Black adhesive tape is used at the junction to avoid any light scattering during experiments.

4.2.2 Materials

Glycerol (74%) – water (26%) mixture (GW: density 1180 kg/m^3, viscosity 0.035 Pa.s, and surface tension 0.025 N/m) is used as the droplet fluid, and silicone oils of different properties are used as the surrounding or continuous fluid filled in the channel. Table 4.1 shows the properties of the different silicone oils. Poly Methyl Methacrylate (PMMA) particles (Dynoseeds Ltd.) are chosen for seeding the droplet. They are neutrally buoyant (PMMA particle density 1180 kg/m^3) in the droplet liquid and follow the flow faithfully. Each droplet is seeded with 0.05% PMMA particles.

Table 4.1. Physical properties of the continuous fluid.

μ_{Si} (Pa·s)	ρ_{Si} (kg/m^3)	$\lambda = \frac{\mu_{GW}}{\mu_{Si}}$
0.371	976	0.09
0.098	975	0.36
0.019	974	1.79

4.2.3 Experimental Set-up

A schematic diagram of the setup used in the experiments is shown in Figure 4.1a. A syringe pump (Holmarc SPLF 2) is used to control the release of glycerol-water droplets of different volumes. A syringe of 60 ml volume is connected to a steady needle at the top of the channel. The channel filled with silicone oil is placed vertically so that the wall effect on the droplet remains symmetric from all sides (Figure 4.1b). A high-intensity LED light (GSVITEC MULTI LED LT) is applied horizontally to the channel. The camera is positioned in the cross-sectional plane of the channel. As the droplet starts falling due to gravity and achieves terminal velocity, images are captured using a high-speed camera (IMPERX UX 50) at a resolution of 1024×1024 pixels and a frame rate of 125 frames per second. It may be noted that the exposure time is 0.25 ms for all the experiments.

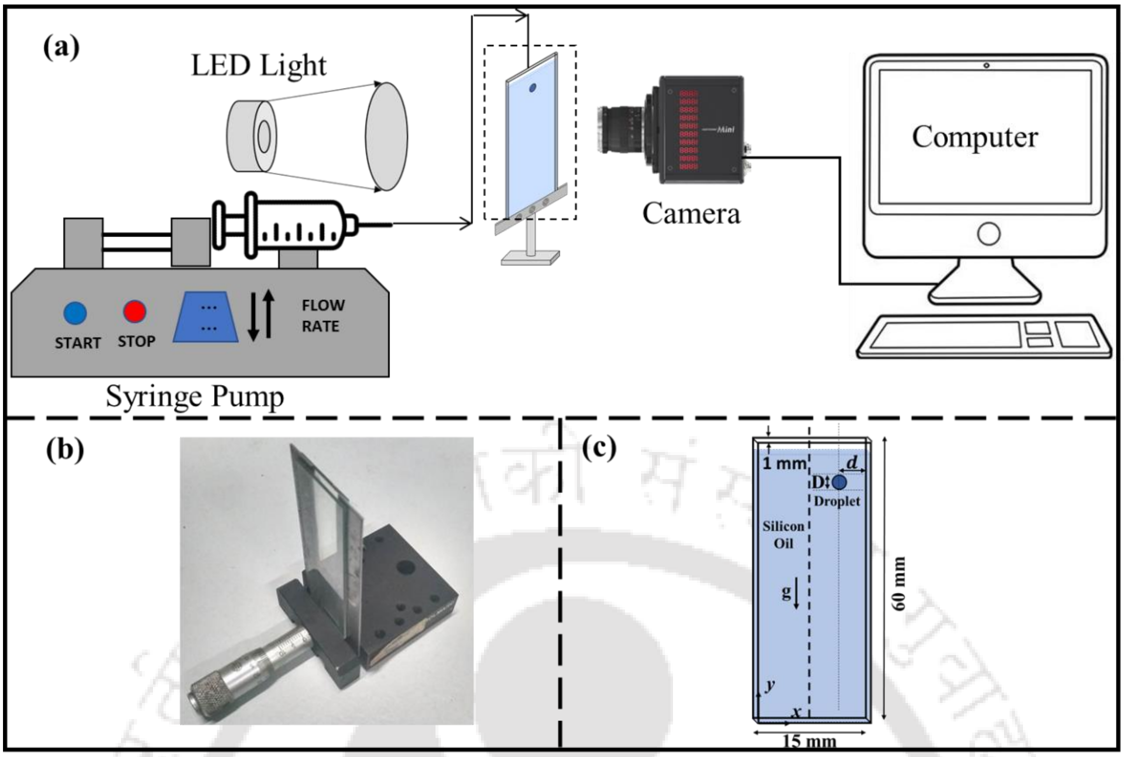

Figure 4.1. (a) Schematic of the experimental setup, (b) Used channel, (c) Schematic of the channel with droplet release position.

The camera is connected to a computer to record and process the images. Figure 4.1b shows an image of the channel which is used in the experiments. Figure 4.1c shows a schematic of the channel (60×15×1 mm) and droplet (diameter D) along with the release location (d). The length of the channel is chosen so as to provide well before it reaches the bottom. The droplet is released at the top of the geometry from three different locations (d/D = 1.72, 0.86, 0.43) with great care so as to avoid any fluctuations.

4.2.4 Image Processing and Particle Image Velocimetry

The images for PIV measurement are captured by the camera focused normal to the *xy* plane. Therefore, the camera captures the average motion of the particles in the *xy* planes. An ensemble of 200 images is captured and preprocessed using ImageJ (Schindelin et al., 2012) software for background subtraction. Figure 4.2 shows different stages of postprocessing performed with DynamicStudio 6.3 (Dantec dynamics), a commercial software, to obtain the velocity field. Imported images are calibrated with a scale of known length (Figure 4.2a). The region of interest (ROI), which includes the square region surrounding the droplet, is marked for further processing (Figure 4.2b). Pixels contain different intensity values of greyscale in an image ranging from 0−255 where 0 is completely black, and 255 is complete white. The noise and reflections present in the images are removed by calculating image Minima and subtracting from the parent image (Figure 4.2c and Figure 4.2d). Image Minima is defined as the minimum of power mean greyscale values, and the subtraction of Image Minima from the parent image is termed as Image Arithmetic. The maximum of power mean greyscale values (Image Maxima) from the series of images is calculated (Figure 4.2e) and utilized to apply a mask that eliminates area of no interest or area of no fluid flow (Figure 4.2f). After masking with the help of image maxima step, adaptive PIV algorithm is applied for 8×8 interrogation grid. To accommodate regional seeding densities and flow gradients, the adaptive PIV algorithm iteratively modifies the size and shape of individual interrogation areas (IA) and determines the appropriate IA size for each IA. The minimum IA size is kept at 16×16 while the maximum IA is 32×32 with a grid step size (number of pixels from one IA to its neighbor) of 8×8. The number of particles per IA is set to 10, controlling the appropriate IA size within the minimum and maximum range. Velocity vectors obtained are further processed for outlier removal, and an average filter is applied with a 7×7 averaging area for smooth vectors. To obtain velocity vectors in the droplet frame of reference, the vector plot is subtracted from the terminal velocity of the droplet.

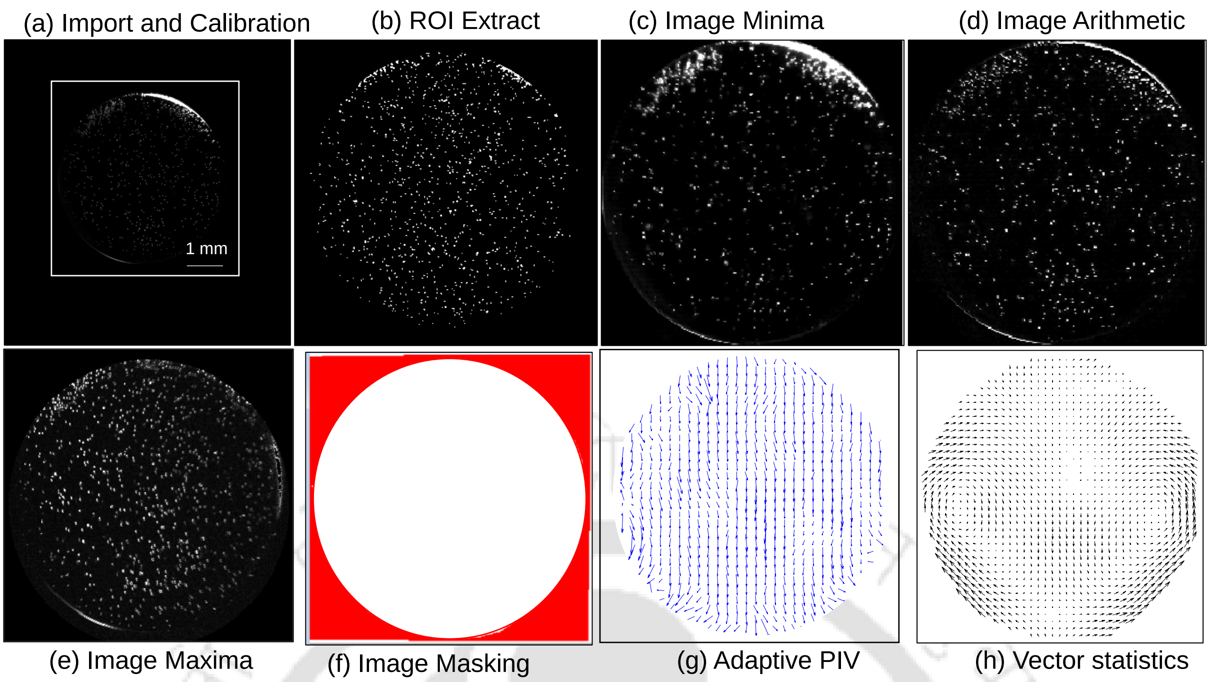

Figure 4.2. Image post-processing stages for particle image velocimetry.

4.3 Results and Discussion

4.3.1 Terminal Velocity

The viscosity of the surrounding liquid is varied while keeping the viscosity of the droplet liquid constant, resulting in three variations of $\lambda \left(\frac{\mu_{GW}}{\mu_{Si}} = 0.09, 0.36, \text{and } 1.79\right)$. Note that the increase in the viscosity ratio is caused by a decrease in the viscosity of silicone oil. Due to the confinement, the droplet cannot take a spherical shape. The shape of the droplet would be closer to that of the disc with some curvature effects. However, a liquid film separates the droplet from the wall, and the disc is expected to be curved at the periphery. The volume of the droplet is proportional to the square of the droplet diameter and its thickness. The known volume of the droplet is released, and the diameter of the droplet can be measured from the images.

Assuming the droplet thickness to be equal to the channel width (1 mm), a theoretical droplet diameter (D^*) can also be calculated for the given droplet volume by $D^* = \sqrt{\frac{4V}{\pi(1mm)}}$, where V is droplet volume. In Figure 4.3, the variation of the square of the experimentally measured and theoretically calculated (D*) droplet diameter with the droplet volume is plotted. Repetition of the experiment exhibits a maximum 3.8% error in diameter (D) measurement and 7.6% in D^2 measurement, which is shown as an error bar. The variation of square of the theoretical (D*) as well as experimentally observed diameter is linear with the volume (V).

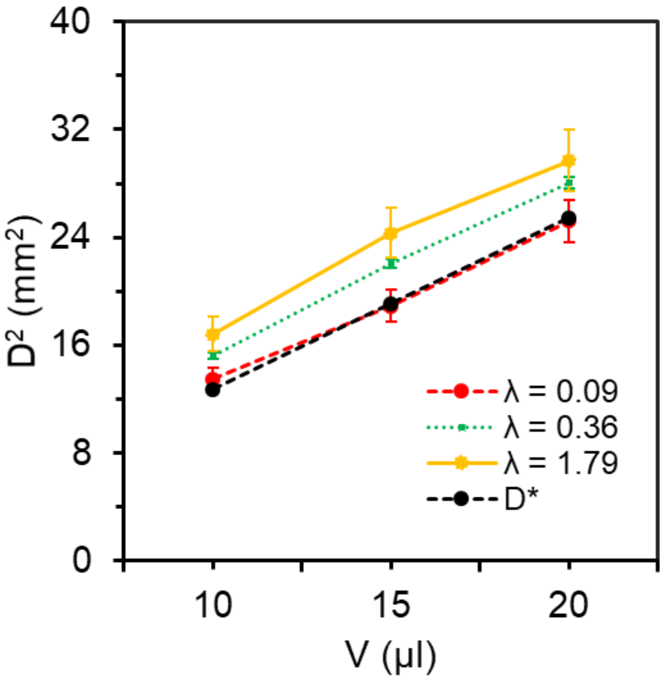

Figure 4.3. Observed and theoretically calculated (D*) diameter of the disc-shaped droplet at different volumes for different viscosity ratios $\lambda = \mu_{GW}/\mu_{Si}$.

It is evident from Figure 4.3 that the measured droplet diameter exceeds the theoretical calculation for the cases of λ = 0.36 and 1.79. The large difference indicates the presence of a liquid film between the droplet and the channel wall. The presence of a thin liquid film causes a small increase in the diameter. However, the measured diameter is nearly equal to the theoretical calculation for λ = 0.09. When the droplet is released into the liquid, it starts accelerating and eventually achieves a terminal velocity. The droplet experiences a downward force due to gravity, an upward force caused by buoyancy, and an upward drag force caused by form and viscous drags. The terminal velocity is achieved when all these forces balance each other. Figure 4.4a shows the variation of terminal velocity of the droplets with droplet diameter at different viscosity ratios, and the detailed data is provided in Table 4.2.

Table 4.2 Droplet diameter, terminal velocities measured in the experiments, and fluid properties and terminal velocity calculated using the H-R relation

D (mm)	ρ_c	ρ_d	μ_c	μ_d	Re	λ	U_t (mm/s)	
							H-R (1911)	Exp
3.67	976	1180	0.371	0.035	0.0016	0.09	5.92	0.17
4.35	976	1180	0.371	0.035	0.0021	0.09	8.31	0.18
5.02	976	1180	0.371	0.035	0.0028	0.09	11.07	0.21
3.9	975	1180	0.0976	0.035	0.0308	0.36	23.52	0.79
4.7	975	1180	0.0976	0.035	0.039	0.36	34.16	0.83
5.3	975	1180	0.0976	0.035	0.047	0.36	43.43	0.88
4.1	974	1180	0.0195	0.035	0.424	1.79	112.02	2.07
4.93	974	1180	0.0195	0.035	0.532	1.79	161.96	2.16
5.45	974	1180	0.0195	0.035	0.604	1.79	197.93	2.22

The terminal velocity increases with an increase in the droplet diameter for all three values of λ. The increment in the velocity with an increase in the diameter is 3.0% for the smallest viscosity ratio (λ = 0.09). However, with increasing λ, the rise in terminal velocity with an increase in diameter is merely 6.4% and 11.1% for λ = 0.36 and 1.79, respectively. A decrease in the viscosity of the surrounding liquid leads to an increase in the terminal velocity of the droplet, as the viscous drag experienced by the droplet increases with an increase in the viscosity of the surrounding liquid. The terminal velocities are compared (Table 4.2) with those calculated using the analytical solution given by Hadamard (1911) and Rybczynski (1911), as shown in Eq. (4.1). The estimated velocity is one order of magnitude greater than the experimentally observed results at all values of λ. However, the estimated velocity is for a spherical-shaped droplet, and the experimentally measured velocity is for a disc-like droplet.

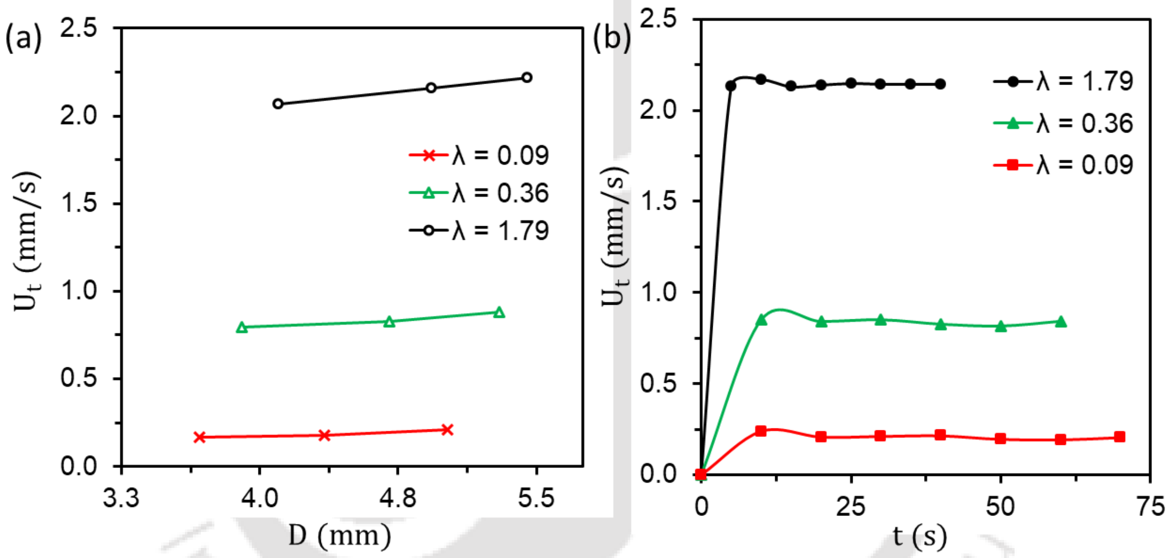

Figure 4.4. (a) Terminal velocity variation with the diameter and (b) Terminal velocity evolution with time for droplet volume of 15 μl for three different viscosity ratios $\lambda = \frac{\mu_{GW}}{\mu_{Si}}$.

Figure 4.4b shows the variation of terminal velocity of the falling droplet of 15 μl volume released at the center of the channel with time (d/D= 1.72). A sequence of images at 30 fps is captured to track the movement of the droplet while falling through silicone oil. Marking the distance traveled at different time instants results in the terminal velocity of the droplet. Because of the greater viscosity of the surrounding fluid, the droplet with the smallest λ achieves the least magnitude of terminal velocity. Similarly, as λ increases, terminal velocity increases because the surrounding liquid is less viscous and offers less drag force. It is observed that the time taken to achieve terminal velocity is smaller for the less viscous surrounding liquid.

Figure 4.4b also shows that the time taken to achieve the terminal velocity for all three cases is well below 15 seconds, and the maximum distance traveled by the droplet to achieve the respective terminal velocity is 20 mm. Since the set-up is 60 mm long, the observation point is chosen at 30 mm from the top, which enables us to observe all the droplets well after achieving their terminal velocity as well as there is no effect of the bottom of the channel. Droplet diameter and terminal velocity investigation suggest the use of λ = 0.09 (highest viscosity of surrounding liquid) case (because of the nearly disc-shaped droplet and smaller distance taken to achieve terminal velocity) for 2D PIV (Legendre et al., 2008).

4.3.2 Velocity Field in the Droplet

Figure 4.5(a-c) show the velocity field inside the droplet in a frame of reference moving with the droplet for three droplets of different volumes released at the center of the channel (d/D = 1.72). The horizontal and vertical diameters of each droplet are shown, each of which divide the droplet in two halves. As the droplet falls, it displaces the continuous fluid in the channel, and this displaced fluid moves upward to fill the gap created by the droplet. In the droplet frame of reference, the surrounding liquid moves past the droplet, and a stagnation point, i.e. the point at which fluid velocity becomes zero, is observed at the bottom of the vertical diameter of the droplet. The surrounding fluid moves tangentially past the droplet, causing a tangential stress on the droplet fluid. As a result, the droplet fluid at the droplet boundary moves upward, and eventually, a vortex is established on either side of the vertical diameter. As a result, a pair of symmetric, counter-rotating vortices are observed inside the droplet. The plus symbol (+) denotes the position of the center of vortices in the figure.

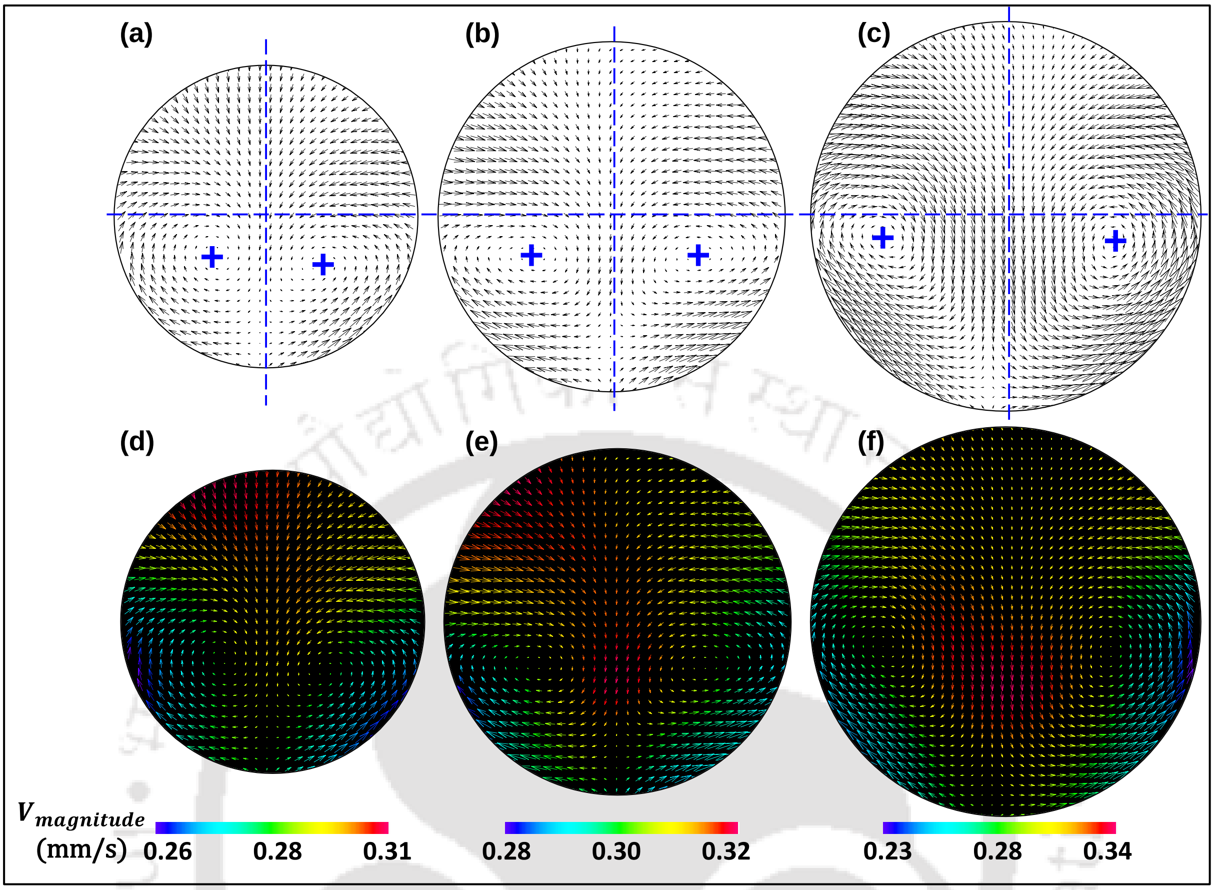

Figure 4.5. Velocity vectors inside droplets of different volumes (a)10 μl, (b) 15 μl, and (c) 20 μl, and colored plot with velocity magnitude of respective volumes (d)10 μl, (e) 15 μl, and (f) 20 μl, released at the center ($d/D = 1.72$) of the channel. The symbol (+) shows the location of the vortices from the horizontal and vertical centerlines.

The centers of both vortices are observed to be in the bottom half of the droplet in each case. The location of the vortex centers moves upward, closer to the horizontal diameter and away from the vertical diameter, as the size of the droplet increases. This suggests that the surrounding fluid is able to drag the droplet fluid to a higher distance with an increase in the droplet diameter. The average velocity of the surrounding fluid ($U_{o,H}$) at the horizontal diameter can be obtained using a simple mass balance (volume balance as the fluids are incompressible).

Mass balance gives $U_t D l = U_{O.H}(L - D) l$ or $U_{O.H} = U_t D/(L - D)$ where L and l are the channel width and depth. Therefore, the shear stress (τ) in the surrounding fluid at the horizontal diameter will be $\tau \sim 2\mu_c U_t D/(L - D)^2$. As the droplet diameter, D, increases, the value of terminal velocity and consequently, the shear stress will also increase. Therefore, the droplet fluid will be dragged higher with an increase in the droplet diameter. This is observed in the experiments clearly. The velocity magnitude is shown in Figure 4.5(d-f) for the three cases. The magnitude of velocity inside the droplet is of the order of droplet terminal velocity (0.17 – 0.21 m/s).

Figure 4.6 shows the velocity vectors inside the droplets of volume 15 μl released at three different locations (d/D = (a) 1.72, (b) 0.86, and (c) 0.43) from the wall. Note that the distance is from the wall on the right (R) side of the droplet. It may be noted that the case shown in Figure 4.6(a) is the same as that shown in Figure 4.5(b, e) and is shown for the comparison with the two near wall cases. When the release point is not at the center, a small horizontal component of terminal velocity is observed, which is ~1% of the vertical component of terminal velocity. The horizontal component of droplet velocity is obtained by averaging the *x* component of velocity in all pixels.

When the droplet is released from a location different from the center, two vortices are observed at the bottom of the droplet in the droplet frame of reference (Figure 4.6b and Figure 4.6c). However, the vortices are not symmetric. The positions of both vortices shift in the droplet as the release point of the droplet shifts toward the wall. The right vortex inside the droplet moves upwards, closer to the horizontal diameter, whereas the left (L) vortex moves slightly down in the droplet. This behavior can again be explained by the shear stress on the left and right sides of the droplet. The distance between the wall and the droplet increases on the left side, whereas decreases on the right side for the near wall cases. This would result in an increase in the shear stress on the right side and a decrease on the left side if there is a significant change in the flow rate distribution on the two sides of the droplet. The position of the vortices suggests the assumption to be true. Figure 4.6(d-f) shows the velocity vectors colored by their magnitude.

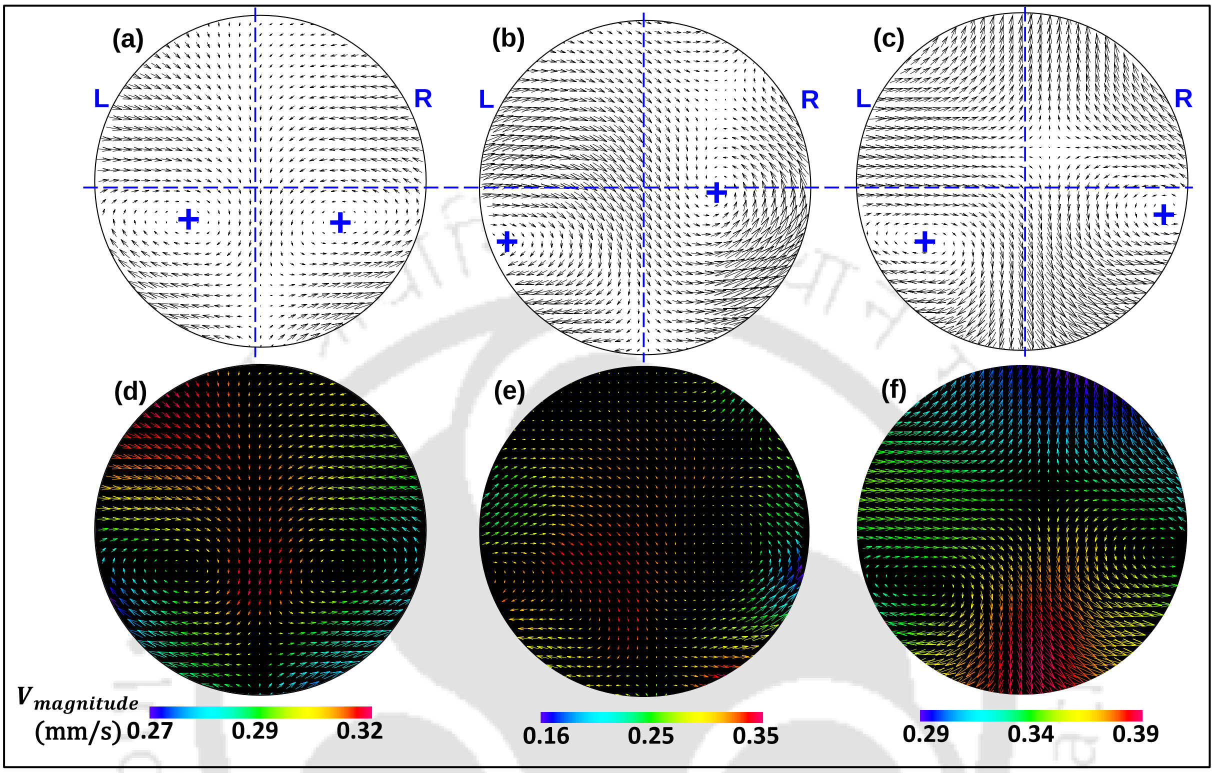

Figure 4.6. Velocity vectors inside the 15 μl droplet released at three different locations d/D = (a) 1.72, (b) 0.86, and (c) 0.43 from the wall.

4.3.3 Coalescence of the Droplets

It is clear from Sections 3.1 and 3.2 that a bigger droplet has a terminal velocity higher than that of the smaller one. Therefore, if a smaller droplet is followed by a bigger one, coalescence between them would occur. In order to capture the coalescence phenomenon in the experiments, a droplet of volume 12 μl is released at the center of the channel, followed by another droplet of volume 18 μl after a certain time. The time gap between the release of two droplets is chosen such that coalescence between them could occur before the droplets reach close to the bottom of the channel. The viscosity ratio is λ = 0.09. Both droplets are seeded with tracer particles in order to capture the local velocity field during coalescence.

Figure 4.7 shows the evolution of the shape of the two droplets during coalescence. Both the droplets achieved terminal velocities of 0.39 mm/s and 0.36 mm/s before coalescence. Figure 4.7a shows the droplet images before the droplets coalesce. Though care and effort have been made to keep the droplets aligned, it may be noticed that the droplets are not perfectly aligned, and a line connecting their centers is at a small angle with the vertical direction (y). As the bigger droplet approach small one, the liquid between them would move out in a direction normal to the line connecting the centers of the two droplets.

The larger droplet (volume 18 µl) approaches the smaller droplet (volume 12 µl) due to its higher terminal velocity during film drainage, and the surrounding liquid present between the vicinity of the droplets moves away from the approaching interfaces, as shown in Figure 4.7a. During this period of the approach of droplets, the velocity of the bigger droplet decreases. Eventually, the velocity of the bigger droplet becomes equal to that of the smaller droplet, and both droplets come in contact with each other, as shown in Figure 4.7b. A neck forms between the two droplets and grows with time, as can be seen in Figure 4.7c, d and e. During this period of neck growth, the combined droplet or doublet also keeps moving down. The shape of the neck changes continuously during the coalescence. Initially, the neck is concave, and the radius of curvature grows with time, as can be seen in Figure 4.7b, c, and d. Eventually, the interface at the neck becomes straight (infinite radius of curvature), as seen in Figure 4.7e, and then the curvature is inverted, and the interface becomes convex, as seen in Figure 4.7f. This completes the merger of the droplet, and a new, bigger droplet forms.

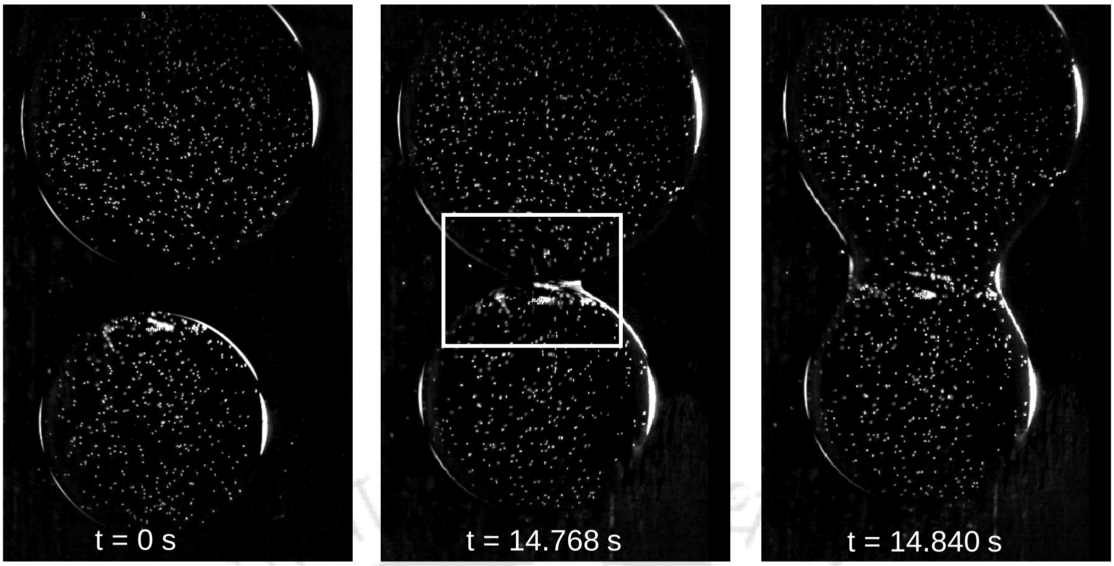

(a) Approaching towards smaller droplet (b) Interface rupture (c) Growth of newly formed interface

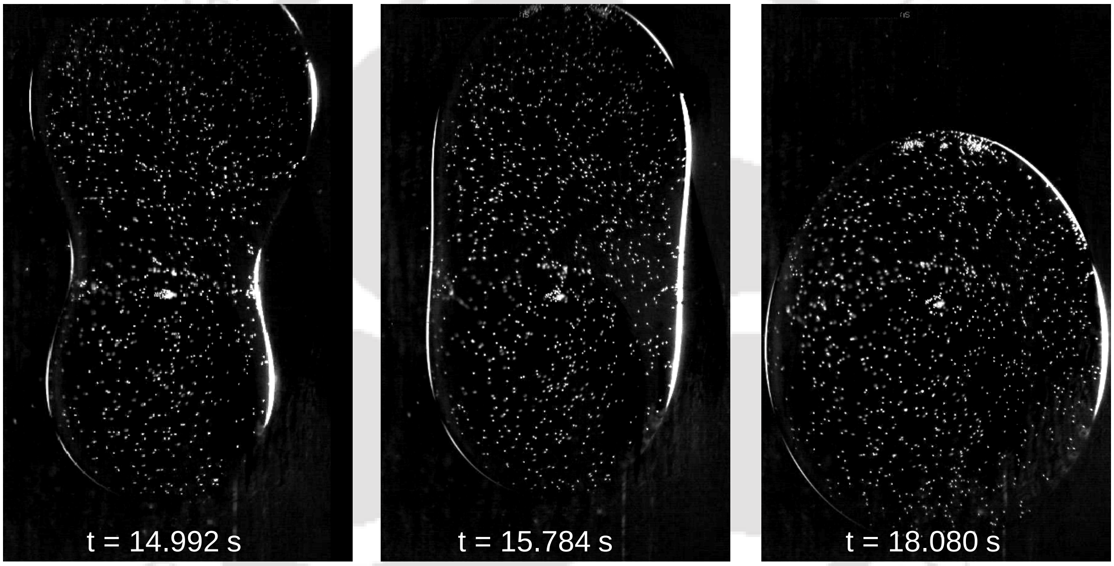

(d) Neck growth (e) Neck growth (f) New Droplet

Figure 4.7. Time evolution of two droplet coalescence of 18 μl and 12 μl volume at the center (d/D = 1.72) of the channel.

The evolution of the neck radius with time has been studied during the coalescence of bubbles and droplets by several researchers. Neck radius is the distance between the line connecting the centers of the two droplets and the neck interface. An expression for the initial stage of the neck growth for coalescence of spherical droplets in the presence of surrounding liquid is given by Paulsen et al.(Paulsen et al., 2014) given by Eq. (4.2).

$$\frac{r}{R_{Droplet}} = C_0 \left(\frac{t}{t_{out}}\right)^{1/2} \tag{4.2}$$

Where C_0 is a dimensionless pre-factor chosen as 1.2, $t_{out} = \sqrt{\rho_c R_{Droplet}^3/\sigma}$, and ρ_c is the density of the surrounding or outer liquid. Experimentally observed variation of dimensionless neck radius with time (non-dimensionalized by t_{out}) is plotted in Figure 4.8 along with that calculated by Paulsen et al. (2013), Kovalchuk et al.(2018) and Brik et al. (2021) In Figure 4.8, the evolution of neck radius with time is plotted for the entire duration of neck growth. The zoomed view shows the neck growth during the initial stage of the coalescence. Kovalchuk et al. (2018) studied the effect of surfactant on the coalescence of water droplets inside silicone oil in microchannel and found that the presence of surfactant slows down the growth of the neck radius. There is a good agreement between our experimental data and that shown by Kovalchuk et al. (2018) with surfactant shown in green color. However, in the absence of surfactant, the neck radius grows faster. Neck radius growth during the coalescence of vertically aligned water droplet inside toluene, studied by Brik et al. (2021), is observed to be faster than our data. Similar results are also observed by Eiswirth et al. (2012) for the coalescence of rising toluene droplets inside water. In our experimental data, it is observed that initial growth is linear with a smaller slope than all the available literature except Kovalchuk et al. (2018) data without surfactant. Further, growth becomes non-linear at r/R = 0.4 with a continuously decreasing slope.

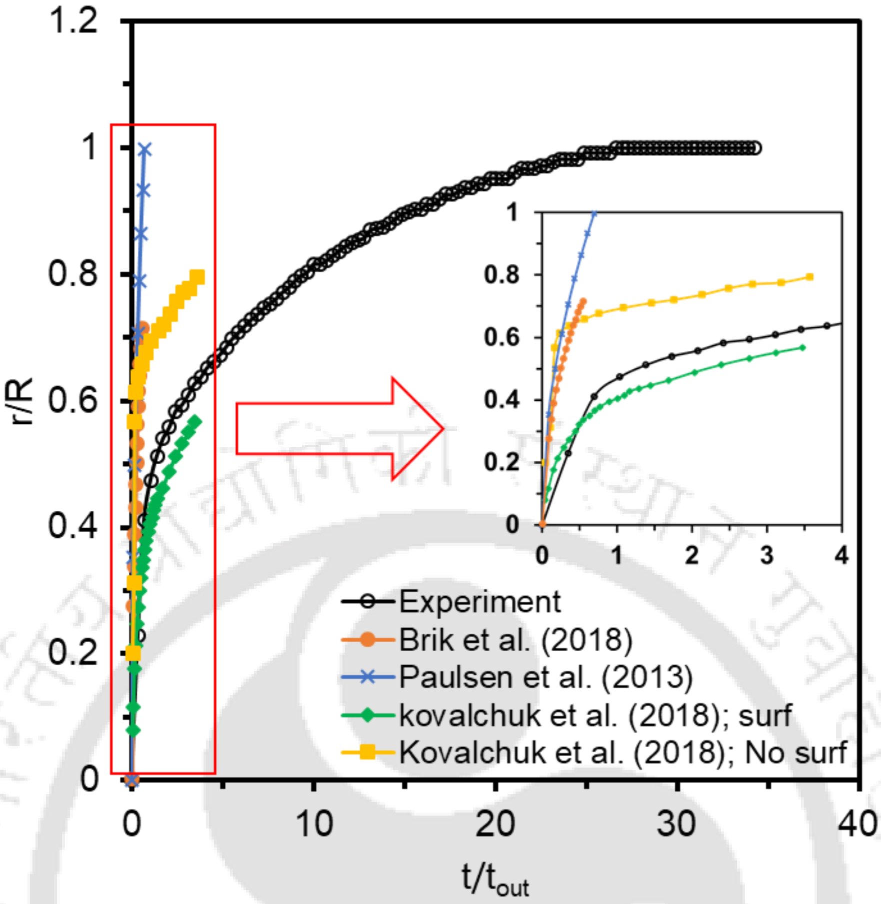

Figure 4.8. Evolution of neck width with time during coalescence of 12 μl and 18 μl droplets at the center of the channel. Growth of neck width till it becomes equal to the radius of the newly formed droplet, and zoomed view of the growth of neck width at the early stage.

As the two droplets merge and the neck radius grows, the fluid motion inside the droplet is rearranged such that the droplet fluid at the neck pushes the neck with the interface velocity. This can be clearly seen in the velocity vectors near the neck region (marked rectangular region in Figure 4.7b) shown in Figure 4.9. The vectors are in a frame of reference, moving with the doublet. At t = 14.768 s, two thin horizontal jets push the droplet fluid outwards (pushing the interface) with a velocity of ~ 5 mm/s. Soon after, at t = 14.776 s and 14.784 s, the size or width of the two horizontal jets grows. After a few ms, at t = 14.800 s and 14.808 s, the velocity of the jet fluid decreases, suggesting a decrease in the rate of neck growth, and at t = 14.968 s, the velocity in the horizontal jet is significantly reduced. This can also be verified by the graph of neck growth in Figure 4.8. In fact, the rate of neck growth is of the same order as the fluid velocity at the corresponding time instants. The horizontal jets form by the fluid brought by both the droplets. While some fraction of the fluid brought by the droplet goes in the horizontal jet, the remaining fluid recirculates, forming vortices in each droplet.

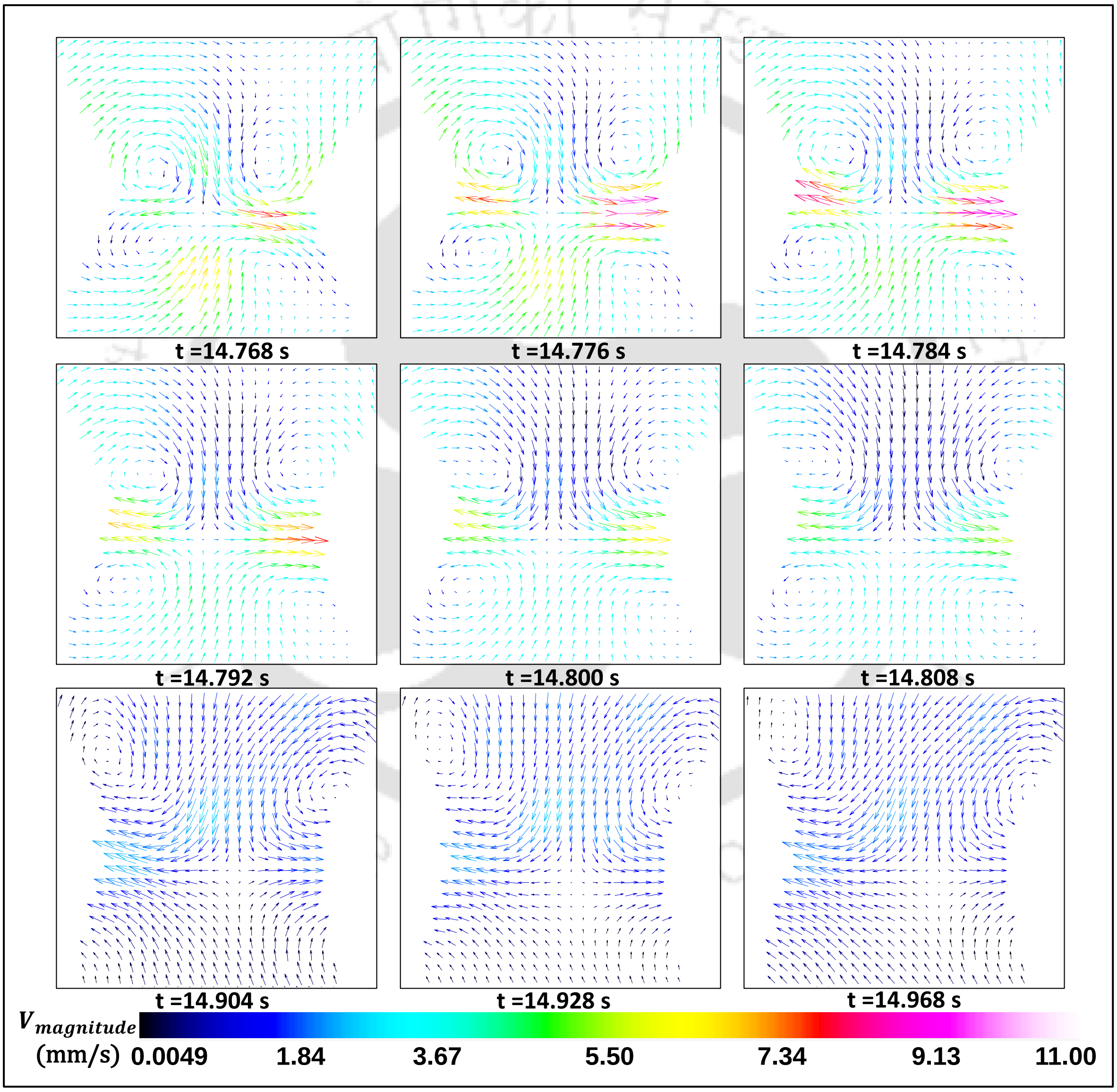

Figure 4.9. Evolution of velocity vectors during coalescence at different time instants.

As a result, four counter-rotating vortices are observed near the neck (symmetric to the horizontal and vertical axis). Similar counter-rotating vortices are also observed by Brik et al. (2021), Kovalchuk et al. (2018), and Eiswirth et al. (2012) As the droplet fluid is incompressible, the growth of the neck causes a reduction in the size of the droplets in the vertical direction. As can be seen in Figure 4.7(d), the size of the bigger droplet decreases, and the smaller droplet increases during this process. This suggests that there is a net movement of fluid from the bigger droplet to the smaller droplet. One possible mechanism for this might be that the fluid in the horizontal jet might eventually turn towards the smaller droplet. However, further detailed investigations are needed to understand this, as the fluid movement in coalescing droplets has implications in droplet-based reactors and biological assays.

4.4 Summary

The flow inside a droplet falling under the effect of gravity in a continuous liquid in a high aspect ratio rectangular channel was studied using particle image velocimetry to investigate the effect of droplet diameter and distance from the wall. For the droplet released at the center of the channel, two symmetric counter-rotating vortices driven by the tangential stress at the interface (caused by the surrounding fluid) are observed in the droplet frame of reference. The vortices were located next to the stagnation point of the droplet. An increase in the droplet diameter resulted in increased tangential stress at the interface and consequently, more fluid recirculated and the size of the vortices grew. When the droplet was released from a location between the channel centerline and sidewall, the tangential stress on the droplet interface and consequently the fluid motion became asymmetric. The closer was the release location to the wall, the higher was the center of the vortex near the wall and the lower was the vortex near the centerline.

The coalescence experiments were performed by releasing a smaller droplet followed by a bigger droplet at the channel center. The bigger droplet slowed down and coalesce with the smaller droplet when their velocities became equal. As the droplets coalesce, the coalescence point grew to take a neck-like shape, which grew rapidly in the beginning and then widen slowly. The growth of the neck was accompanied by the velocity directed radially outward at the neck, having velocity equal to the rate of neck growth. A pair of counter-rotating vortices were observed on each side of the neck. These vortices readjusted the fluid such that the droplet gained the shape of a single bigger droplet.

Chapter 5. Droplet Falling in a Liquid Media in a Rectangular Channel: 2D CFD Simulations

5.1 Introduction & Literature Review

The phenomena of a liquid droplet moving inside another fluid media have always been fascinating to researchers. It becomes more critical when a tiny droplet (micro) moves inside small diameter channels like Hele-Shaw setups. The movement of droplets in a continuous fluid is important in industries like chemicals, pharmaceuticals, and petrochemicals. The knowledge of internal flow patterns of the droplets helps in improving technologies such as gas turbines and internal combustion engines, emulsions, droplet reactors, and mixers. Numerous studies have investigated the flow patterns inside droplets over the past few decades, as they fall through more viscous fluids.

Hadamard (1911) and Rybczynski (1911) initially developed theoretical solutions a low Reynolds number flow in and around liquid spheres extending Stokes' solution for axisymmetric flow around a solid sphere in creeping flow. The study also calculated streamlines from analytical results for Hadamard flow (Reynolds number approaching zero) within spherical droplets. Spells et al. (1952) investigated the circulation patterns within liquid drops moving through another liquid. They conducted an experimental study on the internal circulation in a glycerin drop falling through castor oil, marking the first published evidence of such internal flow phenomena in falling drops. Hu & Kinter (1955) investigated the movement of individual drops of ten different organic liquids falling through a stationary water medium. Their study utilized a glass-walled tank measuring 1×1×4 ft, with drop diameters ranging from 1.6×10^{-4} to 2 mm. They determined the terminal velocity for each organic liquid and developed a generalized plot relating terminal velocity to drop diameter. Additionally, they analyzed the variation in drag coefficient with Reynolds number and established critical drop size criteria based on their findings. Ahmed et al. (1975) conducted both theoretical and experimental investigations on the impact of drag forces on the internal circulation within spherical droplets falling with terminal velocity in a liquid medium. Their study spanned Reynolds numbers ranging from 1 to 50 and computed velocities and drag forces for liquid-liquid systems. The researchers numerically solved the Navier-Stokes equations across various viscosity and density ratios. They also analyzed the surface velocity variation with polar angle for different viscosity ratios at a Reynolds number of 50. Ahmed et al. observed that vorticity tended to concentrate in the lighter fluid, significantly influencing the overall dynamics of the system. Sadhal et al. (1983) examined the flow patterns around a droplet falling within an external velocity field. They developed solutions for uniform external fluid flow in perpendicular direction to falling droplet. The study explored how the drag force, caused by tangential momentum from radial velocity, affects the circulation inside the droplet. This circulation is influenced by the droplet's outward normal velocity. Oliver and Chung (1985) examined the steady flow patterns within and around a fluid sphere under low Reynolds number conditions. They utilized semi-analytical methods involving series truncation to analyze the influence of internal circulation within droplets. The study investigated the impact of density differences on drag coefficients, which were found to be minimal at low Reynolds numbers across all density ratios. Additionally, they observed that shear stress and drag coefficients increased with higher viscosity ratios of the droplet to the surrounding fluid, and decreased as Reynolds numbers increased. Yamauchi et al. (2000) analyzed velocity distributions both inside and outside of water droplets immersed in oil. They investigated the boundary conditions at the interface between the two fluids, focusing on measuring velocity distributions in the immediate vicinity of the interface. The study also evaluated variations in shear stresses on the interface of water droplets in oil. Experimental analysis utilized droplets ranging from 12 to 15 mm in diameter, employing particle tracking velocimetry (PTV) techniques. Belmonte and Sostarecz (2003) investigated the movement and deformation of a viscoelastic droplet falling through a viscous medium. They examined the behavior of a polymer solution droplet falling through a quiescent Newtonian fluid. Their study used an immiscible drop consisting of 0.16% xanthan gum in an 80:20 glycerol/water mixture falling through polydimethylsiloxane oil with a viscosity of 9.8 P. Increasing the droplet volume led to a transition of its free surface from a spherical shape primarily due to non-Newtonian effects. Specifically, they observed the instability of the growing dimple in non-Newtonian droplets falling through a Newtonian fluid. Waheed et al. (2004) conducted a study on simulating the sedimentation of liquid drops to investigate how fluid properties affect flow patterns and settling velocities in Newtonian fluids under asymmetrically stable conditions. They utilized the finite volume method to solve the governing equations of motion, finding that droplet flow patterns were significantly influenced by Reynolds number and the viscosity ratio between the droplets and surrounding fluid. The study showed that viscosity ratios ranging from 0.02 to 50 affect the drag coefficient, and they presented a correlation for sedimentation velocity consistent with experimental findings, highlighting internal droplet circulation during settling in a continuous medium. Wanchoo et al. (2009) investigated the motion and shape of a single Newtonian droplet moving through a static immiscible viscoelastic liquid. They explored various combinations of continuous phases including distilled water, glycerol in distilled water, CMC in distilled water, polyvinyl pyrrolidone in distilled water, PEO in distilled water, and low and high viscous Polyacrylamide (PAM) in distilled water, with dispersed phases such as Carbon tetrachloride (CCl_4), Bromobenzene (BB), Chlorobenzene (CB), Nitrobenzene (NB), Nitrotoluene (NT), and ethyl chloroacetate (ECA). Their study focused on analyzing the droplet shape and eccentricity as it moved through these immiscible non-Newtonian liquids. They generated a regime graph correlating drop shape with its motion in the immiscible non-Newtonian liquid and investigated how physical properties and system parameters influenced drop eccentricity. Terminal velocity and eccentricity were studied in relation to drop diameter. Steven et al. (2010) investigated Poiseuille flow and drop circulation in microchannels within the context of microfluidics, which aims to precisely control fluid and particle transport. They examined the circulation patterns of drops in rectangular microchannels and discussed measurements of interfacial mobility. Tripathi et al. (2014) conducted a comparative study between falling drops and rising bubbles, simulating both phenomena to explore their differences. They examined the influence of Galilei number and viscosity ratio on internal circulation dynamics, emphasizing how vorticity tends to concentrate in lighter fluids, impacting overall kinetics. The study argued that drops and bubbles, descending or ascending under gravity in their respective fluids, do not generally exhibit mirrored behaviors. However, they discovered that a Hadamard bubble could display a flow history similar to that of a solid drop under certain conditions. Numerically, they found hydrodynamic similarities between bubbles and drops when average surface tension and inertia were closely matched, particularly when density ratios were near unity. In axisymmetric flows, vorticity concentrated near the base and interface of the bubble, resulting in a central pinch-off phenomenon, contrasting with the cup-like shape typically exhibited by drops. Robert et al. (2014) explored the circulation patterns within confined droplets in Hele-Shaw channels using a microfluidic device. They observed that liquid droplets flowing through rectangular channels develop a vertical flow field due to shear forces from surrounding fluids. Their study proposed both experimental and computational analyses of droplet velocities and internal flow patterns. The velocity of fluid inside and outside a liquid drop was computed using continuity and Navier-Stokes equations. Kishore et al. (2006) investigated sedimentation in emulsions consisting of monodisperse droplets at moderate Reynolds numbers. They utilized simple concentric spherical cells to elucidate the fluid dynamic interactions between particles. The study presented numerical results for the pressure coefficient ($C_{D,p}$), frictional coefficient ($C_{D,f}$), and total drag coefficient (C_D) as functions of the Reynolds number of the continuous phase. Lekhlifi et al. (2010) conducted detailed numerical simulations to explore the unsteady hydrodynamics of pure water droplets immersed in a continuous phase of paraffin oil. The researchers utilized a two-dimensional setup within a confined square box measuring 1 cm × 1 cm, releasing droplets from varying initial positions. To simulate the fluid dynamics, they employed the Navier–Stokes equations for incompressible fluids, implementing the volume of fluid method. Their investigation focused on evaluating the time-dependent average settling velocity of the droplets and analyzing their hydrodynamics. They suggested the unstable evolution of droplets and proposed numerical simulations applicable to understanding complex fluid systems such as emulsions. Due to gravitational forces, the droplets descended towards the bottom of the system, exhibiting unsteady hydrodynamic behavior across three distinct regimes. Ervik et al. (2014) investigated the behavior of sub-millimeter water droplets falling through viscous oil under an electric field, relevant for industrial applications like crude oil electrocoalescence. They conducted experimental and numerical studies, incorporating surfactants to prevent surface chemical contamination. Their research focused on terminal velocities and droplet responses to sudden electric field changes, confirming calculated terminal velocities for clean systems aligned with predictions from the Hadamard-Rybczynski formula. Lekhlifi et al. (2015) conducted a numerical investigation into the drainage behavior of water droplets in paraffin oil, employing a surfactant to modify the droplet. The surfactant was assumed to be insoluble in paraffin oil and less soluble in water. The study focused on exploring the effects of poorly soluble surfactants, which alter the properties of the water-oil interface and introduce capillary phenomena. The trajectory of droplet drainage was analyzed based on the initial concentration of the surfactant and the initial position of the droplet. The researchers hypothesized that all surfactant molecules were adsorbed at the interface, leading to Marangoni convection. This convection acted in opposition to gravity, thereby reducing the overall drainage velocity of the droplet. They observed that hydrodynamics inside the droplets was complex in asymmetric systems and simpler in symmetric configurations. They also quantified the influence of drag and buoyancy forces, which manifested in varying trajectories for the droplets during settling. Mohammadi et al. (2016) studied the internal flow dynamics of a 2 mm water droplet moving within a confined chamber filled with paraffin oil. They utilized a Multiphase VOF solver for numerical simulations, analyzing the swirling strength and velocity components of the droplet's inner flow field. Khadamkar et al. (2017) performed computational fluid dynamics simulations on single drops in confined geometries, using the ratio of droplet diameter to column diameter to assess wall effects. Their study focused on n-butanol and toluene dispersed in water, observing reduced rising velocities due to pressure profiles, strain rates, and vorticity magnitudes near the drop surface. They calculated drag coefficient using force balance equations and employed VOF, level set, and combined level set and VOF methods to track droplet interfaces, using droplet diameters ranging from 1 to 6 mm. Their findings evaluated transient rise velocity behaviors and correlations for drag coefficients in the presence of wall effects.

Based on the literature review, it is evident that understanding the dynamics of droplets falling through liquid media is crucial. The diameter of the droplet, wall effects, and the viscosity of the surrounding liquids can significantly influence the recirculation patterns both inside and outside the droplet. Therefore, this numerical study aims to investigate the recirculation behavior of droplets falling within a confined channel under the influence of gravity. Key parameters considered include the droplet's release position from the wall, its diameter, and the viscosity ratio between the inner and outer liquids.

Experimental study (discussed in Chapter 4), show that vortices inside droplet become asymmetric when released and fall near wall. The numerical study for same parameter can provide the reason for asymmetric recirculation and enhance the understanding. Similarly, the effect of diameter at different release location along with the effect of viscosity ratio are interesting to investigate using numerical simulation as experiments are done only on one viscosity ratio ($\lambda = 0.09$).

5.2 Numerical Methodology

Two-dimensional CFD simulations are done to investigate the effect of wall, release location and diameter of the droplet on the internal and external velocity field of the droplet. Immiscible liquid-liquid flows are modeled in the laboratory frame of reference. The liquids are incompressible and flow is laminar, with constant fluid properties such as density, viscosity, and surface tension. There is no mass transfer between phases. The VOF method explained in Chapter 3 is used with the inclusion of gravitational force in momentum conservation equation. The conservation equations are written as:

Conservation of mass:

$$\frac{\partial \rho}{\partial t} + \nabla.(\rho \mathbf{v}) = 0 \tag{5.1}$$

Conservation of Momentum:

$$\frac{\partial \rho \mathbf{v}}{\partial t} + \nabla.(\rho \mathbf{v}\mathbf{v}) = -\nabla P + \nabla.(\mu \nabla \mathbf{v}) + \mathbf{F}_{SV} + \rho \boldsymbol{g} \tag{5.2}$$

5.2.1 Geometry and Mesh

Figure 5.1a shows the geometry and boundaries of the domain. No-slip boundary condition is applied at the wall and free slip, at the top. Free slip boundary condition establishes a specified velocity gradient (tangential component of the velocity field is non-zero) with zero normal velocity component. It ensures free surface flow at the top. Droplet of known diameter is patched in such a way that the droplet is at 2.5 mm below from the top surface. Height of the channel is 60 mm (sufficient for the droplets to achieve terminal velocity way before reaching to the bottom) and width of the channel is 15 mm. These dimensions are same as the experimental setup used in the experiments (discussed in Chapter 4). Figure 5.1b shows a part of mesh used for the simulations. Two-dimensional square meshing is done for the simulation domain resulting in 9×10^5 number of elements. The naming convention is used for the release location of the droplet in such a way that center, mid , and wall represents, d = 7.5 mm , 5 mm, and 2.5 mm respectively.

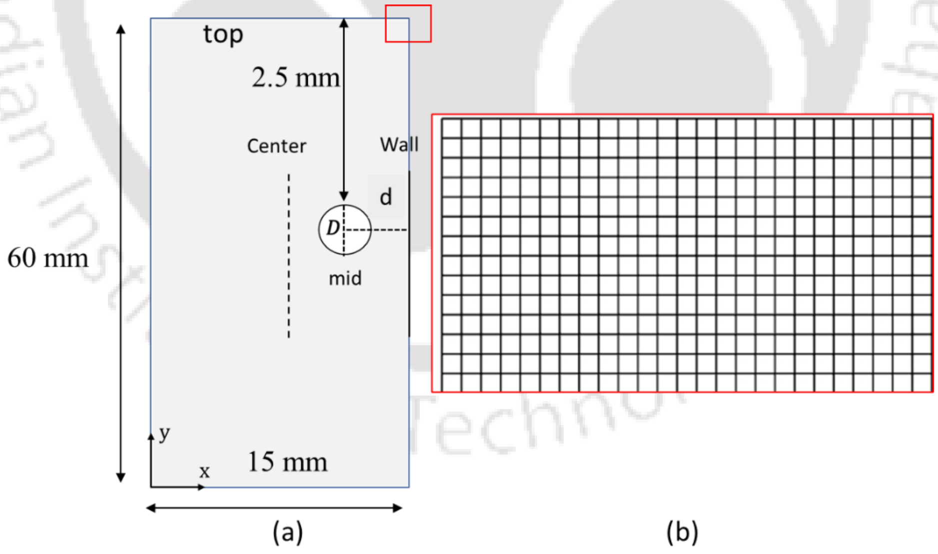

Figure 5.1 (a) Geometry used for the numerical investigation showing the wall (d = 2.5 mm), mid (d = 5 mm) and center (d = 7.5 mm) position and (b) Image of a small part of square mesh elements used for meshing of the domain. The red color rectangle shows the region of the represented mesh.

5.2.2 Numerical Scheme

These governing equations are also solved using the ANSYS Fluent 19.2. The pressure–velocity coupling is solved using PISO (Pressure-Implicit with Splitting of Operators) scheme. Spatial discretization is done by using Grean-Gauss Node Based technique. The pressure at the interface between neighboring cells is calculated using the Body Force Weighted scheme, and the momentum equation is discretized using a second-order upwind method. The discretization of the unsteady term is done using an implicit first-order approach. The time step size is kept variable between 10^{-5}–10^{-8} keeping global courant number constant at 0.25 for transient simulations. The absolute convergence criterion is set to be 10^{-4} for each parameter.

5.3 Results and Discussion

Investigation of internal circulations inside a falling droplet moving under the effect of gravity in liquid media is done by varying different parameters such as droplet diameter (D), release position (d), and viscosity ratio of the droplet to surrounding liquid (λ). 2D simulations are performed and velocity field is obtained for different parameters.

Table 5.1 shows the number of cases run for different parameters; diameter (D), release location (d) and viscosity ratio (λ). Terminal velocity is measured and Capillary number (Ca) and Reynolds number (Re) are derived for all the cases as shown in Table 5.1. Increasing viscosity ratio at constant diameter and release location and diameter show that terminal velocity increases for all the cases. Similarly, increasing the diameter result in increase in the terminal velocity a any constant viscosity ratio as shown in Figure 5.2. Further, increasing viscosity ratio at constant diameter at any release location, increases the terminal velocity. However, experimentally observed value of terminal velocities for the droplets released from the center (Figure 4.4) are one order of magnitude smaller than those obtained by CFD simulation.

Table 5.1 Different parameters studied for falling droplet inside liquid medium under gravity

D (mm)	(d)	(λ)	U_t (mm/s)	Ca	Re
3	7.5	0.09	3.6	0.053	0.03
3	7.5	0.36	12.6	0.049	0.46
3	7.5	1.79	43	0.033	8.01
4	7.5	0.09	4.8	0.071	0.06
4	7.5	0.36	16.6	0.065	0.79
4	7.5	1.79	52	0.040	12.91
4	5	0.09	5.2	0.077	0.07
4	5	0.36	16.7	0.065	0.80
4	5	1.79	52	0.040	12.92
4	2.5	0.09	5.4	0.080	0.07
4	2.5	0.36	18.9	0.074	0.91
4	2.5	1.79	52	0.040	12.92
5	7.5	0.09	5.7	0.085	0.09
5	7.5	0.36	19.2	0.075	1.16
5	7.5	1.79	54.3	0.041	16.86

Figure 5.2b show that the release location of the droplet also affects its terminal velocity. Terminal velocity of the $\lambda = 1.79$ case is always higher at any location but the droplets released near wall observed to possess slightly larger value than those released away from the wall (mid and center locations). This result indicates different velocity field inside the droplet released closer to wall.

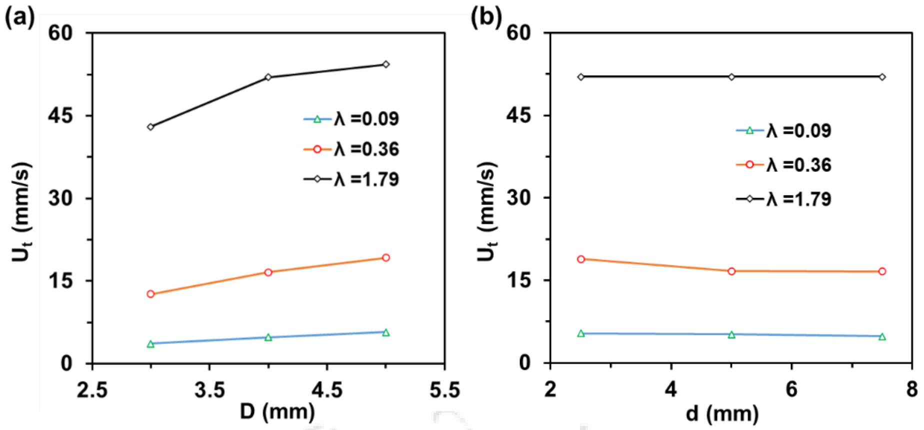

Figure 5.2 (a) Terminal velocity (U_t) variation with viscosity ratio (λ) of the droplet liquid to outer liquid and (b) Terminal velocity (U_t) variation with release location (d).

To compare the CFD result with experiments, normalized terminal velocity is shown in Figure 5.3 with normalized diameter (D/L*). U* represents the corresponding velocity calculated by Hadamard (1911) and Rybczynski (1911), and L* represents the channel width (15 mm). However, it shows that the terminal velocity obtained by CFD is greater than those measured during the experiment. Even though there is an order of magnitude difference between experimental and CFD data but matches qualitatively.

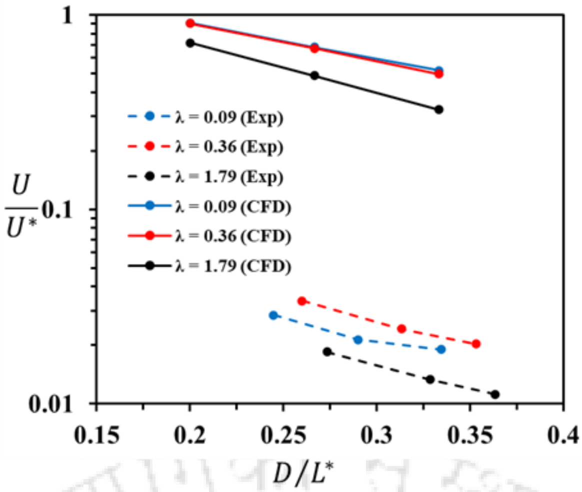

Figure 5.3 Variation of normalized terminal velocity with diameter (D/L*) and comparison with experimentally measured data

5.3.1 Effect of Diameter

Different-sized droplets in Figure 5.4, released at the center of the channel, show two counter-rotating vortices symmetric to a vertical line passing from the droplet center. The vortices are shown in the droplets for λ = 0.09. Each vortex occupies half of the circle. However, there is no shape deformation observed in this case. As shown in Table 5.1, Ca increases greatly (0.053-0.085) with an increase in diameter at constant viscosity ratio (λ = 0.09) for the droplets released from the center (d = 7.5 mm). Therefore, the highest local velocity magnitude is observed mostly near the interface due to dominating viscous force with the increasing diameter. Location of the vortex center fall on the middle position of the center of the droplets showing symmetric behavior about horizontal line passing through middle of the droplet. Vortices shown in the Figure 5.4 indicate that the maximum local velocity is near the interface far away from the central line and almost equal to terminal velocity of the droplets.

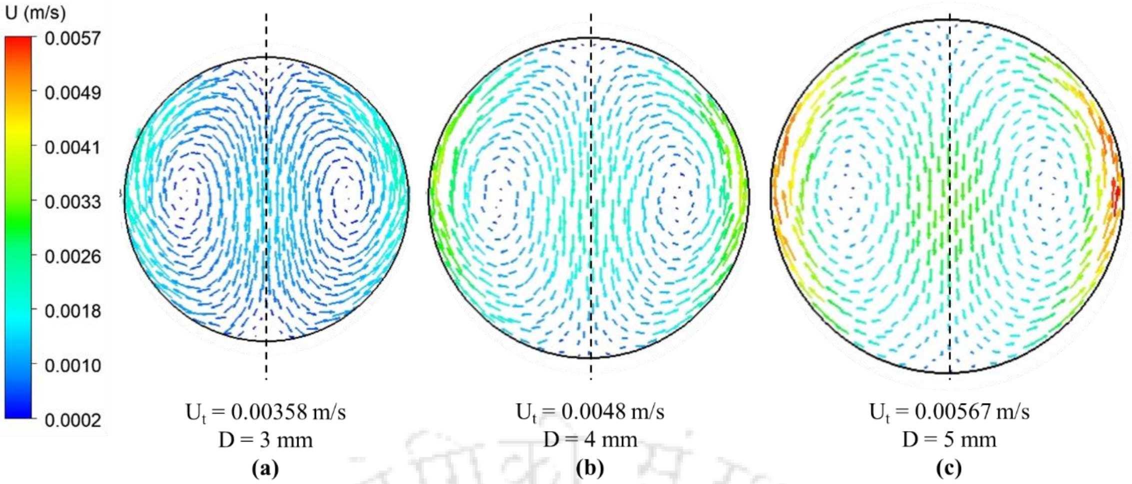

Figure 5.4 Velocity field inside droplets ($\lambda = 0.09$) of different diameters (a) 3 mm, (b) 4 mm, and (c) 5 mm, released from the center position.

An increase in the viscosity ratio ($\lambda = 0.36$, in Figure 5.5), shows similar behavior in terms of symmetric internal circulation of the droplet. It also does not result in shape deformation of the droplet. However, the terminal velocity of each droplet increased substantially (by a factor of ~3.5) with an increase in viscosity ratio (λ). Vortices are observed to be symmetric about horizontal as well as vertical line passing through the middle of the droplet. The center of the vortex falls on the horizontal line passing through the middle of the droplet as well. Increase in Ca value (0.049-0.075) is lesser for this case than $\lambda = 0.09$ case because of the decrease in the value of viscosity of surrounding liquid and increased value of terminal velocity. The local velocity magnitude is still highest at the interface far away from the vertical line passing through the center. It is also to note that the maximum local velocity magnitude is also increased with the increase in the value of viscosity ratio (λ).

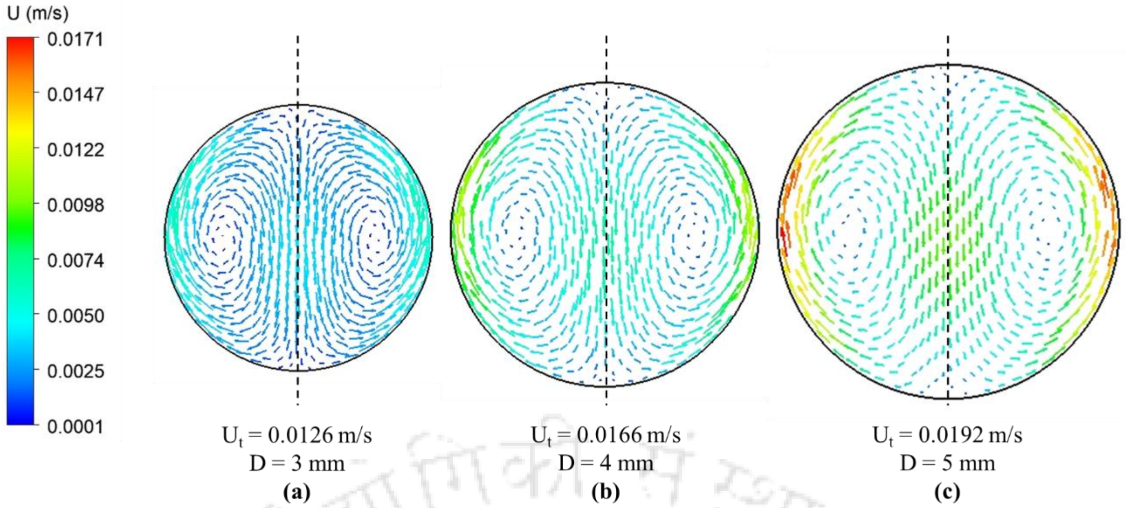

Figure 5.5 Velocity field inside droplets ($\lambda = 0.36$) of different diameters (a) 3 mm, (b) 4 mm, and (c) 5 mm, released from the center position.

The effect of droplet diameter upon a further increase in the viscosity ratio ($\lambda = 1.79$) for the droplets released at the center position of the channel from the wall is shown in Figure 5.6. Two counter-rotating symmetric vortices with respect to the vertical line passing from the center of the droplet are observed. Unlike previous cases ($\lambda = 0.09$ and 0.36) vortices are observed to occupy half area inside the droplet only for D = 3 mm and start to deviate for the case of D = 4 mm and 5 mm (Figure 5.6b and c). the center of these symmetric vortices observed to be shifting towards interface away from the vertical line. The increase in the value of Ca (0.033-0.41) is not significant like previous cases and due to which the maximum local velocity magnitude is observed at the center of the droplets. However, the magnitude of local velocity increases with increasing the diameter. The position of center of the vortex is changed due to the change in the shape of the droplets. Shape deformation is observed in the droplets with the increase in the initial droplet diameter.

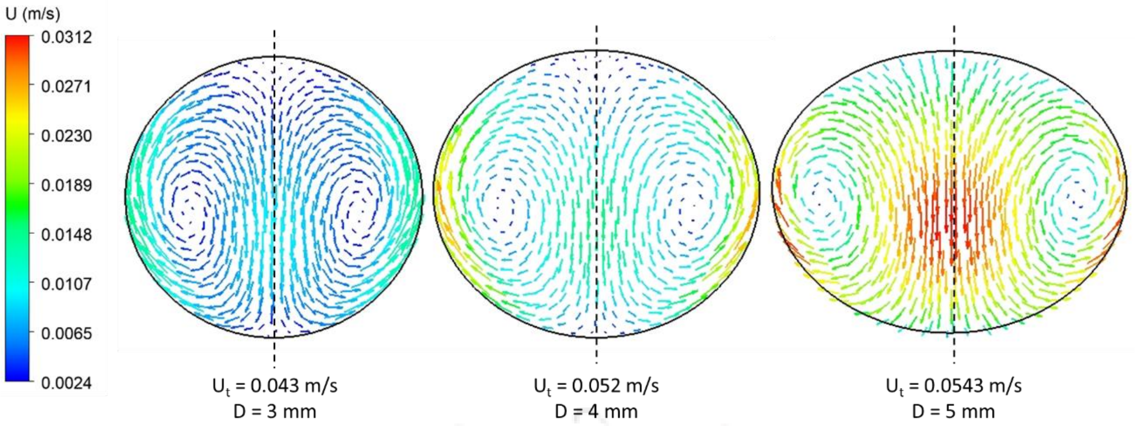

(a) (b) (c)

Figure 5.6 Velocity field inside droplets (λ = 1.79) of different diameters (a) 3 mm, (b) 4 mm, and (c) 5 mm, released from the center position.

5.3.2 Effect of Viscosity Ratio

Figure 5.7 shows the effect of different viscosity ratios (a) λ = 0.09, (b) λ = 0.36, and (c) λ = 1.79) on the internal vortices for the droplet of 4 mm diameter released at the center of the channel from the wall. Increasing the viscosity ratio results in shape deformation and, in turn, a change in the position of the center of the symmetric vortices. In the case of (a) λ = 0.09, vortices are symmetric to the vertical line and located at the center of the droplet. With the increase in the value of λ, the vortices shift towards bottom half of the droplet while remaining symmetric to vertical line. A decrease in the value of Ca (0.71-0.40) is observed with an increase in λ which indicates a decrease in the magnitude of viscous force to surface tension force. This increase in surface tension force is suspected to be the reason for shape deformation. The local velocity is also observed to be increasing with the increase in the value of λ. However, maximum local velocity is always at the interface far away from the vertical line passing through the middle. Terminal velocity is observed to be continuously increasing with an increase in the value of release location (λ).

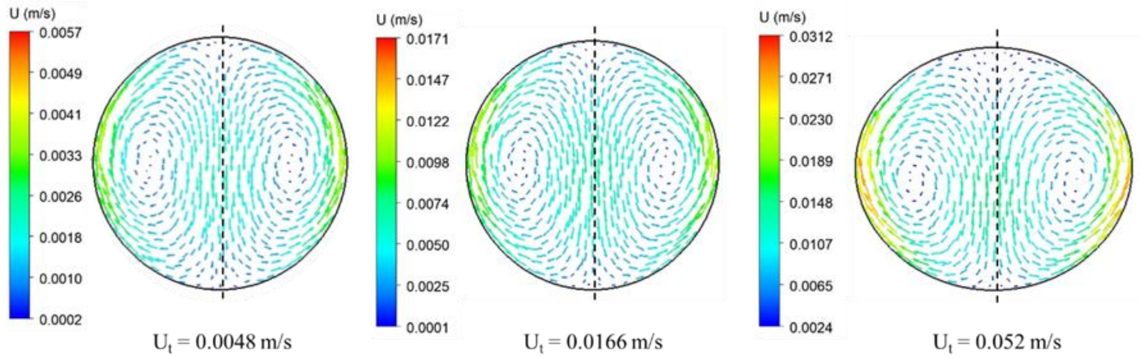

$U_t = 0.0048$ m/s
$\mu = 0.371$ Pa.s
(a)

$U_t = 0.0166$ m/s
$\mu = 0.098$ Pa.s
(b)

$U_t = 0.052$ m/s
$\mu = 0.019$ Pa.s
(c)

Figure 5.7 Velocity field inside droplets (D = 4 mm) for different viscosity ratios (a) $\lambda = 0.09$, (b) $\lambda = 0.36$, and (c) $\lambda = 1.79$, released from the center position (d = 7.5 mm).

The effect of different viscosity ratios on a 4 mm-sized droplet released at the mid-position (d = 5.0 mm) of the channel center and the wall is shown in Figure 5.8. The droplets released at d = 5.0 mm show counter-rotating vortices but the vortices are not completely symmetric. The asymmetry in the vortices can be clearly seen at the lowest viscosity ratio. Vortices are positioned at the bottom half of the droplet in the case of (c) $\lambda = 1.79$ due to the deformation in the shape of the droplet. The terminal velocity is observed to be increasing with an increase in the value of λ at the mid location as well. The local velocity magnitude is also increasing with increasing value of λ and it is measured to be larger than that observed for droplet released at center (d = 7.5 mm). the value of Ca (0.077-0.04) is again observed to be decreasing.

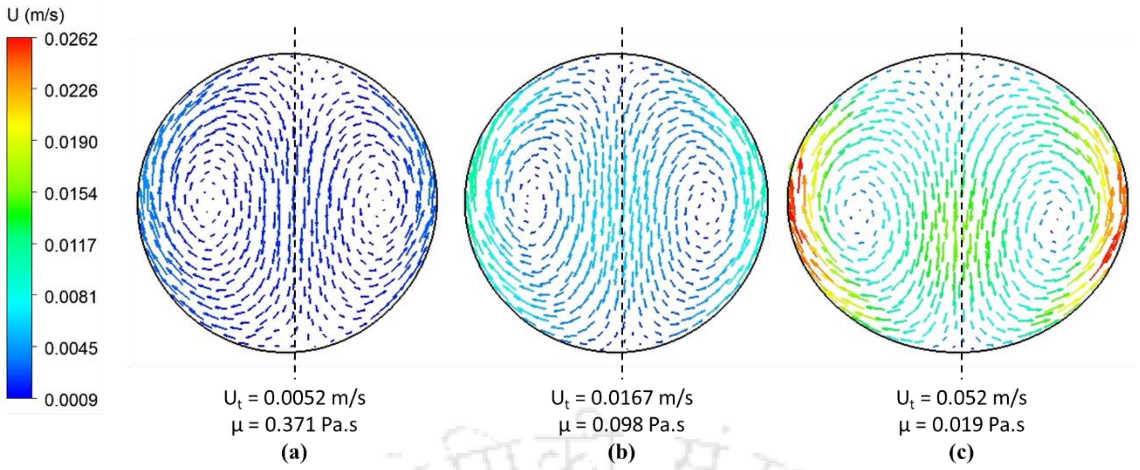

Figure 5.8 Velocity field inside droplets (D = 4 mm) of different viscosity (a) λ = 0.09, (b) λ = 0.36, and (c) λ = 1.79, released from the mid position (d = 5 mm).

Figure 5.9 show the velocity field inside the 4 mm droplets of different viscosity ratios (a) λ = 0.09, (b) λ = 0.36, and (c) λ = 1.79 released near the wall of the channel (d = 2.5 mm). Presence of the wall influence the vortex which is nearer to the wall. The asymmetry between the two vortices is clearly visible. However, with the increase in the viscosity ratio, asymmetry decreases and the shape deformation of the droplet increases.

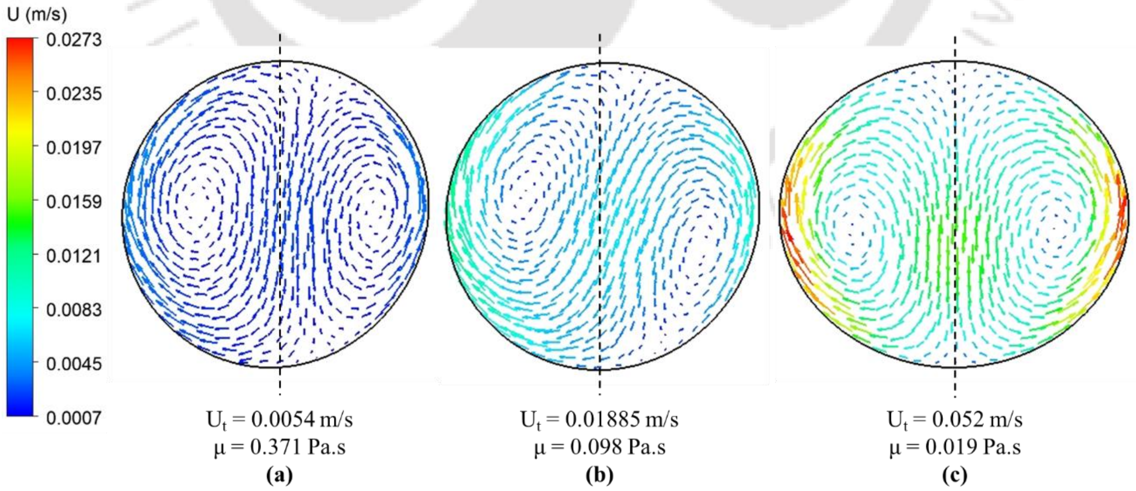

Figure 5.9 Velocity field inside droplets (D = 4 mm) of different viscosity (a) λ = 0.09, (b) λ = 0.36, and (c) λ = 1.79, released from the near wall position (d = 2.5 mm).

The introduction of asymmetry inside the droplet vortices is observed with the increase in the viscosity ratio as well as the presence of the wall.

5.3.3 Effect of Release Position

Behavior of internal vortices inside a 4 mm droplet for λ = 0.09, released at different distances from the wall is shown in Figure 5.10. It is observed that as droplet release position moves towards the wall the vortices become asymmetric. A small shape deformation is also observed for the case when droplet is released from near wall location (d = 2.5 mm). The shape deformation of the droplet introduces the change in the orientation of the vortices around the vertical line. The terminal velocity of these droplets increases with the release location shifts towards wall. There is no significant change in the value of Ca is observed as given in Table 5.1.

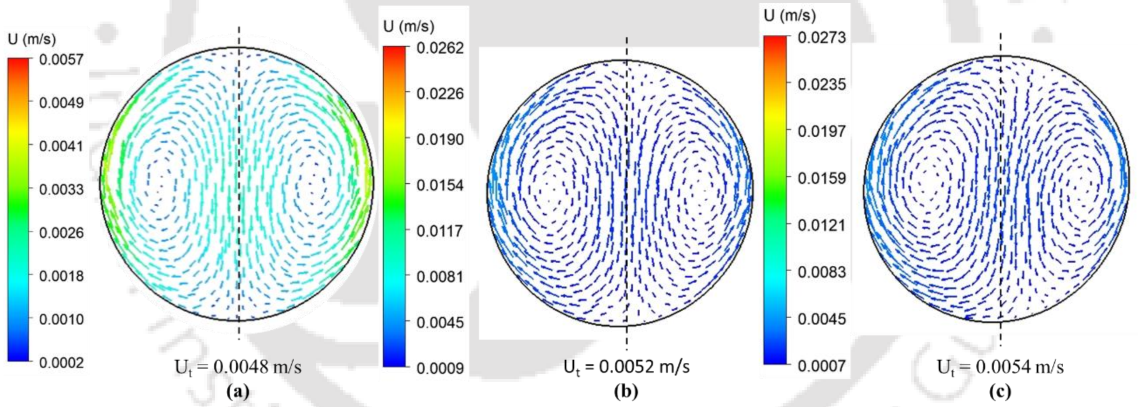

(a) (b) (c)

Figure 5.10 Velocity field inside droplets (D = 4 mm) released from different position (a) Center (d = 7.5 mm), (b) Mid (d = 5.0 mm), and (c) near the wall (d = 2.5 mm), released from the wall for λ = 0.09.

5.3.4 Time Evolution of Recirculations

It is concluded from the above results that the droplet released near the wall for the case of λ = 1.79 can have the highest asymmetry due to the greater shape deformation because of the presence of the wall. Figure 5.11 shows the time evolution of the vortices inside a 4 mm droplet for the case of λ = 1.79. It is observed that location of the vortices changes with time. It is evident that the droplets released near the wall have the highest asymmetry in terms of internal circulation. The terminal velocity of the droplet in this case is 52.0 mm/s constant through out the fall of the droplet.

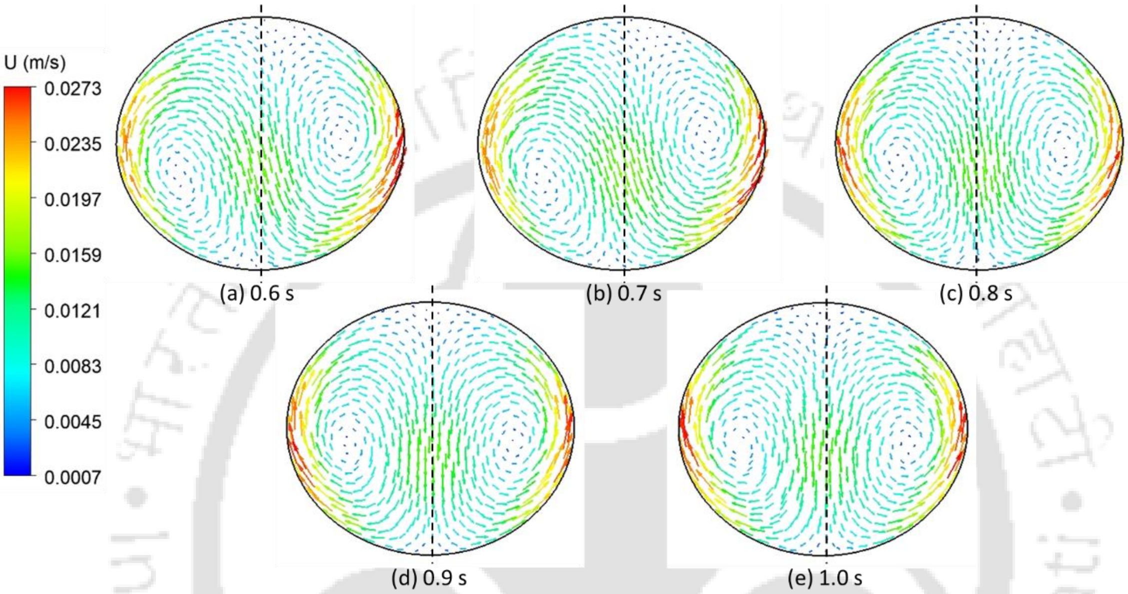

Figure 5.11 Vortex movement inside the (4 mm, λ = 1.79) droplet released near the wall.

5.3.5 Coalescence

Similar to experiments performed and discussed in Chapter 4, the phenomena of coalescence is investigated in this section. The stages of coalescence, neck growth and internal velocity field is important to understand. A 3 mm sized droplet coalescing with a droplet of the size of 4 mm inside liquid media of viscosity ratio λ = 0.09 under the effect of gravity is shown in Figure 5.12. Similar to experimental observation shown in section 4.3.3, numerical simulation also shows different stages of coalescence. Due to higher terminal velocity of 4 mm droplet released after the 3 mm droplet, coalescence occurs.

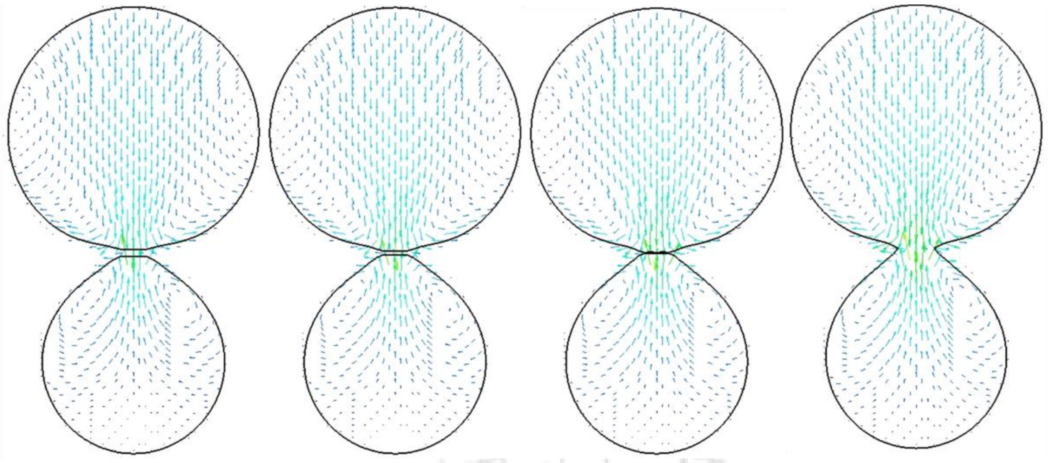

(a) t = 6.06596 s (b) t = 6.06796 s (c) t = 6.06996 s (d) t = 6.07196 s

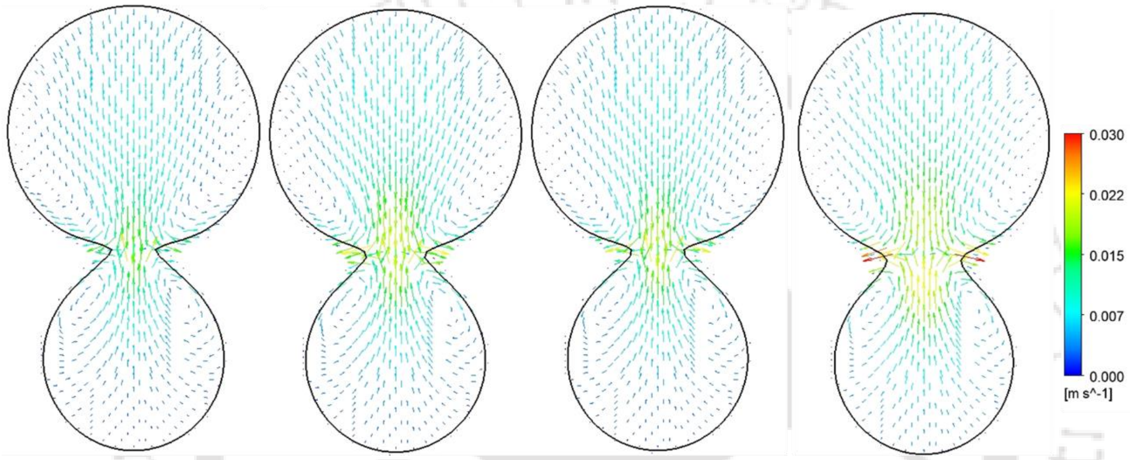

(e) t = 6.07396 s (f) t = 6.07596 s (g) t = 6.07796 s (h) t = 6.07996 s

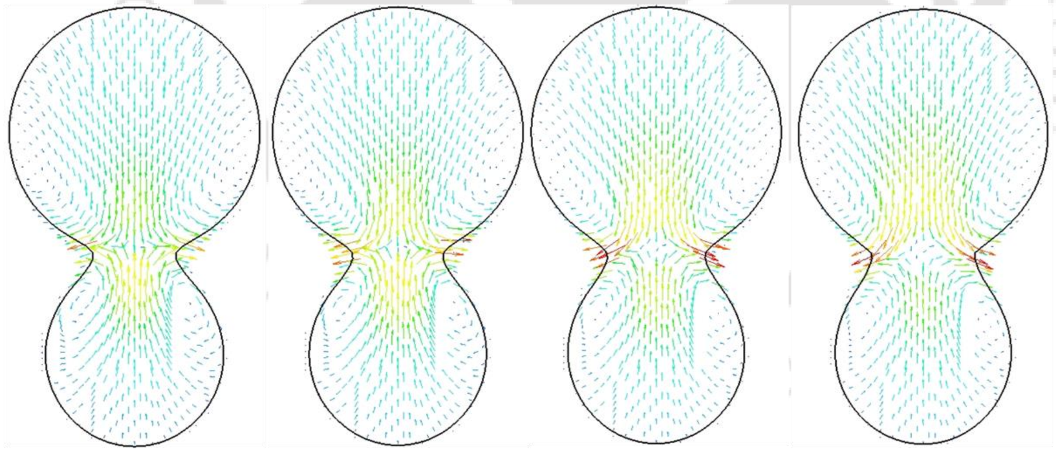

(i) t = 6.07396 s (j) t = 6.07596 s (k) t = 6.07796 s (l) t = 6.07996 s

Figure 5.12 Time evolution of the coalescence of two droplets of different diameters (3 mm, and 4 mm) falling under the effect of gravity inside liquid media of viscosity ratio (λ) = 0.09.

Bigger droplet approaches smaller drop the interfaces of both the droplets deform. The outer liquid present between the approaching droplets moves outwards due to which pressure drops which leads to the deformation of the coalescing interfaces. As the distance between them decreases (Figure 5.12 a-b) four small vortices appear near coalescing interfaces which starts to grow after the film rupture (Figure 5.12 c-l). the mechanism of interface rupture and neck growth is same as observed experimentally (section 4.3.3).

Figure 5.13 shows the growth of non-dimensional neck radius (r/R) with non-dimensional time $t/t_{out.}$ The parameters t_{out} is defined as same as discussed in section 4.3.3 of chapter 4. The growth of neck radius during coalescence of 2D droplets is shown to be similar to as described in literature (Brik et al., 2021; Paulsen, 2013). However, the condition of the current study is different than those studied in literature, the trend of the initial growth is observed to be similar.

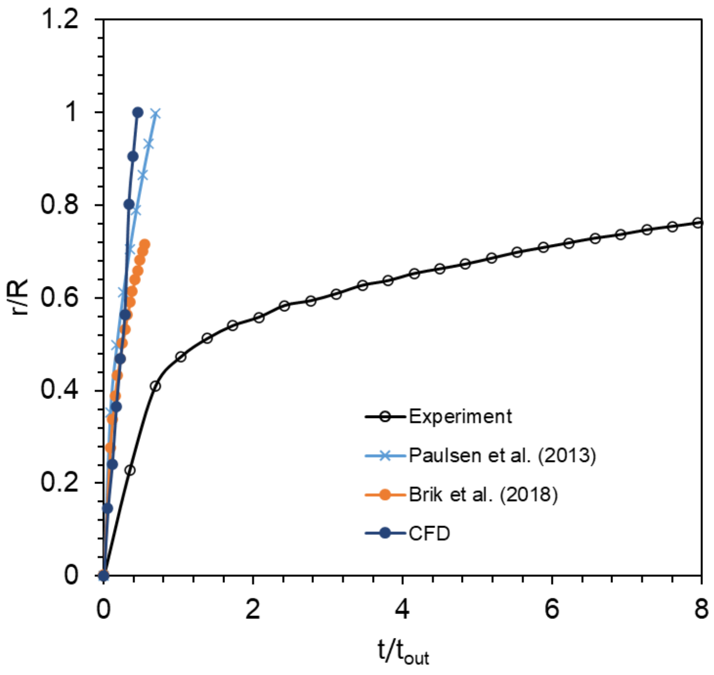

Figure 5.13 Evolution of neck radius (r/R) with dimensionless time t_{out} during the coalescence of 4 mm and 3 mm droplets.

5.3.6 Comparison with the Experiments

Although simulations are performed for same conditions as used in the experimental investigations, there are some similarities and few differences observed when results are compared. Similar to experimental observations, terminal velocity increases with an increase in viscosity ratio with CFD simulations. Internal vortices are symmetric when released from the center for all the cases observed in the experiments as well as CFD simulations. Similarly, introduction of asymmetry with change in the release location towards wall is also observed in CFD as well as experiments. An increase in the terminal velocity with increasing diameter at any location is also observed in both CFD as well as experiments. The stages of coalescence phenomena are also successfully captured by CFD and compare well with the experimental results.

Apart from qualitative match with experimental results CFD results are limited with quantitative data. Experiments show that vortices are mostly at the bottom part of the droplet while CFD show that vortices cover almost half of the droplet area. This difference in the size of the vortices can be attributed to 2D simulations. Full three-dimensional CFD simulation might be able to capture the exact velocity field with respect to experimental data.

5.4 Summary

Two-dimensional numerical simulations were performed to investigate the behavior of internal circulation inside a droplet falling under the effect of gravity in another immiscible liquid medium. The effect of droplet diameter, release distance from the wall, and viscosity ratio of the droplet to surrounding liquid was studied. It was observed that two counter-rotating symmetric vortices appear inside the droplet for all the viscosity ratios when released from the center of the channel. These vortices became asymmetric when the release position was shifted towards the wall. An increase in the droplet diameter only resulted in an increased size of counter-rotating symmetric vortices. An increase in viscosity ratio led to the deformation of the droplets. The asymmetry in the internal circulation of the droplets near the wall was observed to be a combined effect of the wall and increased viscosity ratios.

Further, the coalescing phenomena in the domain were also studied by releasing two unequal-sized droplets, one after another. Four counter-rotating vortices appeared near the neck region, which grew with the growth of the neck. Similar to experimental observations, 2D CFD results were able to show the qualitative behavior of the internal flow field. The increasing trend of terminal velocity with an increase in diameter and asymmetric behavior of internal vortices with a change in release location was successfully captured by CFD simulations. However, 2D CFD results were not able to capture the vortex flow field quantitatively. The difference between internal vortices was attributed to the 2D nature of the CFD simulation.

Chapter 6. Conclusions & Scope for Future Work

The research work discussed in this thesis provides a better understanding of the flow physics involved in two-phase flow in confined channels. The thesis addresses two fundamental problems commonly encountered in the engineering design of process equipment. In the first problem, hydrodynamics in different flow regimes, namely slug, slug-annular, and annular flow in gas-liquid flow in the curved section of a circular channel of 1 mm diameter, was explored experimentally and numerically. In the second problem, flow behavior in a droplet falling under the effect of gravity inside another liquid media was explored experimentally and numerically. The main findings of the thesis are summarized below.

6.1 Gas-Liquid Flow in a Curved Microchannel

- A flow regime map for gas-liquid flow in the curved microchannel was developed on superficial velocities of gas and liquid as the coordinate axis. Slug, Annular, and churn flow observed at U_{SL} = 0.01-0.2 m/s and U_{SG} = 2.34-30.44 m/s along with the slug-annular transition. It was similar to the flow regime map of straight microchannels developed in the past.
- There was a liquid film present between the gas phase and the wall in all cases. The thickness of the liquid film was symmetric upstream to the bend and asymmetric at the bend and downstream.
- In the slug flow at the bend, the film at the inner wall was thinner than the outer wall film while the outer film was thinner than the inner wall film in the annular flow regime. This change in film thickness occurred during the transition from slug to annular flow. The transition was caused by an increase in the inertial force of the liquid phase with the increase in the velocity.

Further, CFD simulations were performed, which provided new insights –

- Three-dimensional CFD simulations were done on one U-bend (length of the two straight sections = 10D each), and slug, slug-annular transition, and annular flow regimes were captured at U_{SL} = 0.21 m/s, and U_{SG} = 0.15-0.62 m/s. The geometry used in CFD simulations had the same diameter and curvature of the bend, and flow developed with time from the inlet, while in experiments, gas and liquid volumetric flow rates controlled the flow regimes, and all the 21 bends with straight sections were used.
- Bubble shape deformation observed at the bend in the slug flow regime due to the effect of the difference in centrifugal force at the outer and inner wall interfaces.
- The profile of the streamlined velocity component was observed to be symmetric in the straight channel and became asymmetric at the bend and skewed towards the outer wall.
- Secondary flow (Dean vortex) observed at the cross-section of the bend in the liquid phase during slug flow. Two Dean vortices occupy the cross-section area of the channel when only liquid slug was present and four vortices were observed when both phases were present during different flow regimes.
- Four counter-rotating Dean vortices were observed during the annular flow regime: two in the gas phase and two in the liquid phase.
- Average bubble velocity during Taylor flow increased in the upper bend due to centrifugal forces and decreased in the lower bend.
- Secondary flow in both phases confirmed the enhanced mixing due to the curvature effect.

CFD simulations confirmed the observations of experiments in terms of asymmetric liquid film thickness and provided additional information about shape, velocity field, and bubble velocity at the bend.

6.2 Droplet Falling in Liquid Media

The internal flow of droplets falling under the effect of gravity inside another immiscible liquid medium in a rectangular channel was studied using particle image velocimetry. The effect of release location and droplet diameter at a constant viscosity ratio (λ = 0.09) were used as parameters for this study. Silicon oil as surrounding liquid and glycerol water mixture for droplet liquid was used for the experiments.

- The terminal velocity of the droplet was observed to be increasing with an increase in the diameter and viscosity ratio.
- Internal motion within a droplet released at the channel center was symmetric, and two counter-rotating vortices were observed at the bottom half of the droplet.
- Change in release positions towards the wall led to asymmetric fluid motion and vortex distribution inside the droplet. The vortex away from the wall became larger than the vortex near the wall.
- Increasing the droplet size resulted in a larger size of the vortices due to increased tangential stress at the interface.
- The coalescence of two droplets was observed by releasing a smaller droplet followed by a bigger droplet at the channel center.
- The coalescence point grew to form a neck-like shape, which grew rapidly in the beginning and then slowed down with a wider shape.

- A pair of counter-rotating vortices were observed on each side of the neck. These vortices readjusted the fluid with a growing neck such that the droplet gains the shape of a single bigger droplet.

Two-dimensional numerical simulations were performed with the same parameters along with different viscosity ratios ($\lambda = 0.09, 0.36$, and 1.79) to observe the effect on the flow within the droplet falling under the effect of gravity inside another immiscible liquid media.

- Terminal velocity increased with increasing diameter and viscosity ratio similar to experimental results. Terminal velocity was observed to be increasing as the release position changed towards the wall.
- The Numerical study confirmed symmetric vortices inside droplets released at the center, becoming asymmetric when released near the channel wall, similar to experimental results.
- Similar to experimental observations, increased droplet diameter at the center, enlarged the size of the symmetric vortices.
- The symmetric vortices occupied the full area of the droplet, while the vortices were mostly at the bottom part of the droplet in experimental results. This difference in the position of the vortices could be attributed to 2D simulations.
- Deformation of the droplet shape observed with increased viscosity ratios. This deformation increased with increasing diameter as well as release position towards the wall.
- Asymmetric circulation inside droplet released near the wall attributed to channel wall influence and higher viscosity ratios.

- During the coalescence of unequal-sized droplets, four counter-rotating vortices at the neck region, intensifying with neck size observed with experiments as well as CFD simulation.
- Similar to experimental results, numerical simulation also showed four counter-rotating vortices present at the neck region. The size of these vortices grew with the growth of the neck as also observed in the experiments.

6.3 Scope for Future Work

While this thesis enhances understanding of gas-liquid flow regime behavior at U-bends and liquid-liquid flow in confined channels for engineering applications, several areas require further investigation. Some of the recommendations for future work are given below.

6.3.1 Gas-Liquid Flow in a Curved Microchannel

- This study has shown the effect of a U-bend with only one curvature. Investigation of flow regimes with variable channel curvature of bend can provide even more data for the better design of microreactor or micromixer with the bend.
- While this study is limited to varying viscosity as a parameter, surface tension, density, wall roughness, channel diameter, and cross-section shapes such as rectangular and triangular can be used for further studies.
- This study has shown the importance of liquid film at the bend. PIV study of liquid film region can be done to provide a better understanding of the flow physics at the bend which can be useful for the better design of such channels.
- The behavior of non-Newtonian fluids (gas-liquid and liquid-liquid) at the bend can be further studied for the application of curved microchannels incorporating non-newtonian fluids.

- Adding a bend, though, definitely enhances mixing, but for plant-level application, pressure drop measurement in two-phase flow can aid the design of microchannels with a bend.
- Numerical investigation using different flow profiles at the inlet (i.e. pulsatile flow) on a single Taylor bubble passing through curvature can be done.
- CFD simulation of channels, including different numbers of bends with different curvatures, can provide a better understanding of flow. However, these simulations can be very expensive but will be very useful for better design of plant-level applications.
- The effect of bend coated with catalyst on reaction kinetics is another area that can be explored.
- Application of microchannels with curved sections in dehydrogenation and decarbonization can be explored.

6.3.2 Moving Droplet Inside Liquid Media

- This study investigated recirculation inside a single droplet at a time released from a particular location to understand the behavior of the droplet as a single unit. Recirculations inside multiple droplets released at the same and different locations can provide a better understanding in terms of four-way coupling.
- The effect of the wall on the growth of the neck formed during the coalescence of the falling droplet inside immiscible liquid media can be explored.
- This study considered only Newtonian fluid, while non-Newtonian droplet dynamics can be explored further, for example, viscoelastic droplet dynamics.
- The problem of rising bubbles/droplets in another immiscible liquid media can be explored based on this work.

- The effect of change in the density ratio of the droplet and surrounding media can also provide a better understanding.

References

Abdel-Alim, A.H., Hamielec, A.E., 1975. A Theoretical and Experimental Investigation of the Effect of Internal Circulation on the Drag of Spherical Droplets Falling at Terminal Velocity in Liquid Media. Ind & Engg Chem Fund 14, 308–312. https://doi.org/10.1021/i160056a004

Akbar, M.K., Woodruff, G.W., Plummer, D.A., Ghiaasiaan, S.M., 2002. Gas-Liquid Two-Phase Flow Regimes in Microchannels, ASME International Mechanical Engineering Congress & Exposition.

Al-Asadi, M.T., Mohammed, H.A., Wilson, M.C.T., 2022. Heat Transfer Characteristics of Conventional Fluids and Nanofluids in Micro-Channels with Vortex Generators: A Review. Energies (Basel). https://doi.org/10.3390/en15031245

Al-Rawashdeh, M., Yu, F., Nijhuis, T.A., Rebrov, E. v., Hessel, V., Schouten, J.C., 2012. Numbered-up gas–liquid micro/milli channels reactor with modular flow distributor. Chemical Engineering Journal 207–208, 645–655. https://doi.org/10.1016/J.CEJ.2012.07.028

Aminizadeh, J., Moosavi, A., 2023. Microfluidic equivalents of three logical systems for controlling droplet generation: Set, reset, and set-reset latches. Sens Actuators A Phys 349, 114073. https://doi.org/10.1016/J.SNA.2022.114073

Aminzadeh, M., Maleki, A., Firoozabadi, B., Afshin, H., 2012. On the motion of Newtonian and non-Newtonian liquid drops. Scientia Iranica 19, 1265–1278. https://doi.org/10.1016/j.scient.2011.09.022

Angeli, P., Gavriilidis, A., 2008. Hydrodynamics of Taylor flow in small channels: A review. Proc Inst Mech Eng C J Mech Eng Sci 222, 737–751. https://doi.org/10.1243/09544062JMES776

Anthony, C.R., Kamat, P.M., Thete, S.S., Munro, J.P., Lister, J.R., Harris, M.T., Basaran, O.A., 2017. Scaling laws and dynamics of bubble coalescence. Phys Rev Fluids 2, 083601. https://doi.org/10.1103/PhysRevFluids.2.083601

Asadolahi, A.N., Gupta, R., Fletcher, D.F., Haynes, B.S., 2011. CFD approaches for the simulation of hydrodynamics and heat transfer in Taylor flow. Chem Eng Sci 66, 5575–5584. https://doi.org/10.1016/j.ces.2011.07.047

Ashwood, A.C., vanden Hogen, S.J., Rodarte, M.A., Kopplin, C.R., Rodríguez, D.J., Hurlburt, E.T., Shedd, T.A., 2015. A multiphase, micro-scale PIV measurement technique for liquid film velocity measurements in annular two-phase flow. International Journal of Multiphase Flow 68, 27–39. https://doi.org/10.1016/j.ijmultiphaseflow.2014.09.003

Assmann, N., Ladosz, A., Rudolf von Rohr, P., 2013. Continuous Micro Liquid-Liquid Extraction. Chem. Engg. and Tech. https://doi.org/10.1002/ceat.201200557

Aussillous, P., Quéré, D., 2000. Quick deposition of a fluid on the wall of a tube. Physics of Fluids 12, 2367. https://doi.org/10.1063/1.1289396

Ayyaswamy, P.S., S. S. Sadhal, 1983. Flow past a liquid drop with a large non-uniform radial velocity. J Fluid Mech 133, 65–81. https://doi.org/10.1017/S0022112083001792

Belmonte Andrew, Michael C. Sostarecz, 2003. Motion and shape of an axisymmetric viscoplastic drop slowly falling through a viscous fluid. Rheol Acta 497, 235–252. https://doi.org/10.1007/s00397-010-0478-1

Bezuidenhout, D., Reynolds, Q., Erwee, M., Oxtoby, O., 2020. High-speed video data for settling of dense liquid droplets through liquid media with different viscosities. Data Brief 33, 106428. https://doi.org/10.1016/j.dib.2020.106428

Bhosale, S.S., Acharya, A.R., 2020. Review On Applications of Micro Channel Heat Exchanger. International Research Journal of Engineering and Technology 7, 5326–5329.

Bird, E., Zhou, J., Liang, Z., 2020. Coalescence speed of two equal-sized nanobubbles. Phys. Fluids 32, 123304. https://doi.org/10.1063/5.0030406

Brackbill, J.U., Kothe, D.B., Zemach, C., 1992. A continuum method for modeling surface tension. J Comput Phys 100, 335–354. https://doi.org/10.1016/0021-9991(92)90240-Y

Bretherton, F.P., 1961. The motion of long bubbles in tubes. J Fluid Mech 10, 166. https://doi.org/10.1017/S0022112061000160

Brik, M., Harmand, S., Zaaroura, I., Saboni, A., 2021. Experimental and Numerical Study for the Coalescence Dynamics of Vertically Aligned Water Drops in Oil. Langmuir 37, 3139–3147. https://doi.org/10.1021/acs.langmuir.0c03624

Čejková, J., Banno, T., Hanczyc, M.M., Štěpánek, F., 2017. Droplets As Liquid Robots. Artif Life 23, 528–549. https://doi.org/10.1162/ARTL_a_00243

Charles, G.E., Mason, S.G., 1960. The mechanism of partial coalescence of liquid drops at liquid/liquid interfaces. J Colloid Sci 15, 105–122. https://doi.org/10.1016/0095-8522(60)90012-X

Chaurasiya, R.K., Singh, K.K., 2022. CFD modelling of mass transfer in liquid–liquid core-annular flow in a microchannel. Chem Eng Sci 249, 117295. https://doi.org/10.1016/J.CES.2021.117295

Chen, R., Yu, H.W., Zhu, L., Patil, R.M., Lee, T., 2017. Spatial and temporal scaling of unequal microbubble coalescence. A.I.Ch.E. Journal 63, 1441–1450. https://doi.org/10.1002/aic.15504

Chen, R.H., Tian, W.X., Su, G.H., Qiu, S.Z., Ishiwatari, Y., Oka, Y., 2011. Numerical investigation on coalescence of bubble pairs rising in a stagnant liquid. Chem Eng Sci 66, 5055–5063. https://doi.org/10.1016/j.ces.2011.06.058

Chinnov, E.A., Ron'shin, F. V, Kabov, O.A., 2015. Regimes of two-phase flow in micro-and minichannels (review) *.

Chung, P.M.Y., Kawaji, M., 2004. The effect of channel diameter on adiabatic two-phase flow characteristics in microchannels. International Journal of Multiphase Flow 30, 735–761. https://doi.org/10.1016/J.IJMULTIPHASEFLOW.2004.05.002

Clift, R. C., Grace, B. J., and Weber, M.E., 1999. Bubbles, Drops, and Particles, Journal of Fluid Mechanics. Dover Publications. https://doi.org/10.1017/S0022112079221290

Colin, C., Fabre, J., McQuillen, J., 1996. Bubble and slug flow at microgravity conditions: state of knowledge and open questions. Chem Eng Commun 141–142, 155–173. https://doi.org/10.1080/00986449608936414

Dean, W.R., 1927. XVI. Note on the motion of fluid in a curved pipe . The London, Edinburgh, and Dublin Philosophical Magazine and Journal of Science 4, 208–223. https://doi.org/10.1080/14786440708564324

Deng, N.N., Sun, J., Wang, W., Ju, X.J., Xie, R., Chu, L.Y., 2014. Wetting-induced coalescence of nanoliter drops as microreactors in microfluidics. ACS Appl Mater Interfaces 6, 3817–3821. https://doi.org/10.1021/am500563z

Dessimoz, A.L., Cavin, L., Renken, A., Kiwi-Minsker, L., 2008. Liquid-liquid two-phase flow patterns and mass transfer characteristics in rectangular glass microreactors. Chem Eng Sci 63, 4035–4044. https://doi.org/10.1016/j.ces.2008.05.005

Eggers, J., Lister, J.R., Stone, H.A., 1999. Coalescence of liquid drops. J Fluid Mech 401, 293–310. https://doi.org/10.1017/S002211209900662X

Eiswirth, R.T., Bart, H.J., Ganguli, A.A., Kenig, E.Y., 2012. Experimental and numerical investigation of binary coalescence: Liquid bridge building and internal flow fields. Physics of Fluids 24, 062108. https://doi.org/10.1063/1.4729791

Etminan, A., Muzychka, Y.S., Pope, K., 2021. Liquid film thickness of two-phase slug flows in capillary microchannels: A review paper. Can J Chem Eng 100, 325–348. https://doi.org/10.1002/cjce.24068

F. H. Garner and P. J. Haycock, 1959. Circulation in liquid drops. Chem Eng Sci 6, 457–475. https://doi.org/10.1016/0009-2509(56)80012-2

Fernández-Maza, C., Fallanza, M., Gómez-Coma, L., Ortiz, I., 2022. Performance of continuous-flow micro-reactors with curved geometries. Experimental and numerical analysis. Chemical Engineering Journal 437, 135192. https://doi.org/10.1016/J.CEJ.2022.135192

Fries, D.M., Waelchli, S., Rudolf von Rohr, P., 2008. Gas-liquid two-phase flow in meandering microchannels. Chemical Engineering Journal 135, 37–45. https://doi.org/10.1016/j.cej.2007.07.052

Gaikwad, S.M., Jolhe, P.D., Bhanvase, B.A., Kulkarni, A., Patil, V.S., Pimplapure, M.S., Suranani, S., Potoroko, I., Sonawane, S.H., Sonawane, S.S., 2017. Process intensification for continuous synthesis of performic acid using Corning advanced-flow reactors. Green Processing and Synthesis 6, 62–73. https://doi.org/10.1515/gps-2016-0147

Garner, F.H., Skelland, A.H.P., 1955. Some factors affecting droplet behaviour in liquid-liquid systems. Chem Eng Sci 4, 149–158. https://doi.org/10.1016/0009-2509(55)85017-8

Garner, F.H., Skelland, A.H.P., Haycock, P.J., 1954. Speed of circulation in droplets. Nature. https://doi.org/10.1038/1731239a0

Ge, L., Peng, Z., Moreno-Atanasio, R., Doroodchi, E., Evans, G.M., 2020. Three-Dimensional VOF-DEM Model for Simulating Particle Dynamics in the Liquid Slugs of a Vertical Gas-Liquid-Solid Taylor Flow Microreactor. Ind Eng Chem Res 59, 7965–7981. https://doi.org/10.1021/acs.iecr.0c00108

Govindarajan, R., Sahu, K.C., 2013. Instabilities in Viscosity-Stratified Flow. Annual Review of Fluid Mechanics 46, 331–353. https://doi.org/10.1146/annurev-fluid-010313-141351

Günther, A., Jensen, K.F., 2006. Multiphase microfluidics: From flow characteristics to chemical and materials synthesis. Lab Chip 6, 1487–1503. https://doi.org/10.1039/b609851g

Günther, A., Khan, S.A., Thalmann, M., Trachsel, F., Jensen, K.F., 2004. Transport and reaction in microscale segmented gas-liquid flow. Lab Chip 4, 278–286. https://doi.org/10.1039/b403982c

Guo, M., Hu, X., Yang, F., Jiao, S., Wang, Y., Zhao, H., Luo, G., Yu, H., 2019. Mixing Performance and Application of a Three-Dimensional Serpentine Microchannel Reactor with a Periodic Vortex-Inducing Structure. Ind. Eng. Chem. Res. 58, 13357–13365. https://doi.org/10.1021/acs.iecr.9b01573

Guo, Z., Fletcher, D.F., Haynes, B.S., 2016. Numerical simulation of annular flow hydrodynamics in microchannels. Comput Fluids 133, 90–102. https://doi.org/10.1016/j.compfluid.2016.04.017

Gupta, R., Fletcher, D., Haynes, B., 2010. Taylor flow in microchannels: A review of experimental and computational work. Journal of Computational Multiphase Flows 2, 1–31. https://doi.org/10.1260/1757-482X.2.1.1

Gupta, R., Fletcher, D.F., Haynes, B.S., 2009. On the CFD modelling of Taylor flow in microchannels. Chem Eng Sci 64, 2941–2950. https://doi.org/10.1016/j.ces.2009.03.018

Gupta, R., Turangan, C.K., Manica, R., 2016. Oil-water core-annular flow in vertical pipes: A CFD study. Can J Chem Eng 94, 980–987. https://doi.org/https://doi.org/10.1002/cjce.22451

Haase, S., Murzin, D.Y., Salmi, T., 2016. Review on hydrodynamics and mass transfer in minichannel wall reactors with gas–liquid Taylor flow. Chemical Engineering Research and Design 113, 304–329. https://doi.org/10.1016/j.cherd.2016.06.017

Hadamard, J.M., 1911. Mouvement permanent lent d’une sphère liquide et visqueuse dans un liquide visqueux. Comptes rendus hebdomadaires des séances de l ’ Académie des sciences, Série B 152, 1735–1738.

Han, Y., Kanno, H., Ahn, Y.J., Shikazono, N., 2015. Measurement of liquid film thickness in micro tube annular flow. International Journal of Multiphase Flow 73, 264–274. https://doi.org/10.1016/j.ijmultiphaseflow.2015.03.016

Han, Y., Shikazono, N., 2009. Measurement of liquid film thickness in micro square channel. International Journal of Multiphase Flow 35, 896–903. https://doi.org/10.1016/j.ijmultiphaseflow.2009.06.006

Hasan, N., Zakaria, Z. binti, 2011. Computational approach for a pair of bubble coalescence process. Int J Heat Fluid Flow 32, 755–761. https://doi.org/10.1016/j.ijheatfluidflow.2011.02.004

Hassan, I., Vaillancourt, M., Pehlivan, K., 2005a. Two-phase flow regime transitions in microchannels: A comparative experimental study. Microscale Thermophysical Engineering 9, 165–182. https://doi.org/10.1080/10893950590945049

Hassan, I., Vaillancourt, M., Pehlivan, K., 2005b. Two-phase flow regime transitions in microchannels: A comparative experimental study. Microscale Thermophysical Engineering 9, 165–182. https://doi.org/10.1080/10893950590945049

Hirt, C.W., Nichols, B.D., 1981. Volume of fluid (VOF) method for the dynamics of free boundaries. J Comput Phys 39, 201–225. https://doi.org/10.1016/0021-9991(81)90145-5

Hu, S., Kinter, R.C., 1955. The fall of single liquid drops through water. A.I.Ch.E. Journal 1, 42–48. https://doi.org/10.1002/aic.690010106

Huang, D., Wang, J., Che, J., Wen, B., Kong, W., 2023. Ultrasound-responsive microparticles from droplet microfluidics. Biomedical Technology 1, 1–9. https://doi.org/10.1016/J.BMT.2022.10.001

Hudson, S.D., 2010. Poiseuille flow and drop circulation in microchannels. Rheol Acta 49, 237–243. https://doi.org/10.1007/s00397-009-0394-4

Jayawardena, S.S., Balakotaiah, V., Witte, L.C., 1997. Flow Pattern Transition Maps for Microgravity Two-Phase Flows. Aiche Journal 43, 1637–1640. https://doi.org/10.1002/aic.690430627

Joanicot, M., Ajdari, A., 2005. Droplet control for microfluidics. Science (1979) 309, 887–888. https://doi.org/10.1126/science.1112615

Kakac, S., Bon, B., 2008. A Review of two-phase flow dynamic instabilities in tube boiling systems. Int J Heat Mass Transf 51, 399–433. https://doi.org/10.1016/j.ijheatmasstransfer.2007.09.026

Kawahara, A., Chung, P.Y., Kawaji, M., 2002. Investigation of two-phase flow pattern, void fraction and pressure drop in a microchannel. International Journal of Multiphase Flow 28, 1411–1435. https://doi.org/10.1016/S0301-9322(02)00037-X

Kawahara, A., Sadatomi, M., Nei, K., Matsuo, H., 2009. Experimental study on bubble velocity, void fraction and pressure drop for gas-liquid two-phase flow in a circular microchannel. Int J Heat Fluid Flow 30, 831–841. https://doi.org/10.1016/j.ijheatfluidflow.2009.02.017

Keller, W.W., Pauly, L.W., 2009. Innovation in the Indian semiconductor industry: The challenge of sectoral deepening. Bus Polit 11, 1–22. https://doi.org/10.2202/1469-3569.1270

Khadamkar, H.P., Patwardhan, A.W., Mathpati, C.S., 2017. Computational Fluid Dynamics Simulations of Single Drops in Confined Geometries. Ind Eng Chem Res 56, 8311–8329. https://doi.org/10.1021/acs.iecr.7b00443

Khadiya, S., Kumari, S., Gupta, R., 2021. Hydrodynamics of bubble coalescence in microchannels. Can J of Chem Engg 99, 1199–1210. https://doi.org/10.1002/cjce.23918

Klaseboer, E., Gupta, R., Manica, R., 2014. An extended Bretherton model for long Taylor bubbles at moderate capillary numbers. Phys. Fluids 26, 032107(1)-032107(8). https://doi.org/10.1063/1.4868257

Kolb, W.B., Cerro, R.L., 1991. Coating the inside of a capillary of square cross section. Chem Eng Sci 46, 2181–2195. https://doi.org/10.1016/0009-2509(91)85119-I

Kositanont, C., Putivisutisak, S., Tagawa, T., Yamada, H., Assabumrungrat, S., 2014. Multiphase parallel flow stabilization in curved microchannel. Chemical Engineering Journal 253, 332–340. https://doi.org/10.1016/J.CEJ.2014.05.023

Kovalchuk, N.M., Chowdhury, J., Schofield, Z., Vigolo, D., Simmons, M.J.H., 2018. Study of drop coalescence and mixing in microchannel using Ghost Particle Velocimetry. Chemical Engineering Research and Design 132, 881–889. https://doi.org/10.1016/j.cherd.2018.01.034

Kumari, S., Kumar, N., Gupta, R., 2019. Flow and heat transfer in slug flow in microchannels: Effect of bubble volume. Int J Heat Mass Transf 129, 812–826. https://doi.org/10.1016/j.ijheatmasstransfer.2018.10.010

Lai, Y.K., Rosin, P.L., 2014. Efficient circular thresholding. IEEE Transactions on Image Processing 23, 992–1001. https://doi.org/10.1109/TIP.2013.2297014

Lakehal, D., Thomas, S., Caviezel, D., Narayanan, C., Labois, M., 2012. Advanced two- and three-dimensional simulation of multiphase flow in horizontal and vertical pipes, in: BHR Group - 8th North American Conference on Multiphase Technology.

Lakhera, P., Chaudhary, V., Bhardwaj, B., Kumar, P., Kumar, S., 2022. Development and recent advancement in microfluidics for point of care biosensor applications: A review. Biosens Bioelectron X. https://doi.org/10.1016/j.biosx.2022.100218

Lee, C.Y., Wang, W.T., Liu, C.C., Fu, L.M., 2016. Passive mixers in microfluidic systems: A review. Chemical Engineering Journal 288, 146–160. https://doi.org/10.1016/J.CEJ.2015.10.122

Legendre, D., Colin, C., Coquard, T., 2008. Lift, drag and added mass of a hemispherical bubble sliding and growing on a wall in a viscous linear shear flow. Philosophical Transactions of the Royal Society A: Mathematical, Physical and Engineering Sciences 366, 2233–2248. https://doi.org/10.1098/rsta.2008.0009

Lekhlifi, A., Antoni, M., Ouazzani, J., 2010. Numerical simulation of the unsteady hydrodynamics of a water droplet in paraffin oil. Colloids Surf A Physicochem Eng Asp 365, 70–78. https://doi.org/10.1016/j.colsurfa.2010.04.036

Leung, S.S.Y., Gupta, R., Fletcher, D.F., Haynes, B.S., 2012. Gravitational effect on Taylor flow in horizontal microchannels. Chem Eng Sci 69, 553–564. https://doi.org/10.1016/J.CES.2011.11.016

Li, C.H., Lee, C.K., 1993. Minimum cross entropy thresholding. Pattern Recognit 26, 617–625. https://doi.org/10.1016/0031-3203(93)90115-D

Liu, Q., Palm, B., 2016. Numerical study of bubbles rising and merging during convective boiling in micro-channels. Appl Therm Eng 99, 1141–1151. https://doi.org/10.1016/j.applthermaleng.2016.01.116

López, J., Ratkovich, N., Pereyra, E., 2020. Analysis of two-phase air-water annular flow in U-bends. Heliyon 6, e05818. https://doi.org/10.1016/J.HELIYON.2020.E05818

Magnini, M., Municchi, F., El Mellas, I., Icardi, M., 2022. Liquid film distribution around long gas bubbles propagating in rectangular capillaries. International Journal of Multiphase Flow 148, 103939. https://doi.org/10.1016/j.ijmultiphaseflow.2021.103939

Mandal, T.K., Bhuyan, M.K., Das, G., Das, P.K., 2008. Effect of undulation on gas–liquid two-phase flow through a horizontal pipeline. Chemical Engineering Research and Design 86, 269–278. https://doi.org/10.1016/J.CHERD.2007.11.014

Mashayek, F., Ashgriz, N., Minkowycz, W.J., Shotorban, B., 2003. Coalescence collision of liquid drops. Int J Heat Mass Transf 46, 77–89. https://doi.org/10.1016/S0017-9310(02)00256-9

Mazzolai, B., Mattoli, V., 2016. Generation soft Friendly neighbours feed tumour cells. Nature 536, 400.

Mehrabian, S., Acosta, E., Bussmann, M., 2018. Oil-particle separation in a falling sphere configuration: Effect of viscosity ratio & interfacial tension. Int. J. Multiph. Flow 98, 120–127. https://doi.org/10.1016/j.ijmultiphaseflow.2017.09.004

Menchaca-Rocha A, Martínez-Dávalos A, Núñez R, Popinet S, Zaleski S., 2001. Coalescence of liquid drops by surface tension. Phys Rev E Stat Phys Plasmas Fluids Relat Interdiscip Topics 63, 046309. https://doi.org/10.1103/PhysRevE.63.046309

Mishra, D., Mohanty, D., Gupta, R., Singh, A., 2022. Effect of Bend on Film Thickness in Slug, Slug-Annular, and Annular Flow Regimes in Gas–Liquid Flow in a Microchannel. Ind Eng Chem Res 61, 14081–14092. https://doi.org/10.1021/acs.iecr.2c01905

Muradoglu, M., Stone, H.A., 2007. Motion of large bubbles in curved channels. J Fluid Mech 570, 455–466. https://doi.org/10.1017/S0022112006002692

Nino, V., Hrnjak, P.S., Newell, T.A., 2002. Analysis of void fraction in microchannels. International Refrigeration Conference at Purdue University.

Noishiki, K., Miwa, Y., Matsuoka, A., 2013. Microchannel reactor (Stacked multi-channel reactor: SMCR®) for bulk chemical industry. R and D: Research and Development Kobe Steel Engineering Reports 63, 28–32.

Nowak, E., Kovalchuk, N.M., Che, Z., Simmons, M.J.H., 2016. Effect of surfactant concentration and viscosity of outer phase during the coalescence of a surfactant-laden drop with a surfactant-free drop. Coll and Surf A: Phys and Engg Asp 505, 124–131. https://doi.org/10.1016/j.colsurfa.2016.02.016

Oliver, D.L.R., Chung, J.N., 1985. Steady flows inside and around a fluid sphere at low Reynolds numbers. J Fluid Mech 154, 215–230. https://doi.org/10.1017/S0022112085001495

Pan, L.J., Tu, J.W., Ma, H.T., Yang, Y.J., Tian, Z.Q., Pang, D.W., Zhang, Z.L., 2018. Controllable synthesis of nanocrystals in droplet reactors. Lab Chip. https://doi.org/10.1039/c7lc00800g

Pandya, D., Nagarajappa, Kumar, A., Reddy, Sreedevi., Bhasin, Meenakshi., 2015. Lab-on-a-Chip – Oral Cancer Diagnosis at Your Door Step. Journal of International Oral Health 7, 122–128.

Pang, Z., Zhu, C., Ma, Y., Fu, T., 2020. CO2 Absorption by Liquid Films under Taylor Flow in Serpentine Minichannels. Ind Eng Chem Res 59, 12250–12261. https://doi.org/10.1021/acs.iecr.0c02217

Patel, R.S., Weibel, J.A., Garimella, S. v., 2015. An optical approach for quantitative characterization of slug bubble interface profiles in a two-phase microchannel flow. Int J Heat Mass Transf 86, 31–38. https://doi.org/10.1016/J.IJHEATMASSTRANSFER.2015.02.067

Paulsen, J.D., 2013. Approach and coalescence of liquid drops in air. Phys Rev E Stat Nonlin Soft Matter Phys 88, 063010. https://doi.org/10.1103/PhysRevE.88.063010

Paulsen, J.D., Carmigniani, R., Kannan, A., Burton, J.C., Nagel, S.R., 2014. Coalescence of bubbles and drops in an outer fluid. Nat Commun 5, 3182. https://doi.org/10.1038/ncomms4182

Picardo, J.R., Pushpavanam, S., 2013a. Core-annular two-phase flow in a gently curved circular channel. AIChE Journal 59, 4871–4886. https://doi.org/10.1002/aic.14247

Picardo, J.R., Pushpavanam, S., 2013b. Core-annular two-phase flow in a gently curved circular channel. AIChE Journal 59, 4871–4886. https://doi.org/10.1002/aic.14247

Rahman, M.M., Lee, W., Iyer, A., Williams, S.J., 2019. Viscous resistance in drop coalescence. Phys. Fluids 31, 1–10. https://doi.org/10.1063/1.5064706

Rahmat, A., Yildiz, M., 2018. A multiphase ISPH method for simulation of droplet coalescence and electro-coalescence. Int J of Multiph Flow 105, 32–44. https://doi.org/10.1016/j.ijmultiphaseflow.2018.03.006

Ramji, S., Rakesh, A., Pushpavanam, S., 2019. Modelling mass transfer in liquid-liquid slug flow in a microchannel. Chemical Engineering Journal 364, 280–291. https://doi.org/10.1016/j.cej.2019.01.075

Rastog, V., 2018. Micro, Small, and Medium Enterprises in India – An Explainer. india briefing 3.

Ratulowski, J., Chang, H., 1989. Transport of gas bubbles in capillaries. Physics of Fluids A: Fluid Dynamics 1, 1642–1655. https://doi.org/10.1063/1.857530

Rawal, S., Sidpara, A.M., Paul, J., 2022. A review on micro machining of polymer composites. J Manuf Process. https://doi.org/10.1016/j.jmapro.2022.03.014

R.H. Magarvey and Juris Kalejs, 1963. Internal circulation within liquid drop. Nature 198, 377–378.

Rybczynski, W., 1911. Uber die fortschreitende bewegung einer flussigen kugel in einem zahen medium. Bull. Acad. Sci. Cracovie A 1, 40–46.

Sahu, K.C., 2021. A new linearly unstable mode in the core-annular flow of two immiscible fluids. J Fluid Mech 918, A11. https://doi.org/10.1017/jfm.2021.349

Sarvar-Ardeh, S., Rashidi, S., Rafee, R., Karimi, N., 2023. A review on the applications of micro-/mini-channels for battery thermal management. J Therm Anal Calorim 148, 7959–7979. https://doi.org/10.1007/s10973-023-12092-6

Saucedo-Espinosa, M.A., Breitfeld, M., Dittrich, P.S., 2023. Continuous Electroformation of Gold Nanoparticles in Nanoliter Droplet Reactors. Angewandte Chemie - International Edition 62, e202212459. https://doi.org/10.1002/anie.202212459

Savic, 1953. Circulation and Distortion of Liquid Drops Falling Through a Viscous Liquid. National Research Council of Canada MT-22, 1–33.

Schindelin, J., Arganda-Carreras, I., Frise, E., Kaynig, V., Longair, M., Pietzsch, T., Preibisch, S., Rueden, C., Saalfeld, S., Schmid, B., Tinevez, J.Y., White, D.J., Hartenstein, V., Eliceiri, K., Tomancak, P., Cardona, A., 2012. Fiji: An open-source platform for biological-image analysis. Nat. Methods. https://doi.org/10.1038/nmeth.2019

Sen, N., 2010. Two-phase slug-to-annular flow pattern transition in microgravity. Acta Astronaut 66, 1373–1377. https://doi.org/10.1016/j.actaastro.2009.10.029

Sen, N., 2009. Suratman number in bubble-to-slug flow pattern transition under microgravity. Acta Astronaut 65, 423–428. https://doi.org/10.1016/j.actaastro.2009.02.013

Sharma, B., Lakra, U., Sharma, R., Sharma, S.R., 2022. A comprehensive review on nanopesticides and nanofertilizers—A boon for agriculture, in: Nano-Enabled Agrochemicals in Agriculture. Elsevier, pp. 273–290. https://doi.org/10.1016/B978-0-323-91009-5.00026-4

Sharma, V.K., Tiwari, P., Singh, A., 2021. Micro-particle Image Velocimetry Measurements of Pore-Scale Velocity Field during Nanoparticle-Assisted Alkaline Flooding. Energy & Fuels 35, 12957–12973. https://doi.org/10.1021/acs.energyfuels.1c00592

Shen, F., Du, W., Kreutz, J.E., Fok, A., Ismagilov, R.F., 2010. Digital PCR on a SlipChip. Lab Chip 10, 2666–2672. https://doi.org/10.1039/c004521g

Simmons, M.J., Wong, D.C.Y., Travers, P.J., Rothwell, J.S., 2002. Bubble behaviour in three phase capillary microreactors. International Journal of Chemical Reactor Engineering 1. https://doi.org/10.2202/1542-6580.1046

Spells, K.E., 1952. A study of circulation patterns within liquid drops moving through a liquid. Proc of the Phy Soc, Sec B 65, 541–546. https://doi.org/10.1088/0370-1301/65/7/310

Sprittles, J.E., Shikhmurzaev, Y.D., 2012. Coalescence of liquid drops: Different models versus experiment. Phys. Fluids 24, 122105. https://doi.org/10.1063/1.4773067

Sternberg, S.R., 1983. Biomedical Image Processing. Computer (Long Beach Calif) 16, 22–34. https://doi.org/10.1109/MC.1983.1654163

Subasinghe, C.S., Ratnayake, A.S., Roser, B., Sudesh, M., Wijewardhana, D.U., Attanayake, N., Pitawala, J., 2022. Global distribution, genesis, exploitation, applications, production, and demand of industrial heavy minerals. Arabian Journal of Geosciences 15, 1–28. https://doi.org/10.1007/s12517-022-10874-0

Suo, M., Griffith, P., 1964. Two-Phase Flow in Capillary Tubes. Journal of Basic Engineering 86, 576–582. https://doi.org/10.1115/1.3653176

Thome, J.R., 2004. Boiling in microchannels : a review of experiment and theory 25, 128–139. https://doi.org/10.1016/j.ijheatfluidflow.2003.11.005

Thoroddsen, S.T., Takehara, K., Etoh, T.G., 2005. The coalescence speed of a pendent and a sessile drop. J Fluid Mech 527, 85–114. https://doi.org/10.1017/S0022112004003076

Tirre, F., Kampschulte, L., Thoma, G.B., Höffler, T., Parchmann, I., 2019. Design of a student lab program for nanoscience and technology–an intervention study on students' perceptions of the Nature of Science, the Nature of Scientists and the Nature of Scientific Inquiry. Research in Science and Technological Education 37, 393–418. https://doi.org/10.1080/02635143.2018.1551201

Tiwari, A., Rajesh, V.M., Yadav, S., 2018. Biodiesel production in micro-reactors: A review. Energy for Sustainable Development. https://doi.org/10.1016/j.esd.2018.01.002

Triplett, K.A., Ghiaasiaan, S.M., Abdel-Khalik, S.I., Sadowski, D.L., 1999. Gas-liquid two-phase flow in microchannels part I: Two-phase flow patterns. International Journal of Multiphase Flow 25, 377–394. https://doi.org/10.1016/S0301-9322(98)00054-8

Unger, M.A., Unger, M.A., Chou, H., Thorsen, T., Scherer, A., Quake, S.R., 2013. Monolithic Microfabricated Valves and Pumps by Multilayer Soft Lithography. Science 113, 113–116. https://doi.org/10.1126/science.288.5463.113

Usha, R., Sahu, K.C., 2019. Interfacial instability in pressure-driven core-annular pipe flow of a Newtonian and a Herschel–Bulkley fluid. J Nonnewton Fluid Mech 271, 104144. https://doi.org/10.1016/J.JNNFM.2019.104144

Vashisth, S., Kumar, V., D. P. Nigam, K., 2008. A Review on the Potential Applications of Curved Geometries in Process Industry. Ind Eng Chem Res 47, 3291–3337. https://doi.org/10.1021/ie701760h

Waheed, M.A., Henschke, M., Pfennig, A., 2004. Simulating sedimentation of liquid drops. Int J Numer Methods Eng 59, 1821–1837. https://doi.org/10.1002/nme.920

Wang, C., Zhao, N., Chen, C., Sun, H., 2018. A method for direct thickness measurement of wavy liquid film in gas-liquid two-phase annular flow using conductance probes. Flow Measurement and Instrumentation 62, 66–75. https://doi.org/10.1016/j.flowmeasinst.2018.05.002

Wang, Jianmei, Li, Y., Wang, X., Wang, Jianchun, Tian, H., Zhao, P., Tian, Y., Gu, Y., Wang, L., Wang, C., 2017. Droplet microfluidics for the production of microparticles and nanoparticles. Micromachines (Basel). https://doi.org/10.3390/mi8010022

Widianto, A.Y., Aubin, J., Xuereb, C., Poux, M., 2020. Gas-liquid-liquid reactions: Contacting mechanisms and effective process technologies. Catal Today 346, 46–57. https://doi.org/10.1016/j.cattod.2019.02.064

Wu, M., Cubaud, T., Ho, C.M., 2004. Scaling law in liquid drop coalescence driven by surface tension. Phys. Fluids 16, L51–L54. https://doi.org/10.1063/1.1756928

Wu, Z., Sundén, B., 2019. Liquid-liquid two-phase flow patterns in ultra-shallow straight and serpentine microchannels. Heat and Mass Transfer 55, 1095–1108. https://doi.org/10.1007/s00231-018-2494-0

Xiong, P., Chen, X., Xiong, Y., Liu, G., Tian, Y., 2016. Microstructure-enhanced liquid-liquid extraction in a real-time fluorescence detection microfluidic chip. Micromachines (Basel) 7. https://doi.org/10.3390/mi7030046

Yamauchi, M., Uemura, T., Ozawa, M., 2000. Velocity distributions inside and outside of a water drop in oil. Application of Laser Techniques to Fluid Mechanics, CD-ROM 1–6.

Yao, C., Ma, H., Zhao, Q., Liu, Y., Zhao, Y., Chen, G., 2020. Mass transfer in liquid-liquid Taylor flow in a microchannel: Local concentration distribution, mass transfer regime and the effect of fluid viscosity. Chem Eng Sci 223, 115734. https://doi.org/10.1016/J.CES.2020.115734

Zaloha, P., Kristal, J., Jiricny, V., Völkel, N., Xuereb, C., Aubin, J., 2012. Characteristics of liquid slugs in gas-liquid Taylor flow in microchannels. Chem Eng Sci 68, 640–649. https://doi.org/10.1016/j.ces.2011.10.036

Zhang, M., Vokoun, A.E., Chen, B., Deng, W., Dupont, R.L., Xu, Y., Wang, X., 2023. Advancements in Droplet Reactor Systems Represent New Opportunities in Chemical Reactor Engineering: A Perspective. Can J Chem Eng 101, 5189–5207. https://doi.org/10.1002/cjce.24897

Zhang, P., Yao, C., Ma, H., Jin, N., Zhang, X., Lü, H., Zhao, Y., 2018. Dynamic changes in gas-liquid mass transfer during Taylor flow in long serpentine square microchannels. Chem Eng Sci 182, 17–27. https://doi.org/10.1016/j.ces.2018.02.018

Zhao, T.S., Bi, Q.C., 2001. Pressure drop characteristics of gas-liquid two-phase flow in vertical miniature triangular channels. Int J Heat Mass Transf 44. https://doi.org/10.1016/S0017-9310(00)00282-9

Zhou, J., Cao, X., Zhang, N., Yuan, Y., Zhao, X., Hardy, D., 2020. Micro-Channel Heat Sink: A Review. Journal of Thermal Science. https://doi.org/10.1007/s11630-020-1334-y

Zhou, Y., Yao, C., Zhang, P., Zhang, X., Lu, H., Zhao, Y., 2020. Dynamic coupling of mass transfer and chemical reaction for Taylor flow along a serpentine microchannel. Ind Eng Chem Res 59, 9279–9292. https://doi.org/10.1021/acs.iecr.0c00014

Zong, J., Yue, J., 2022. Continuous Solid Particle Flow in Microreactors for Efficient Chemical Conversion. Ind Eng Chem Res 61, 6269–6291. https://doi.org/10.1021/acs.iecr.2c00473

Appendix

As mentioned in Chapter 3, the analytical solution to two-phase flow in U bend microchannel is derived for two-dimensional geometry. A two-dimensional circular bend with inner radius R_1 and outer radius R_2 is selected for the two-phase annular flow, as shown in Figure A: 1. The fluid in the core has a dynamic viscosity μ_G and outer liquid has a viscosity μ_L. The interfaces formed between the two phases have radii R_i and R_o, and the subscripts i and o refer to the radius of the inner and outer interfaces, respectively. Figure A: 1 shows the schematic diagram of the system where a two-phase flow comes in from one side and goes out from the opposite side. The two-phase flow inside the bend is divided into three regions (I, II, and III). Note that the analysis is performed in a two-dimensional plane, and therefore, the secondary or Dean flow that occurs in a curved channel cannot be modeled. Further, while zone I and zone III represent the same fluids, they are separate regions in this model and are independent of each other. Therefore, this work can also be considered as a model for the parallel flow of three liquids in a circular bend. In general, there are waves present on the interface in the gas-liquid annular flow. We assume the solution to be a smooth interface solution, and the wavy nature of the interface is neglected.

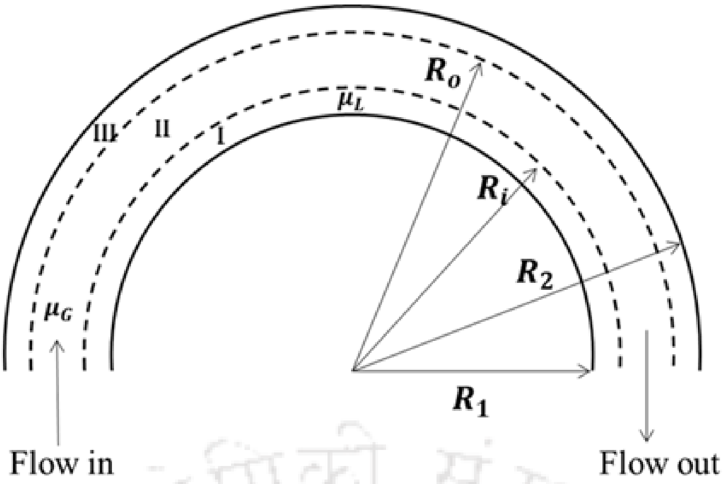

Figure A: 1 Schematic diagram of two-phase flow inside a semicircular bend with three regions of flow.

The Navier-Stokes equation is solved in cylindrical coordinates (r and θ *coordinates*). Flow is assumed to be incompressible, fully developed, and steady. Therefore, v_r = 0, $v_\theta \neq$ 0 and v_z = 0. The simplified momentum conservation equations assuming the fluids to be Newtonian can be written as:

***r* momentum equation**:

$$\frac{\rho {v_\theta}^2}{r} = \frac{\partial p}{\partial r} \qquad (a)$$

***θ* momentum equation**:

$$\mu\left[\frac{\partial}{\partial r}\left(\frac{1}{r}\frac{\partial}{\partial r}(r v_\theta)\right)\right] = \frac{1}{r}\frac{\partial p}{\partial \theta} = \frac{B}{r}, \quad where \quad \frac{\partial p}{\partial \theta} = B \qquad \text{(b)}$$

Velocity profiles is obtained by integrating equation (b) twice for each of the three regions. In each case, there will be two integration constants.

$$v_{\theta_I} = f(C_1,\ C_2), v_{\theta_{II}} = f(C_3,\ C_4), \text{and } v_{\theta_{III}} = f(C_5,\ C_6)$$

Table A: 1 Boundary conditions at the wall and interfaces

1	$r = R_1$	$v_{\theta_I} = 0$
2	$r = R_2$	$v_{\theta_{III}} = 0$
3	$r = R_i$	$v_{\theta_I} = v_{\theta_{II}}$
4	$r = R_o$	$v_{\theta_{II}} = v_{\theta_{III}}$
5	$r = R_i$	$\tau_{r\theta_I} = \tau_{r\theta_{II}}$
6	$r = R_o$	$\tau_{r\theta_{II}} = \tau_{r\theta_{III}}$

***<u>θ momentum equation</u>*:**

$$\mu\left[\frac{\partial}{\partial r}\left(\frac{1}{r}\frac{\partial}{\partial r}(rv_\theta)\right)\right] = \frac{1}{r}\frac{\partial p}{\partial \theta} = \frac{B}{r}, \quad where \quad \frac{\partial p}{\partial \theta}$$

$$= B$$

$$\int \partial\left(\frac{1}{r}\frac{\partial(rv_\theta)}{\partial r}\right) = \int \frac{B}{\mu r}\partial r$$

$$\frac{1}{r}\frac{\partial(rv_\theta)}{\partial r} = \frac{B}{\mu}\ln r + C_1$$

$$\int \partial(rv_\theta) = \int\left(\frac{B}{\mu}r\,(\ln r)\right)\partial r + \int rC_1\,\partial r$$

$$v_\theta = \frac{Br}{4\mu}(2\ln(r) - 1) + \frac{r\xi_1}{2} + \frac{\xi_2}{r} \qquad (1)$$

Note: $\int(x\,(ln\,x))\,\partial x = \frac{x^2}{2}\left(ln(x) - \frac{1}{2}\right) + \xi$

Where ξ_1 and ξ_2 are an integration constant.

BC 1:

At $r = R_1, v_{\theta_I} = 0$

$$v_{\theta_I} = \frac{BR_1}{4\mu_L}(2\ln(R_1) - 1) + \frac{R_1 C_1}{2} + \frac{C_2}{R_1} = 0$$

$$C_2 = -\left(\frac{B{R_1}^2}{4\mu_L}(2\ln(R_1) - 1) + \frac{{R_1}^2 C_1}{2}\right) \tag{2}$$

BC 2:

At $r = R_2, v_{\theta_{III}} = 0$

$$v_{\theta_{III}} = \frac{BR_2}{4\mu_L}(2\ln(R_2) - 1) + \frac{R_2 C_5}{2} + \frac{C_6}{R_2} = 0$$

$$C_6 = -\left(\frac{B{R_2}^2}{4\mu_L}(2\ln(R_2) - 1) + \frac{{R_2}^2 C_5}{2}\right) \tag{3}$$

BC 5 & 6:

At $r = R_i, \tau_{r\theta_I} = \tau_{r\theta_{II}}$

Note that: $\tau_{r\theta} = \mu\left[r\frac{\partial}{\partial r}\left(\frac{v_\theta}{r}\right)\right]$

$$\tau_{r\theta_I} = \tau_{r\theta_{II}}$$

$$\mu_L\left[R_i\frac{\partial}{\partial r}\left(\frac{v_{\theta_I}}{r}\right)\right] = \mu_G\left[R_i\frac{\partial}{\partial r}\left(\frac{v_{\theta_{II}}}{r}\right)\right]$$

$$\boldsymbol{C_2} = \frac{\mu_G}{\mu_L}\boldsymbol{C_4} = \boldsymbol{C_6}$$

BC 3:

At $r = R_i, v_{\theta_I} = v_{\theta_{II}}$

$$\frac{BR_i}{4\mu_L}(2\ln(R_i)-1)+\frac{R_iC_1}{2}+\frac{C_2}{R_i}=\frac{BR_i}{4\mu_G}(2\ln(R_i)-1)+\frac{R_iC_3}{2}+\frac{C_4}{R_i}$$

After solving these equations, one can calculate the expressions for six constants (C_1 to C_6). It can be solved for a separate equation for all the constants. Once we get the constant values, it can be used to derive velocities of all three regions (v_{θ_I}, $v_{\theta_{II}}$, $v_{\theta_{III}}$).

The analytical solution as discussed above can be useful for a number of instants. Some examples are, to obtain velocity profile in a two-dimensional curved channel, velocity profile in three phase parallel flow in a 2D circular bend, velocity profile in annular or Taylor bubble (in the liquid film surrounding the bubble) for given film thickness. The limitation of this analysis is that it treats the inner and outer liquids separately and the change in region I does not cause the change in region III.